Atomistic simulations of the mineral water interface

Spagnoli, Dino

Award date:
2006

Awarding institution:
University of Bath

Atomistic Simulations of the Mineral Water Interface

Submitted by Dino Spagnoli
for the degree of
Doctor of Philosophy
of the University of Bath
Department of Chemistry
November 2006

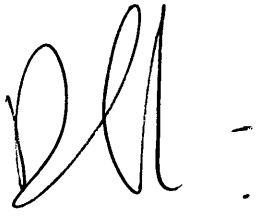

ProQuest LLC
789 East Eisenhower Parkway
P.O. Box 1346
Ann Arbor, MI 48106-1346

Abstract

The aim of this thesis is to use computer simulations to describe the interactions between a mineral surface and water. The two minerals of choice are the calcium carbonate polymorph, calcite, and magnesium oxide, periclase. In this study we consider not only surfaces but also nanoparticles with a finite size.

In Chapter 1, the relevant experimental and computational studies of the mineral-water interface are reviewed and the theory of colloidal stability is presented as it affects the structure of the mineral-water interface and interaction of nanoparticles.

Chapters 2 and 3 discuss the methodology used throughout this thesis. The work presented in this thesis uses atomistic simulations and the reliability of the results depends on the interatomic potential used. Therefore Chapter 2 discussed in detail the definition of the potential model and how reliable potential model parameters are derived. Chapter 3 gives an introduction to the theoretical methods used, which are energy minimisation and molecular dynamics.

Chapters 4 through to 6 present the main results obtained during this investigation. A number of calcite surfaces are considered in dry and aqueous conditions in chapter 4. The most stable flat, $\{10\bar{1}4\}$ surface is considered along with two vicinal surfaces, the $\{31\bar{4}8\}$ and $\{3\bar{1}\bar{2}16\}$, which both consists of flat $\{10\bar{1}4\}$ terraces and steps. The $\{31\bar{4}8\}$ forms an acute step and the $\{3\bar{1}\bar{2}16\}$ surface forms an obtuse step, both of which contain neutral step edges. Four kinked surfaces are also considered. On a step edge a kink is an offset where the edge jumps one or more atomic units. The four different kinked surfaces can be named by the orientation of the step followed by the orientation of the partial step at the kink. The structures of water above these surfaces are described using molecular dynamics simulations.

The free energy profiles of the dissolution of ions from both the flat and stepped surfaces were investigated and it was found that dissolution is more likely to occur at the lower coordinated stepped surface. In addition, the complexity of the system was increased by considering the interaction of a polymeric additive, polyacrylic acid, on the flat calcite surface. The adsorption of only one of the polyacrylic salts occurred when the surface has an opposite charge to the molecule.

In Chapter 5 energy minimisation is used to study the surface reactivity of the {100} MgO nanoparticle. By calculating the energy to dissociatively adsorb water onto the surface of the nanoparticle, it was found that the lower coordinated corner site is the most reactive. The structure of water around the MgO nanoparticle is considered using molecular dynamic simulations and compared with a smaller calcite nanoparticle. Finally, charged MgO nanoparticles are immersed in salt water and the distribution of the salt ions are observed. Even though these simulations need longer to run, the change in charge strongly influences the distribution of oppositely charged ions around the nanoparticle.

While Chapter 5 discussed the interactions of one nanoparticle with its environment, Chapter 6 studies the interaction of two approaching nanoparticles with each other. The aggregation of calcite nanoparticles evolves into a very different structure compared to bulk. The aggregation of MgO nanoparticles is strongly orientated by the stable ⟨100⟩ direction. The free energy of aggregation was evaluated and restricting the rotation of the nanoparticles enabled a free energy profile with no free energy barrier to occur.

Finally, Chapter 7 gives a summary of the main results presented in this thesis.

Acknowledgements

I would like to firstly thank Prof Steve Parker for his guidance and support during my PhD. He is always available to discuss issues that arise and has taught me a great deal during my project. Without him, then the opportunities that are now opening for me would not have arrived.

The members of the Computational Solid State Chemistry Group in Bath have always made it an enjoyable and welcoming place to work. I would like to thank the members of this group: Paul Martin, Jeremy Allen, Dr Corinne Arrouvel, Dr Arnaud Marmier and especially Dr David Cooke for help on programming matters and simulation of nanoparticles and Dr Sebastien Kerisit for help on the calcite-water interface. I also wish to thank Dr Paul Bowen at Ecole Polytechnique Fédérale de Lausanne for useful discussions.

I would like to thank the Engineering and Physical Sciences Research Council (EPSRC) and the Department of Chemistry at the University of Bath for funding my studentship and the EPSRC funded Materials Chemistry Consortium, the Natural Environment Research Council (NERC) funded Computational Mineral Physics Consortium and the EPSRC funded MOTT2 facility run by CCLRC e-Science Centre for computer time.

I would also like to thank the seven-a-side post grad and staff Chemistry football team for allowing me to play in goal even though I made the odd mistake here and there!!!

Last, but by no means least, I would like to thank my friends and family for supporting me throughout my studies. A special mention must go to my ever supportive parents who are just brilliant. My sister, Daniela, always has an ear open when I need it and my little brother Giacomo always makes me smile, especially when he said to his teacher, "I want to be a scientist just like my brother!!"

Contents

Chapter 1

Introduction

The interaction of aqueous solutions with mineral surfaces is one of the most important chemical reactions occurring in nature. This interface plays a governing role in dissolution, precipitation and adsorption processes [1]. However, this interface is also important in the preparation and performance of metal-on-metal oxide catalysts, the cleaning of semiconductor surfaces, water treatment, metal corrosion and surface passivation [2]. The mineral-water interface has received a great deal of attention due to its complex nature. The complexity arises because of the variation of behaviour including the formation of inner- or outer-sphere complexes [3, 4], varying water density depending on the distance away from the surface [5] and the electric double layer (EDL) [6].

The central theme of this project is to investigate the role of the solvent on mineral surfaces, to try to understand these phenomena on an atomic scale and how this behaviour differs at the surfaces of nanoparticles of the same mineral. Furthermore, as a way of distinguishing behaviour that is composition dependent we have considered two materials, $CaCO_3$ and MgO.

$CaCO_3$ has been at the centre of much research interest, particularly the most stable polymorph of calcium carbonate, calcite. Calcium carbonate can be found naturally as three polymorphs; calcite, aragonite and vaterite, but by far the most abundant is calcite [7]. One of the reasons for the increasing research interest is due to the fact that calcite has the ability to adsorb pollutant metals into its lattice and is widely used by micro-organisms in the biomineralisation process. Biomineralisation describes the deposition of minerals within or outside the cells of living organisms. Examples include iron and gold deposits in bacteria, silicates in algae, carbonates in diatoms and nonvertebrates, and calcium phosphates and carbonates in vertebrates [8]. It is important to realise that the morphology and structure of these shells does not resemble the morphology of the naturally occurring mineral.

Another important role of calcite in the environment is its involvement in the carbon cycle and the storage of green house gases in two different ways. Firstly, calcite is precipitated in the oceans by marine organisms from dissolved carbon dioxide and is subsequently stored on the seafloor in layers of limestone. Secondly, the weathering of calcite produces carbonate ions, which combine with water to eventually release carbon dioxide. Therefore, calcium carbonate can act as a reservoir that will buffer the level of CO_2 in the atmosphere and the oceans [9].

The second mineral of technological and geological importance is periclase, MgO. Mineral aerosols such as periclase have a significant impact on the chemistry of trace gases in the troposphere, such as SO_2 and NO_x [10]. The high surface areas these aerosols have increased the reactivity of the mineral and therefore increasing the amount of adsorption of these trace gases. Minerals on the nanoscale have

characteristic high surface to volume ratio, which increases the reactivity compared to their bulk counterparts. The aim of this chapter is to present the current state of knowledge of calcite and periclase surface and nano-chemistry as well as to introduce the main themes of this thesis. Therefore, the main experimental and computational techniques used in the analysis of these minerals will be described first, followed by the theory of colloidal stability which is of relevance to minerals on the nanoscale and where future work in this area will have most impact.

1.1 Experimental Studies

1.1.1 Dry Mineral Surfaces

The chief requirement for the understanding of the behaviour of mineral surfaces is for experimental studies that give the surface composition, the crystallographic structure and the microtopography of the surface. By far the most widely used surface analytical technique for determining surface composition is x-ray photoelectron spectroscopy (XPS) [11]. XPS can give useful chemical state information, including oxidation and structural state parameters. This technique uses soft x-rays which advance onto the surface and eject photoelectrons from valence and core levels of the surface and the near-surface atoms. An example of this technique being used was a recent study by Chada *et al.* [12]. XPS was used to study the uptake of cadmium and lead ions on the calcite $\{10\bar{1}4\}$ surface. This showed that the uptake kinetics of cadmium ions was faster than lead ions for the low concentration study. Also in dry conditions the concentration of adsorbed species on the surface remained constant for weeks.

Auger electron spectroscopy (AES) has also been a popular surface analytical technique for obtaining surface composition of semiconductors, especially, due to its high spatial resolution capabilities. Auger electrons are generated whenever a

core vacancy is created in an atom. This process generates a characteristic energy from the Auger electron. The problem of AES is that the surface being analysed can be damaged by the electron beam and therefore AES is generally more difficult to interpret and less useful than that from XPS. It is particularly powerful when combined with theoretical studies and has, for example been used to investigate the stabilisation of the polar {111} MgO surface [13]. The results indicate that polar oxide surfaces are a promising candidate for hydrogen storage.

One of the most universally used techniques to study physical properties, such as microtopography of solid surfaces, is scanning electron microscopy (SEM). This technique offers very high imaging resolution down to a few tens of Angstroms. A highly focused beam of electrons is scanned over the mineral surface, and secondary, backscattered, and Auger electrons are generated very near to the point of impact of the beam. Secondary electrons are those defined as whose origin is from the sample and intensity is anything up to the energy of the incident beam. However, the SEM images are formed by the lower energy secondary electrons which are from the valence and conduction bands of the near-surface atoms. The generation of these lower energy electrons is dependent on the composition and the angle at which the incident beam strikes the sample. SEM is a very popular technique in studying the different morphologies observed in the biomineralisation process [14, 15] of minerals such as calcite.

The most common tools used for determining the surface structure of mineral surfaces include low energy electron diffraction (LEED) and scanning tunnelling microscopy (STM). In LEED, a low energy beam of electrons are driven towards a surface. Elastic backscattered primary electrons will undergo Bragg diffraction if the surface is crystalline. The diffraction pattern is recorded and analysis of the spot positions yields information on the size, symmetry and rotational alignment of the sample. Quantitative analysis is achieved where the intensities of various diffracted beams are recorded as a function of the incident electron beam energy and used to generate I-V curves, which provide information on atomic positions. STM has been

used as an auxiliary tool with LEED to study mineral surface structure and reactivity [16]. The tunnelling microscopy utilizes a sharp metallic tip that is brought to within several Angstroms of the surface. Electrons are tunnelled across the gap from the tip to the mineral surface and therefore the perturbations introduced by the mineral surface will be recorded by the differing heights of the tip. The tip will follow the physical contours of the surface and provide a 3-dimensional "image" of the surface, which can have a resolution lower than SEM images. All of these techniques give valuable information on the prepared dry surface, but increasingly, experimental studies are focusing attention on the mineral-water interface.

1.1.2 The Mineral-Water Interface

The most widely used techniques to study the mineral-water interface are atomic force microscopy and synchrotron based methods. Atomic force microscopy (AFM) works by rastering a sample, by means of a single tube piezoelectric translator, under a sharp tip mounted on or part of a flexible microcanterlever [11]. As with STM the sample is rastered under the tip and the perturbations can be measured in order to get a profile on the Angstrom level. A recent AFM study on the surfaces of MgO and TiO_2 were performed under aqueous solution [17]. In this study AFM was used to measure the stability of defects on the surface in aqueous conditions. At the atomic level, MgO (100) gave AFM images of very low contrast, indicating very small force variations on its surface under aqueous environment. TiO_2 (110) showed images with rows whose intervals correspond to those of Ti^{4+} rows. The study indicated slow dissolution rates in aqueous conditions at these surfaces, especially in the case of TiO_2.

The Interfacial Processes Group at Argonne National Laboratory in the USA, which is lead by Paul Fenter, uses synchrotron based techniques such as X-ray reflectivity measurements and Resonant Anomolous X-ray Reflectivity (RAXR) to study the

mineral-water interface. RAXR makes use of the "anomolous" dispersion in the atomic scattering factor of an atom near its characteristic absorption edge. This allows for the possibility of incorporating element-specific information in the X-ray scattering methods. Park *et al.* have used RAXR to study the outer sphere adsorption of platinum species at the oxide-water interface [18]. Since RAXR is element-specific it enabled geometric and spectroscopic information to be yielded for the weakly adsorbed species. Fenter and his group have determined the structure of hydrated calcite [19], barite ($BaSO_4$) [20] and orthoclase ($KAlSiO_3$) [21]. Fenter *et al.* [19] showed that the surface structure of calcite does not vary over a broad pH range. A further study by surface x-ray scattering has determined the 3-dimensional structure of the calcite-water interface. The results reveal that calcite is nearly ideally terminated with a single surface hydration layer containing two distinct water molecules whose heights are 2.3 ± 0.1Å and 3.45 ± 0.1Å [5].

The biological deposition of calcium carbonate is found in marine planktonic coccoliths, sea urchin spicules and coral sclerties [22]. Coccoliths are calcite shields produced by unicellular marine algae and these calcite shields were recently subject of an AFM study in order to determine its crystal orientation [23]. The AFM study revealed that biologically produced calcite shows the same atomic-scale features as freshly cleaved, inorganic crystals. This makes it possible to define the crystal orientation on the shells of the unicellular marine algae.

Henriksen *et al.* went further in studying the stability of coccoliths with and without their organic coating [24]. AFM was used to study dissolving coccoliths and it was found that the coating protects the surface from etching. The coating can be either granular at the flat faces of the coccoliths or fibrous at the stepped central areas. The type of surface and type of coating of organic material on the surface is influential to the dissolution behaviour. The dissolution of the coccoliths occurred more rapidly when the surface had its organic material removed and at the stepped surfaces. Step and kink defects are not uncommon on mineral surfaces and play a

vital role in their reactivity [25]. Steps and kinked surfaces also have an affect on growth and dissolution of mineral surfaces in aqueous conditions [26].

1.1.3 Growth and Dissolution

The first images, using AFM, of the growth and dissolution process of the $\{10\bar{1}4\}$ calcite surface were obtained by Hillner *et al.* in 1992 [27, 28]. Growth occurred in a layer-by-layer fashion by the increasing monoatomic steps and dissolution occurred by the removal of islands, expansion of existing surface pits and motion of steps. Pits were formed in two preferential directions, namely, the $\langle\bar{4}41\rangle$ and $\langle\bar{4}\bar{8}1\rangle$ directions. These pits have rhombohedral shapes which mirrors the symmetry of the calcite crystal structure. From the two directions that form the pits, an acute angle of 78° and an obtuse angle of 102° [29] with respect to the flat terrace is formed. Acute and obtuse steps are common on not just calcite but the other carbonates as well, such as magnesite ($MgCO_3$) [30] and smithsonite ($ZnCO_3$) [31]. A recent study on the dissolution of rhodochrosite ($MnCO_3$) $\{10\bar{1}4\}$ surface revealed that the active sites for dissolution of ions into solution is at step sites [32] (figure 1.1).

Figure 1.1 shows that as the surface is dissolved the etch pit expands at a rate of 90nm every 512 seconds. The depth of the flat-bottomed pit is 4nm and did not increase during the first and last image taken in the study. This study found that the pits were either shallow and flat-bottomed or deep and pointed. The pits in figure 1.1 were formed at a pH of 3.6 but well-formed rhombohedral morphologies were observed at pH of 7.5, 8.3 and 10.3. At pH 5.6, rounding of one of the obtuse angles was observed and at a lower pH of 2.5 or less distortion of internal angles occurred. This could indicate the start of a transition to new pit morphology at low pH.

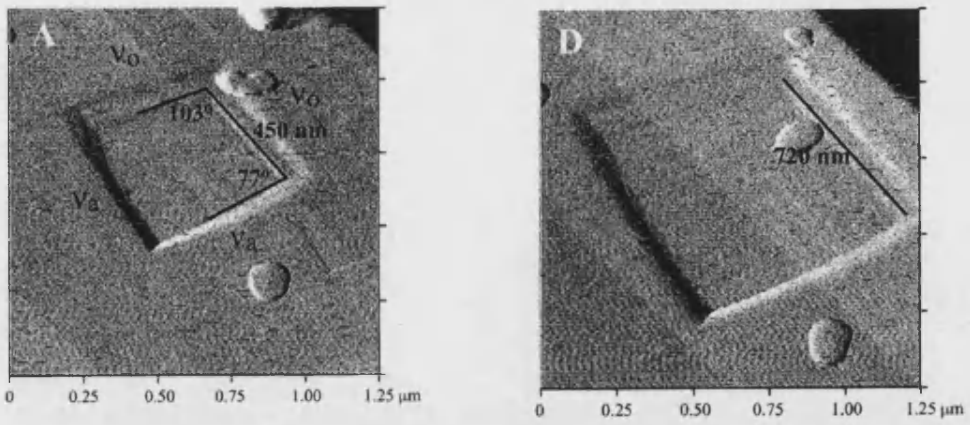

Figure 1.1: AFM images of the dissolution of the $\{10\bar{1}4\}$ face of rhodochrosite at pH=3.6 performed by Duckworth and Martin [32]. The etch pit is bordered by crystallographically equivalent $\langle\bar{4}41\rangle$ and $\langle\bar{4}\bar{8}1\rangle$ steps.

The growth and dissolution rates of calcite and aragonite in water were measured by a pH-stat method as a function of concentration of calcium and carbonate ions and temperature [33]. The pH-stat method, introduced by Meyer in 1979 [34], is a titration technique where the pH of a reaction is continuously measured. Therefore any deviation from the required pH can be quickly compensated. The temperature, speed and volume of reagent addition can be measured throughout and the pH is adjusted accordingly. The pH-stat method is especially good for studies of $CaCO_3$ from solution because the super-saturation can be easily adjusted by the pH. In all "pure" conditions the growth of calcite is strongly preferred. By controlling the saturation and thus the pH of the system the dissolution of aragonite continues while the growth of calcite increases.

Cubillas *et al.* measured the rates of dissolution of calcite, aragonite and three bivalves; ground clam, cockle and mussel shells at 25°C with a mildly basic pH [35]. The two major results of this study are that BET (Brunaur, Emmet and Teller) surface area-normalised rates of the bivalve samples are far lower then the inorganic calcite crystals. However when geometric surface area-normalised

dissolution rates are compared they are found to be very similar. This suggests that geometric surface areas are a better proxy for reactive surface areas because the large BET surface areas tend to have substantially lower percentages of their total areas available for dissolution [36].

The effect of polymeric additives on crystal growth and morphology has been of increasing interest in recent years. Modifications of calcium carbonate powders are generally obtained by the use of additives such as sulphates [37-39], carboxylic acids [40] or phosphates [40]. To control the precipitation reaction, the nucleation and growth steps must be controlled. One way of doing this is by adding polymeric additives to affect this growth. A study by Donnet *et al.* showed that by varying the concentration of polyacrylic acid (PAA) in solution, the shape and size of calcium carbonate powders varies [41].

Biomimetic morphologies of calcium carbonate have been prepared by use of mixed poly (ethylene oxide)-block-poly-(methacrylic acid)-sodium docyclsulphate (PEO-b-PMAA-SDS). The calcium carbonate precipitates out at a size of 2.5-4μm [42] and the concentration of this polymeric additive greatly influences the morphology of the calcium carbonate crystals. At SDS concentration lower than 0.1mM, only calcite spheres or dumb-bell like particles were produced. However, when the SDS concentration was increased to 1 or 2mM, well-defined calcium carbonate hollow spheres were obtained. Interestingly, the presence of both PMAA and PEO segments is necessary for formation of core-shell micelles, and thus calcite hollow spheres. This is consistent with results where solid calcite spheres were produced in mixed PMAA-SDS solutions and rhombohedral calcite crystals were formed in mixed PEO-SDS solutions.

The pH, temperature, concentrations of PAA and $CaCO_3$ turned out to be important parameters for the control of morphology of $CaCO_3$ [43]. Higher temperatures are more beneficial to the formation of monodispersed cubic calcite particles. Increasing the concentration of $CaCO_3$ in the presence of PAA obtained ellipsoidal

and irregular particles. This is attributed to the increase in the relative ratio of polymer to $CaCO_3$.

A study by Tong *et al.* used L-aspartic acid (L-Asp) to control the crystal phase, shape, size and aggregation of calcium carbonate [44]. Calcium carbonate formed the more stable calcite polymorph in the absence of L-Asp but stabilisation of the vaterite polymorph occurred when L-Asp was present. The adsorbed L-Asp controls the nucleation and growth of aggregating particles and maintains the vaterite morphology.

Recently, increasing interest has come from the enantioselective adsorption of chiral molecules on chiral surfaces [45]. Mineral surfaces are very molecular selective [46]. Prebiotic enantioselective adsorption of amino acids onto mineral surfaces has been proposed as a viable mechanism to account for exclusive incorporation of left-handed amino acids in biological organisms [47].

1.1.4 Experimental Synthesis of Mineral Nanoparticles

One of the goals for experimentalists is to be able to keep particles on the nanoscale so that the increased reactivity could be used for catalytic proposes. In general terms, the origins of the increased reactivity are:

i) That the particles have dimensions comparable in length scale of basic quanta in solids,
ii) The surface effects dominate the thermodynamic and energetics of the particle [48].

An example of the increased reactivity of nanoparticles in a geochemical environment was described by Waychunas *et al.* in 2005 [49]. The study described the reactivity of the iron oxyhydroxide with the goethite structure, focusing on its

ability to scavenge toxins from the environment. It concluded that owing to its large surface area and tendency to aggregate as part of their growth process, the nanoparticulate goethite is extremely influential on geochemical processes. The aggregation process is one route that has been continually explored in the synthesis of nanoparticles.

Monodispersed 1.4nm ZnS nanoparticles have been synthesised by stabilising it with 2-hydroxy-1-ethanethiol. The nanoparticles were characterised by Wide-Angle X-ray Scattering (WAXS) [50]. The physical properties were determined in a recent study by Gilbert *et al.* Small-Angle X-ray Scattering (SAXS) was used to obtain the average diameter, High-Resolution Transmission Electron Microscopy (HR-TEM) confirmed that the nanoparticles were spherical, and the structural disorder in the nanoparticles was determined by Extended X-ray Absorption Fine Structure (EXAFS) and WAXS techniques [51]. WAXS and SAXS are x-ray diffraction techniques that are used to analyse Bragg peaks. WAXS is where the Bragg peaks are scattered to wide angles and implies that they are caused by sub-nanometer sized structures. SAXS records these peaks at very low angles, typically 0.1-10°. In this angular range, information about the shape and size of macromolecules, characteristic distances of partially ordered materials and pores sizes can be obtained. EXAFS is a method of determining the bonding of solids by analysing oscillations in x-ray absorption against photon energy that are caused by interference. The structural disorder gave an interesting result which suggested that the nanoparticles are much stiffer than expected. The structural disorder and stiffness modify the electronic properties of nanoparticle materials.

Metal oxide nanoparticles can be synthesised using the sol-gel method which was first introduced by Kistler in 1932 [52]. The aim of this approach is to precipitate metal ions in aqueous media to form a hydroxide gel. The problem that can be found with this is that once the gel is dehydrated, the oxide can have severe sintering which damage to the structure [53]. The most efficient way to eliminate this effect of sintering is to remove the liquid within the gel above its critical

temperature and pressure in an autoclave. Stark *et al.* compared the surface chemistry of autoclave prepared MgO (AP-MgO) nanoparticles with conventionally prepared MgO (CP-MgO) nanoparticles [54]. This comparison showed that more SO_2 and CO_2 were absorbed on the AP-MgO and it was a chemisorption process. The reason for this is due to AP-MgO having more adsorption sites made when dehydration occurs.

Lin *et al.* proposed a synthetic route to prepare calcite on the nanoscale [55]. A gas mixture of carbon dioxide and nitrogen was continuously bubbled into a suspension of calcium hydroxide in triple distilled, carbon dioxide free water. SEM images revealed the presence of calcite nanocrystals in the calcium hydroxide suspension. The nucleation of calcite was inhibited by the increasing concentration of sodium tripolyphosphate. Therefore, it is thought that control of the concentration of these polymeric additives can ultimately control the nucleation rate and size of nanoparticles.

Although it is often difficult to model the mineral-water interface at the same level of complexity as experiment, computational investigations have however made a number of advances.

1.2 Computational Studies

Computational studies of mineral surfaces and the mineral-water interface can fall into three broad categories; atomistic simulations [56], electronic structure calculations [57] and Monte Carlo simulations [58]. Atomistic simulations involve the use of potential based parameterised functions to describe the long- and short-range interaction between atoms. Electronic structure calculations, as the name suggests, is the description of the electron-electron interaction for a specific system by numerical solutions of Schrödinger's equation. Approximations are introduced

to reduce the amount of numerical analysis involved in the calculation, such as Local Density Approximation (LDA) and Generalised Gradient Approximation (GGA). The third technique used in computer simulations is Monte Carlo methods. Monte Carlo is a class of computational algorithms for simulating the behaviour of various physical and mathematical systems. This method differs from others, such as molecular dynamics (MD), as it is stochastic. This means that the algorithms used are nondeterministic in some manner and uses random number or pseudo-random number generators. The most significant for this thesis is the atomistic simulations of the mineral-water interface.

1.2.1 Mineral-Water Interface

Minerals have been simulated using atomistic simulations for many years. Studies have included evaluation of defect energies in bulk minerals [59, 60], on surfaces [61], energetics of grain boundaries [62] and more recently radiation damage in a range of minerals [63]. One of the first simulations that included the interaction between a surface and an explicitly dynamic model for water was in 1993 by Rose and Benjamin [64]. This simulation contained 512 water molecules above the platinum (100) surface, which were three layers of a 5x5 unit cell. This study aimed to determine the electron transfer reaction at a solution–electrode interface.

Simulations of the mineral-water interface since then have increased in complexity. A study by de Leeuw and Parker in 1998 used an explicit dynamical model for water on the stable (100) and stepped (310) MgO surface [65]. The model for water also included a shell around the water oxygen's to account for electronic polarisation. The water structure indicated that there are areas of high and low water density in an oscillating manner above the flat (100) MgO surface. The layering of water above flat surfaces was also found in a study performed by Kerisit *et al.* on the flat $\{10\bar{1}4\}$ calcite surface [66]. The layering appeared to be caused by water

binding strongly to the mineral surface, causing an oscillatory effect throughout the liquid.

The effect of the structure of water on crystal growth was addressed by an investigation by Kerisit and Parker in 2004. Using the thermodynamic integration techniques, described in the following chapter, the free energy change of adsorption of calcium and carbonate ions [67] and other metal ions [68] on the flat $\{10\bar{1}4\}$ calcite surface was calculated. It was revealed that the free energy change of adsorption of these ions on to a surface is strongly influenced by the aqueous media. At high water density the adsorbing ion coordinates with the water molecules and the free energy change lowers. When an adsorbing ion is between two high density areas, the opposite effect occurs. The free energy change increases as the ion is torn between two areas of high water density and leads to the formation of a free energy barrier.

The previous Kerisit and Parker simulation calculated the free energy profile of crystal growth on flat surfaces, however, as is shown in the experimental studies, growth and dissolution occurs at steps and kinked surfaces. One of the first computational studies to involve steps and kinks on calcite surfaces was performed by Kristensen *et al.* [69]. Cuts were made through a calcite structure at low enough angles to the cleavage plane produce faces that can consist of cleavage planes connected by steps [70]. Such faces are named vicinal surfaces because they lie at very low angle to the preferred $\{10\bar{1}4\}$ cleavage face. The investigation by Kristensen *et al.* suggested that the miller indices of these vicinal surfaces can be generalised into two rules; those with obtuse angled steps are $\{n,\bar{1},(-n+1),(4n+4)\}$ and those with acute angles are $\{n,1,(-n-1),(4n-4)\}$. The stability of the steps and kinks was obtained by static energy minimisation calculations. The surface energy of the flat, acute and obtuse steps followed similar trends as in previous studies [66]. The author suggests that the acute step formation energy is higher than that of the obtuse step formation energy. However, the overall stability of the kinks could not be determined due to lack of well-converged results.

The dissolution of ions from mineral surfaces has been investigated using theoretical methods. In 1997, McCoy and La Femina used the Kinetic Monte Carlo (KMC) method to study the rates of dissolution of ions from the flat $\{10\bar{1}4\}$ calcite surface [71]. The KMC method was used to study the shallow-pit formation at the calcite-water interface, as observed experimentally by an AFM study [72]. The KMC model quantitatively reproduces the shallow-pit behaviour occurring in real system as observed using AFM. This method only treats the removal of material from the solid surface and ignores effects such as growth onto the surface. The model simulates the calcite surface configuration as a function of time but does not explicitly simulate the water present. This is taken into account by considering only effective dissolution rates of surface sites at the calcite lattice. The effective dissolution rates are calculated by fitting the simulated behaviour to the experimental behaviour. The surface is represented by the solid-on-solid (SOS) lattice model [73] which employs nearest-neighbour interactions only. The results of this study suggested that "fast" and "slow" rates of dissolution are dependent on what steps cause the pit formation. It was found in this and a previous study [72] that the obtuse step retreats approximately 2.3±0.2 times faster than the acute step.

In 2004, Cooper and de Leeuw executed a series of energy minimisation calculations to investigate the adsorption of water and organic molecules on a range of scheelite ($CaWO_3$) surfaces [74]. The interest in adsorbing organic molecules onto mineral surfaces is that they have an inhibiting effect on crystal growth [75]. Minerals are hydrophilic in nature but it is the physisorbtion of hydrophobic organic surfactants that enable particles to be separated from aqueous media. The results of the study indicate that organic surfactants, such as hydroxymethanamide and methanoic acid, would have to displace preadsorbed water first. This is due to the results of exothermic hydration energies when water was adsorbed onto the surface. It was found that carboxylic acids have higher exothermic adsorption energy then the amines and therefore should be a good surfactant for mineral separation.

The interface between five low index calcite surfaces and monolayers of octadecanoic acid were modelled by Duffy and Harding in 2002 [76]. All interfaces considered to be strongly bound with interfacial energies of around -1 Jm^{-2}. The highest interfacial energy was found for the (100) Ca-terminated interface. A high interfacial energy reveals that there would be an enhanced nucleation rate. Such monolayers will, therefore, substantially enhance the nucleation rate of calcite crystals from solution.

The affect bicarbonate ions on the crystallisation of calcite on Self-Assembled Monolayers (SAM) was studied in 2005 by Duffy *et al.* [77]. The presence of bicarbonate ions in the super-saturated solution not only enhances the nucleation rate but may influence the orientation of the nucleated crystals. The $(01\bar{1}2)$ face of calcite nucleates on a range of substrates, some of which would seem to have very poor lattice matching.

The atomistic simulations described above have been performed using periodic 2-dimensional surfaces; however these techniques have been applied to studying the stability and reactivity of mineral nanoparticles. The next section will review the latest research on computer simulations of mineral nanoparticles.

1.2.2 Computer modelling of mineral nanoparticles

Simulating nanoparticles by atomistic simulations has provided some insight into the unusual behaviour of these materials on the nano-scale. By using a new set of potentials derived by Hamad *et al.* [78] for zinc sulphide (ZnS), Spano *et al.* found computational evidence of ZnS forming bubble type clusters [79]. $(ZnS)_n$ clusters, with n ranging from 10 to 47, were energy minimised using a simulated annealing technique. The simulation is started at very high temperatures, to melt the solid to a liquid, and then the system is cooled by performing a succession of 50ps simulations with the temperature being 10K less than the previous one. This method

enables a greater sampling of configuration space in the simulation. The simulation is systematically started and stopped at regular intervals and after every 50 ps the energy is sampled. The energy can be compared, to evaluate which is the most stable at a given temperature. It was previously thought that large $(ZnS)_n$ clusters, where n is greater than 20, would have a bulk like structure with the majority of atoms four coordinated. However, Spano *et al.* found that spheroidal (bubble) clusters with only three coordinated atoms are more stable than the bulk structure. If the number of ZnS units is increased to 60 then the appearance of onion structures occur [80]. This is a $(ZnS)_{12}$ inside a bubble of $(ZnS)_{48}$. This appears to be the global minimum of the system and agrees with high resolution transmission electron microscope studies of other semiconductor compounds such as BN [81, 82], however as yet these double bubbles are not found in ZnS. This structure has more four coordinated atoms then the smaller ZnS units and also has a more stable structure than the single bubbled clusters. The double-bubbled $(ZnS)_{60}$ is more stable than $(ZnS)_{12}$ by 13.05 kJ/mol per ZnS unit.

The bubble type cluster of ZnS was also subject of a Density Functional Theory (DFT) study [83] where the authors used molecular dynamics (MD) and DFT to calculate the vibrational spectra and electronic structure of the clusters. The nucleation energy changed with cluster size but there was no apparent trend. It is suggested that the clusters with higher nucleation energies, will have faster growth and, therefore, will be the predominant species. The domination of the local coordination causes the band gap energy to not change significantly with cluster size. However, the band gaps of double bubble clusters are smaller than those of the single bubble clusters.

A combined approach using simulating annealing (SA), Monte Carlo Basin Hopping (MCBH) simulations and genetic algorithms (GA) was employed to study the global minima in the potential energy of titanium dioxide clusters [84]. MCBH is based on a deformation of the potential energy hyperspace [85]. The transformed potential energy, $\widetilde{E}_C$, is defined by:

$$\tilde{E}_C(X) = \min\{E_C(X)\} \tag{1.1}$$

Where X represents the vector of the nuclear coordinates and "*min*" means that the local energy minimisation is performed starting from configuration X. A series of flat steps make up the transformed potential energy and the height of each step is the energy value of the local minimum at that region. The search of this transformed landscape is performed by Monte Carlo, random changes are applied to the current configuration and either accepted or rejected depending on the Metropolis criteria. The advantage of the basin method is that the barriers have been lowered considerably and in some cases transitions have no barrier. GA is a search technique, which is based on the principles of natural evolution [86]. A GA comprises of three parts; mutation, crossover, and fitness selection [87]. These are applied cyclically and iteratively to fixed-size, finite populations consisting of a boundary condition that must be satisfied. All three operations must stay constant in the course of the algorithm. A GA can be applied to any problem as long the variables to be optimised (genes) can be encoded to form a string (chromosome). This approach has been applied to global optimisation of water clusters [88], aluminium clusters [89] and palladium-platinum clusters [90].

These three techniques were combined by using the final configuration of the SA 3000K simulation as the start of the MCBH search. The end structure of this MCBH search is likely to be the global minima, however, in case it is trapped in a local minimum, this end structure is then started as a seed for the next MD simulation at 2990K. This procedure is continued until a temperature is reached where the structural change is minimal with changing temperatures. The best structures found using SA-MCBH was then the starting point for a GA search to continue. The amount of configurational space explored gives confidence that a global minimum has indeed been found. The structures found for Ti_nO_{2n} clusters, where n=9-15, show a series of compact structures with titanium ions reaching high coordination as n increases. For n=11 onwards the particles have at least a central octahedron

surrounded by a shell of surface tetrahedral, trigonal, bipyramids, and square base pyramids.

A GA was applied to determine the structure and shape of MgO nanoparticles where one of the variables was the charge on the ions [91]. A charge of ±2 seems to overestimate the repulsion between magnesium and oxygen ions and generates an open cage structure consisting of four-, six- and eight-membered rings. These structures were generated using rigid ion models, but when an explicit term for polarisation was applied, a higher coordinated (bulk-like) cuboidal structure was generated. By changing the charge on the ions to ±1, the rock salt structure was formed and varying the charge in non-integer steps from ±1 to ±2, intermediate structures were observed ranging from cage structures to two stacked octahedral rings. Although the results of this work are still controversial, it is suggested that this method could be employed to examine the effect on size on the structures that were formed.

A further MD based method, simulated amorphisation and recrystallisation (A&R), has been developed to study mineral nanoparticles. This technique started by simulating thin films at oxide interfaces [92]. The A&R strategy differs from the simulated annealing method because the solid is heated and pressurised until it becomes glass-like. So the atoms have more degrees of freedom than in a solid but less degrees of freedom than in a liquid. Once the glass has been made you take a point in your crystal and start to recrystallise it. This has the advantage over simulated annealing because very big systems can be treated; however there is not a full sampling of configuration space. Thus, picking the point of recrystallisation is very important.

Sayle and co-workers have used molecular dynamics to explore the structures of nanoparticles supported on an oxide substrate [93], simulating nanoparticles of SrO, CaO and MgO on a BaO {100} surface. The resulting structures and morphologies of the supported nanoparticles differed considerably with the substrate oxide. In

particular the nanoparticles accommodated a wealth of structural defects. These defects included dislocations, grain boundaries, and vacancies. Sayle and Watson went further and simulated a 25000-atom nanoparticle on a metal oxide substrate [94]. The simulated A&R strategy was used to simulate the SrO nanoparticle on an MgO {100} surface. The nanoparticle again exposed defects and various facets at the surface.

Sayle *et al.* used atomistic simulations to generate a model for a $25nm^3$ CaO nanoparticle that has been encapsulated within the near surface region of an MgO lattice [95]. This was a development of the simulated A&R method, which again proved that the morphology of the nanocrystal could differ from its bulk structure, and still be stable. The system is stabilised due to the epitaxial configurations which include CaO {100}/MgO {100}. This facilitates energetically favourable cation-anion interaction across the interfacial region.

Simulated A&R was used to explore the microstructure of the mineral pyrolusite (MnO_2) [96]. The starting configuration was a cube of pyrolusite and by allowing the structure to evolve during the simulation, the end configuration contained small domains that closely conforms to a brookite (TiO_2) structure. The microstructure included micro-twinning, grain boundaries, isolated and associated point defects comprising of Mn^{4+} and oxygen vacancies, stacking faults and dislocations. The packing of the oxygen sub-lattice changed from an hcp to a ccp formation.

MD simulations can be used to describe another important process that occurs, especially during biomineralisation, namely the aggregation of nanoparticles. This evolved from a combined experimental and computational study into the phase stability of ZnS nanoparticles. It was determined by EXAFS and WAXS techniques that anhydrous ZnS nanoparticles, which were under 7nm in diameter, contained a very amorphous structure which was very similar to its sphalerite morphology. However the addition of water caused it to adopt a wurzite morphology, which was confirmed by an MD investigation [97]. The MD simulations predict that the polar

water molecules orient to permit hydrogen and oxygen bonding to the terminating sulphur and zinc ions. This has a very large stabilising affect on the crystal structure of the nanoparticle.

The phase stability of ZnS nanoparticles was studied during its aggregation process. Zhang and Banfield showed that this phase transformation of sphalerite to wurtzite could be caused by nanoparticle aggregation and coarsening [98]. 3nm ZnS nanoparticles were randomly orientated with respect to each other and allowed to aggregate to form a larger nanoparticle. Following aggregation, the coarsened particle adopts a near-amorphous structure that transforms rapidly to a wurtzite structure.

This work by Banfield and co-workers has provided a link between atomistic simulations and the forces that cause their aggregation, i.e. colloidal chemistry. This work has shown that atomistic simulations can describe the aggregation of nanocrystals. One part of colloidal chemistry looks at the forces of aggregation and separation of particles, as well as the conditions that helps or hinders this. The next section will review some of the relevant factors.

1.3 Theory of Colloidal Chemistry

Colloid science concerns systems in which one or more of the components has at least one dimension within the nanometre to micrometre range. The system is made up of a dispersed phase and a dispersion medium. An example would be if the dispersed phase was a solid and the dispersion medium was a liquid then the system would be known as a suspension solid (printing ink or toothpaste). Colloidal chemistry is interested in the intermolecular forces in the interfacial region of these micro heterogeneous systems.

1.3.1 Van der Waals Interactions

The van der Waals force is a long-range force acting between any surface in any media. The force has an electrodynamic origin based on the interactions between permanent and induced dipoles. Their correlation gives rise to attraction or repulsion depending on the orientation of atomic and molecular electric dipoles. There are three types of interactions that add up to the total van der Waals force [99]. The Keesom or orientation interaction is a dipole-dipole interaction, where the electric field created by a permanent dipole affects other permanent dipoles. The second part is known as the Debye or induction interaction. This is a dipole-induced interaction, where the field from a permanent dipole induces a dipole in a polarisable atom or molecule. The final interaction is known as London or dispersion interactions. This occurs when an induced dipole, created by a fluctuation of electronic charges, induces dipoles in other molecules.

1.3.2 Hamaker Constant

Dispersion-type forces between macroscopic objects were first treated by Hamaker in 1937 [100]. Hamaker used London-dispersion attraction between neutral atoms or molecules and assume additive sums over all the molecules of the macroscopic body. Additivity of forces is not correct for a real liquid phase but this is the convention. The van der Waals interaction energy for two macroscopic spheres of equal size, R, separated by distance D, is:

$$V_A(D) = -\frac{A}{6}\left[\frac{2R^2}{D^2-4R^2} + \frac{2R^2}{D^2} + \ln\left(\frac{D^2-4R^2}{D^2}\right)\right] \qquad (1.2)$$

Where A is the Hamaker constant and is a material property. The earliest expression for this interaction between two materials is expressed in terms of the number

densities, ρ_i, and a constant C known as the London constant, so that the Hamaker constant becomes:

$$A = \pi^2 C \rho_1 \rho_2 \tag{1.3}$$

Equation 1.3 is only valid for like materials in a vacuum. This is because the constant C is roughly proportional to the volume of an atom, which makes A roughly constant to whatever medium separates the interacting bodies. Typical values for the Hamaker constant of condensed phases are around 10^{-19} J for interaction across a vacuum. This is because if each body is composed of atoms for which C=10^{-77} J m^6 and a number density ρ= 3 x 10^{28}m^{-3} the Hamaker constant is:

$$A = \pi^2 10^{-77} \left(3x10^{28}\right)^2 \approx 10^{-19} J \tag{1.4}$$

In 1997, Bergstrom wrote a paper describing Hamaker constants of various inorganic materials using Lifshitz theory [101]. Lifshitz theory [102] was introduced because the theoretical microscopic approach presented by Hamaker is subject to a few limitations. The calculation is based on number densities and polarisabilities of atoms of interacting bodies and ignores the effect of the surrounding medium. There is also the effect of retardation, which is ignored by Hamaker. Retardation occurs when the distance between interacting bodies is so large that the propagation of the electromagnetic field can not be regarded as instantaneous. This electromagnetic field, which is created by the electron and nuclear motion of a molecule, moves through the surrounding space at the speed of light. If the distance is large enough the first molecule has a different dipole orientation when the reflected field from the interacting molecule has returned. This is an instance where the additivity of the Hamaker constant breaks down.

1.3.3 Lifshitz Theory

The problem of additivity is avoided in the Lifshitz theory. The original theory provided an alternative approach to calculate A and requires working knowledge of quantum field theory for its understanding. It ignores the atomic structure and the forces between large bodies, now treated in a continuous media and is derived in terms of bulk properties, such as their dielectric constants and refractive indices. Lifshitz theory is only valid when the interacting surfaces are further apart than molecular dimensions and the media are homogeneous with constant densities. Using Lifshitz theory you gain an expression for the van der Waals interaction energy per unit area between two half-spaces, composed of materials 1 and 2, separated by thickness D of material 3, becomes:

$$V_{132}(D) = -\frac{A_{132}(D)}{12\pi D^2} \tag{1.5}$$

The Lifshitz approach in determining the Hamaker constant unveils three interesting aspects:

1) The van der Waals force between two identical bodies in a medium is always attractive (A is positive); while if there are different bodies then it can be attractive or repulsive (A is negative).
2) The van der Waals force between any two condensed bodies in vacuum or air is always attractive.
3) The Hamaker constant for two similar media interacting across another medium remains unchanged if the media are interchanged.

Bergstrom's review provided data for non-retarded Hamaker constants from Lifshitz theory for 31 different inorganic materials. The accuracy of this relies on the dielectric spectral representation and quality of the experimental dielectric data of the materials and media [101].

1.3.4 Colloid Stability

The realisation of the existence of these relatively long-ranged attractive forces made possible the first theories of the stability of hydrophobic colloids as a balance between London attraction and electrical double layer repulsion. Deryagin and Landau [103] and Verway and Overbeek [104] independently developed a quantitative theory, known as DLVO theory, which was used to describe this balance of attraction and repulsion. The partition function for N simple ions of charge q_i arrayed at position r_i in the static potential $\Phi(r)$ is:

$$Q = Q_0 \int_{\Omega} dr_1 ... dr_i \exp[-\beta V(\{r_i\})] \tag{1.6}$$

Where:

$$V(\{r_i\}) = \frac{1}{\varepsilon} \sum_{i=1}^{N} q_i \Phi(r_i) \tag{1.7}$$

is the total Coulombic energy, the prefactor Q_0 (from equation 1.6) results from momenta, and

$$\beta^{-1} = k_B T \tag{1.8}$$

is the thermal energy at temperature T [105]. All charged species in the system, including the fixed microions, contribute to $\Phi(r)$. The microions also exclude simple ions from their interiors, so their volumes are excluded from volume of Ω. Equation 1.7 implicitly adopts the primitive model and approximates the solvent's influence through its dielectric constant, ε. The partition function can be expressed as a function integral over all possible simple ion distribution:

$$Q = Q_0 \int Dn \exp(-\beta f[n]) \tag{1.9}$$

Where *n(r)* is one particle simple ion distribution with an action:

$$\beta f[n] \approx \beta V[n] + \int_{\Omega} n \ln n d\Omega \tag{1.10}$$

Ω is the volume of the system and the prime on the integral in equation 1.9 indicates that the ions number is conserved:

$$\int_{\Omega} n d\Omega = N \tag{1.11}$$

This differs from the exact action by terms accounting for higher-order correlations among simple ions. Equation 1.10 yields a tractable but thermodynamically inconsistent theory. Minimising *f[n]* to implement the mean field approximation yields the Poisson-Boltzmann equation:

$$V_{\Phi}^2 = -\frac{4\pi}{\varepsilon} \sum_{\alpha} n_{\alpha} q_{\alpha} \exp(-\beta q_{\alpha} \Phi) \tag{1.12}$$

Where the subscript n_{α} is the concentration of simple ions of type α far from a charged surface. Even this has no analytic solution except for the simplest geometries. DLVO invoked the Debye-Huckel approximation to linearise the Poisson-Boltzmann equation. This gave a solution for the potential outside a sphere of radius, *a*, carrying charge, *–Ze*:

$$\Phi(r) = -\frac{Ze}{\varepsilon} \frac{\exp(Ka)}{1+Ka} \frac{\exp(-Kr)}{r} \tag{1.13}$$

In this approximation we obtain the effective pair potential by integrating equation 1.13 over a second sphere separated from the first by a centre to centre distance, *r*.

This assumes that the second sphere does not disrupt the first sphere's ion cloud. The resulting superposition yields a screened Coulombic repulsion for the inter sphere interaction:

$$U(r) = -\frac{Z^2 e^2}{\varepsilon}\left[\frac{\exp(Ka)}{1+Ka}\right]^2 \frac{\exp(-Kr)}{r} \tag{1.14}$$

The full DLVO potential includes a term accounting for dispersion interactions. These are negligibly weak for well separated spheres, however, and omitted from *U(r)*.

A dispersive phase is thermodynamically unstable with respect to the bulk. The survival of colloids must therefore be a consequence of kinetic collapse. However, colloids attract each other over large distances. The reason behind this is that the energy of attraction between two individual atoms, *i* and *j* are separated by a distance, R_{ij}, in each colloid particle varies at different separation by $\frac{1}{R_{ij}^6}$. The sum of these pair wise interactions however decreases approximately by $\frac{1}{R^2}$ where *R* is the separation of the centres of the particles. A precise sum of the pair wise interaction can be gained by knowing the shape of the particles. The sum has a much longer range than the $\frac{1}{R_{ij}^6}$ dependence, characteristic of individual particles and small molecules. A major source of kinetic stability of colloids is the existence of an electric charge on the particles. On account of this charge, ions of opposite charge tend to cluster nearby and the phenomenon of the electric double layer is seen.

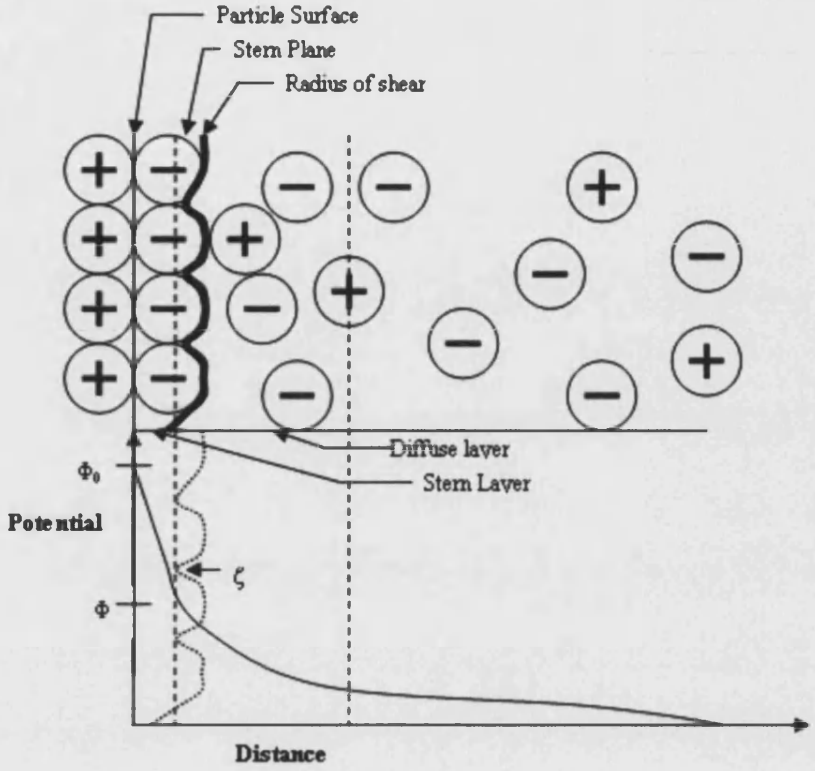

Figure 1.2: Schematic representation of the electric double layer

Figure 1.2 shows a schematic representation of the different layers that make up the electric double layer. The first of this double layer is a fairly immobile layer of ions that adhere tightly to the surface of the colloid particle. This immobile layer is known as the Stern layer and the radius of spheres that captures this rigid layer is known as the radius of shear. The radius of shear is a major factor determining the mobility of particles. The electric potential at the radius of shear relative to its value in the distant, bulk medium is called the zeta potential, ζ. The second layer is made up of an oppositely charged atmosphere of mobile ions that are attracted to the charged unit. This is known as the diffuse layer [105]. In the diffuse layer the ions can move freely and the net electric charge decreases exponentially with the distance away from the surface.

At high ionic strength, the ionic atmosphere is denser and the potential shows a secondary minimum at large separations. Aggregation of the particles arising from the stabilizing effect of this secondary minimum is called flocculation. This can be re-dispersed by agitation. This is summed up by the Schulze-Hardy rule [106, 107] which states that the hydrophobic colloids are flocculated most efficiently by ions of opposite charge type and high charge number.

The application of DLVO theory is used to predict the stability of useful colloidal systems, such as clay. Missana and co-workers used DLVO theory and the Hamaker constant to predict the stability of Na-montmorillonite colloids [108]. In this study they found that DLVO theory does not reliably predict the stability of their colloidal system due to the input parameters. In particular, they mention the fact that the Hamaker constant is a huge factor in this unreliability. They state that this theory is unable to take into account the contribution of the pH-dependent charge. However, Andersson *et al.* undertook a successful investigation into DLVO interactions of tungsten oxide and cobalt oxide surfaces with the colloidal probe technique [109]. Since there was no experimental data on the Hamaker constants for these materials they were calculated using the Lifshitz theory. The accuracy of this was determined via the accuracy of the dielectric response function. This study showed that the electrostatic interaction between oxidised tungsten and cobalt surfaces at a pH 10 is attractive.

Meurk *et al.* have tried to do direct measurements of van der Waals attractive and repulsive forces using AFM [110]. Their paper considered direct surface force measurements between inorganic materials in organic media, where the interactions were limited to a van der Waals force only. The experimental force curves resulted in attraction in both media for the symmetric systems and repulsion for the asymmetric systems. This agreed well with the theoretical predictions. However this work has yet to be tested against atomistic simulation.

1.4 Conclusions

Clearly there have been many advances recently in studying the interactions that occur at the mineral-water interface and now that computers are becoming increasingly powerful, more complex systems can be simulated. However, some key issues still remain unanswered:

- How does the structure of the surface influence the surface of water around it?
- Can dissolution of ions from mineral surfaces be simulated with a dynamic model of water included?
- Can a reliable potential be derived to describe the interactions between polymeric additives and mineral surfaces?
- Can atomistic simulations be used to determine the reactivity of mineral nanoparticles?
- Can the aggregation process of mineral nanoparticles be quantified?

These questions are addressed in this thesis. However, before presenting recent progress in modelling the mineral-water interface, the potentials used to model the interactions at this interface are described.

Chapter 2

The Potential Model-Theory and Derivation

All of the simulations described in this thesis require the evaluation of the forces between the atoms. *Ab initio* calculations may give a very accurate description of many important processes on mineral [111, 112] and metal surfaces [113, 114]. However, the calculations of the forces from electronic structure calculations are very computational expensive, the sizes of the systems are relatively small and the amount of real time that can be simulated is very short. Therefore, it is not yet viable to use these techniques to simulate processes such as the aggregation of mineral oxide nanoparticles, or the adsorption and dissolution of ions across the solid-liquid interface.

A faster and less computationally expensive method is to use parameterised interatomic potentials to evaluate the forces. Thus in this thesis we have used interatomic potentials and this chapter will describe the components of these potentials, which can be further sub divided into long-range and short-range interactions. The accuracy of the calculations performed using interatomic potentials is largely due to the reliability of the potential parameters, therefore, in this chapter we will give a full description of the parameters used and how they were derived. The Born model of solids is the basis for the description of long- and short-range forces and therefore be described first.

2.1 The Born Model of Solids

The Born model of solids [115] is used to describe the interactions of ionic or polar solids. This model assumes a formal charge on each atom. Using this approach the lattice energy, U, is defined as the sum of all pair wise interactions, between atoms i and j. Thus enabling the lattice energy to be written in the form:

$$U(r_{i,j}) = \sum_{i}^{N} \sum_{\substack{j \\ j \neq i}}^{N} \frac{q_i q_j}{4\pi\varepsilon_0 r_{i,j}} + \sum_{i}^{N} \sum_{\substack{j \\ j \neq i}}^{N} \phi_{i,j}(r_{i,j}) \tag{2.1}$$

The first term describes the long-range electrostatic interactions and the second term describes the short-range contribution which is calculated using adjustable parameters dependent on the interaction in question.

2.2 Long-Range Interaction

The Born model has Coulombic interactions, which account for the majority of all interactions in an atomistic simulation. When two atoms are brought together from

infinity, to their lattice sites, the electrostatic contribution to the lattice energy is released. Therefore, the potential energy of the long-range interactions takes the form:

$$\psi = \sum_{l,i,j}' \frac{q_i q_j}{4\pi\varepsilon_0 (r_{i,j} + l)} \tag{2.2}$$

Where q_i and q_j are the charges on the ions i and j, $r_{i,j}$ is the displacement of ion i from ion j and l is the set of lattice vectors representing the periodicity of the crystal lattice. The problem with equation 2.2 is that it has a $1/r$ term has poor convergence. Fortunately, many alternatives exist and the two described in this thesis were originally suggested by Ewald [116] and Parry [117, 118].

2.2.1 Ewald Summation

The Ewald summation [116] assumes that the unit cell is periodic in three dimensions. This method over comes the problem that occurs in the Coulombic summation by splitting it into real and reciprocal space. Each ion is effectively neutralised, at long range, by the superposition of a Gaussian distribution of opposite charge on the ion. By combining the point charges and Gaussian distribution this becomes the real space part of the Ewald sum. A second modification is to superimpose a second set of Gaussian charges, this time with the same charge as the original point ions and again centred on the point ions. This second set of Gaussians cancel out the effect of the first set of Gaussians and here we are left with the charge distributions of just the point charges. The potential due to these Gaussians is obtained from Poisson's equation and is solved as a Fourier series in reciprocal space.

The total potential at an ion is the sum of two distinct but related potentials:

$$\Psi_i = \Psi_1 + \Psi_2 \tag{2.3}$$

The potential Ψ_1 is that of a structure with a Gaussian distribution of charge situated at each ion site, whose sign is the same as on the real ion. The charge distribution on the reference point is not considered to contribute to the potential Ψ_1 or Ψ_2. We therefore calculate the potential Ψ_1 as the difference of two potentials, Ψ_a and Ψ_b.

$$\Psi_1 = \Psi_a - \Psi_b \tag{2.4}$$

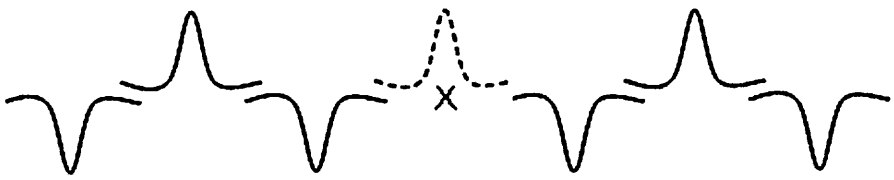

Figure 2.1: Charge distribution used to computing potential Ψ_1

Ψ_a is the potential of a continuous series of Gaussian distributions (including the dashed curve at reference point X in figure 2.1). Ψ_b is the potential of the single (dashed) Gaussian distribution on the reference point X.

The potential Ψ_2 is that of a lattice of point charges with an additional Gaussian distribution of the opposite sign superposed upon the point charges.

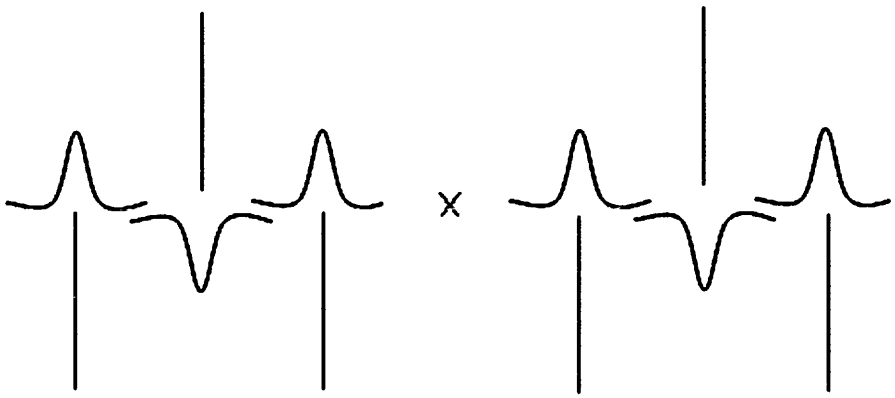

Figure 2.2: Charge distribution for potential Ψ_2. The reference point is denoted by an X.

By splitting the problem into two parts we are able to find a suitable choice of parameters to determine the width of the Gaussian peak [119]. The rapidity of convergence is dependent only on the width of the Gaussian peak, although the actual value for the total potential is independent of the width parameter. In fact, the Gaussian distributions drop out completely on taking the sum of the separate charge distributions giving rise to Ψ_1 and Ψ_2.

The total charge at point r can be seen as:

$$\rho(r) = \left[\delta(r_i, r_{lattice}) - \exp\left(\frac{(r_i - r_{lattice})^2}{\eta}\right)\right] + \exp\left(\frac{(r_i - r_{lattice})^2}{\eta}\right) \qquad (2.5)$$

Where $\delta(r_i, r_{lattice})$ takes the value 1 if r_i represents a lattice site and zero otherwise. The first term is the interaction associated with Ψ_2 by using Poisson's equation 2.6.

$$\nabla^2\psi = \rho(r) \qquad (2.6)$$

This gives the potential of the first term as:

$$\psi_2(r) = q_i \sum_j \frac{q_i erfc(\eta r_{i,j})}{r_{i,}j} \tag{2.7}$$

Where $erfc(\eta r_{i,j})$ is the complementary error function and takes the form:

$$erfc(x) = 1 - \left(\frac{2}{\sqrt{\pi}}\right)\int_0^x \exp(-t^2)dt \tag{2.8}$$

The second term in equation 2.5 is associated with Ψ_1 and represents the compensating charge distribution, which is solved by means of Fourier transforms. In transform space, the function converges rapidly to give a series of Gaussians of the form:

$$\rho(r) = \sum_k (C_k \exp(iKR)) \tag{2.9}$$

Where K represents the reciprocal lattice vectors and R is $(r_i - r_{lattice})$ for all ions in the unit cell. If Poisson's equation is used again, the potential for Ψ_1 becomes:

$$\psi_1(r) = q_i \sum_i \left[\frac{q_i}{\pi V_k} \sum_k \left(\frac{\exp(-\pi^2 k^2 \eta^2)\exp(iKR)}{k^2}\right)\right] \tag{2.10}$$

This model assumes that the cell is always charge neutral, therefore the sum of the charges is always zero.

The above equations sums all possible interactions of ion i and j in the entire lattice including the interaction of atom i with itself. This feature is due to the fact that this summation takes place periodic in 3-dimensions. This self interaction is removed by

including equations 2.7 and 2.10 into equation 2.3 and including an extra term to describe self interaction. Therefore equation 2.3 can be re written as:

$$\psi_i = q_i\left[\frac{q_i}{\pi V_k}\sum_{\substack{k\\k\neq 0}}\left(\frac{\exp\left(-\pi^2k^2\eta^2\right)\exp(iKR)}{k^2}\right)\right]+q_i\sum_j\left(\frac{q_j erfc(\eta r_{i,}j)}{r_{i,}j}\right)-\frac{2q_i^2\eta}{\sqrt{2}} \quad (2.11)$$

2.2.2 Parry Summation

The Parry summation [117, 118] is an adaptation of the Ewald summation for crystals periodic in 2-dimensions, i.e. surfaces. The crystal is assumed to consist of a series of charged planes of infinite size rather than an infinite lattice. When summing the electrostatic interactions, the vectors are now divided into in-plane vectors and vectors perpendicular to the plane. This means the sum of the charges on a plane can no longer be assumed to be zero. The term involving the reciprocal lattice vector must be evaluated and a detailed derivation of the Parry summation is given by Heyes *et al.* [120].

The problems of trying to overcome the convergence in the long-range interactions have been described above by applying Ewald and Parry summations. In this thesis we converge the sums to 10^{-6} eV. The next part of the chapter will consider various techniques for modelling the short-range interactions.

2.3 Short-Range Interaction

In its simplest form, the short-range interactions can be thought of in two parts. At very short distances there is repulsion between the two ions as the electron clouds come together. As the separation increases an attractive part, which describes the

van der Waals forces between the ions can become significant. As we start to consider many-body interactions then other terms such as bond bending and angles can be described.

Throughout this work the short-range interactions are parameterised models which are used to describe the attractive and repulsive contributions. In order to obtain reliable quantitative results it is important that the parameters used accurately describe the lattice properties. Therefore there needs to be careful consideration of the parameters used. The short-range potentials used in this thesis are described below.

2.3.1 The Lennard-Jones Potential

The Lennard-Jones potential is an approximation that describes the complicated nuclear and electronic repulsions.

$$\phi_{i,j} = \frac{A}{r_{i,j}^{12}} - \frac{B}{r_{i,j}^{6}} \tag{2.12}$$

The first term models the repulsion between ions when brought very close together. Its physical basis derives from the fact that when the electronic clouds start to overlap the energy of the system increases. The exponent 12 was chosen exclusively on a practical basis since it makes the equation easy to compute. Having already worked out $1/r^6$, the repulsive term is simply the square of this multiplied by A_{ij}. At large distances the second term dominates and makes up the attractive part of the potential. A $1/r^6$ attraction models the van der Waals dispersion forces, which is caused by instantaneous dipole-dipole interactions. The parameters A and B are chosen to fit the physical properties of the material.

2.3.2 The Buckingham Potential

The Buckingham potential has been widely used due to its success in modelling ionic systems [121]. As with the Lennard-Jones potential, the first part represents the repulsion between the negatively charged electron clouds while in the second term the attractive the van der Waals interaction between ions are described:

$$\phi_{i,j} = Ae^{\frac{-r_{i,j}}{\rho}} - \frac{C}{r_{i,j}^6} \tag{2.13}$$

Where A, ρ and C are parameters which differ for each pair of interacting ions and r is the distance between ion i and ion j. The exponential in the first part of equation 2.13 enables the repulsive component to be more flexible than the Lennard-Jones potential and is more widely used in the simulation of polar solids.

The use of Lennard-Jones and Buckingham potentials do constitute extremely important model systems. It can not be over-estimated the importance of these potentials in gaining an insight into some important properties in a variety of different conditions. Examples include investigations in solids [122-124], surfaces [61, 125], and clusters [126-128].

2.3.3 The Morse Potential

This potential is used to model the two-body component of covalently bonded interactions, such as atoms in molecular ions.

$$V_{(ri,j)} = A_{i,j}\left(1 - \exp\left[-B_{i,j}\left(r_{i,j} - \phi_{i,j}\right)\right]\right)^2 - A_{i,j} \tag{2.14}$$

Where $A_{i,j}$ is the bond dissociation energy, ϕ_{ij} is the equilibrium bond distance and $B_{i,j}$ is related to the curvature of the slope of the potential energy well and can be obtained by spectroscopic data.

2.3.4 Many Body Potentials

There are many ways of introducing many body potentials into atomistic simulation, each adopted by different communities. The metal and semi-conductor communities use potentials that have density dependent terms. The molecular modellers use angle dependent terms, whereas those from the polar solid community use shell models. In this work we use many body terms from the latter two communities. The three body potential is used for modelling the angular dependence of covalent materials. Changes in interaction energies are caused by deviation from the equilibrium bond angle, θ, which is described as the angle between a central ion i, and two adjoining ions j and k.

$$\Phi_{i,j,k} = \frac{1}{2} K_{i,j,k} (\theta - \theta_o)^2 \tag{2.15}$$

$K_{i,j,k}$ is the harmonic force constant and θ is the bond angle. The term can only be zero when the bond angle is equal to the equilibrium angle $(\theta = \theta o)$.

A discussion of how the potential parameters mentioned above are derived can be found later in this chapter. In the next section we shall describe how we can account for polarisable ions using the shell model.

2.3.5 The Shell Model

The many body potential used extensively by those modelling polar solids is the shell model. There have been some very successful investigations performed using rigid ions. This is where each ion addressed is a formal point charge. Although simplistic, this type of model has been found to work well over a wide range of systems [129-131]. Indeed there are several studies involving a comparison between the results provided by rigid ion and a polarisable ion system [132-134]. In each case the shell model has been shown to be superior, and only neglected because of the higher computational cost.

In this work, the shell model is used on all anions developed by Dick and Overhauser [135]. This model treats the electron cloud of the ions as a separate species.

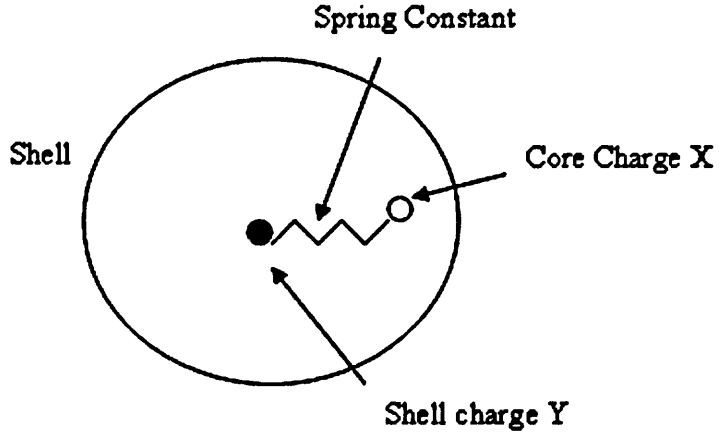

Figure 2.3: Schematic representation of the shell model

In this model (figure 2.3) an ion is represented by a core and a shell. The core, which contains all the mass of the ion, is attached to the shell by a harmonic spring. The total charge of the ion is shared between the core and the shell. The ion polarisability, α, is related to the shell charge, Y, and the spring constant, k.

$$\alpha = \frac{Y^2}{k} \tag{2.16}$$

The harmonic core-shell potential is used to model the interactions between the negatively charged electron cloud and the positively charged nucleus. An extension to the shell model is the breathing shell model, which was introduced by Schroder in 1966 [136]. This allows the shell to distort spherically thus adding another degree of freedom. An advantage of this method is that when the ions environment changes the polarisability also changes. However it has the disadvantage of requiring two new parameters for evaluation. The computational cost of using this model is that the number of species involved in the computer simulation is doubled. Catlow *et al.* provides a detailed discussion of polarisable ions and its effects [137].

The shell model has been adapted and extended to give a more accurate representation of polarisation. An example of this is the aspherical ion model (AIM) which was developed by Madden and co-workers [138, 139]. Madden and co-workers showed how the results of electronic structure calculations on a wide range of condensed phase configurations can be used to construct models for the inter-ionic forces and simultaneously for the multipoles on the ions due to their interactions. The models reproduce the *ab initio* dipoles and quadrupoles and therefore necessarily include a reliable account of the polarization contributions.

The remainder of the chapter considers methods by which reliable parameters for these potentials are derived, before considering the potentials used in this work.

2.4 Derivation of Potential Model

As noted previously, the quality of a potential is dependent on the appropriate choice of potential parameter. In general, there are two possible ways of deriving inter-atomic potential parameters. Firstly, the parameters can be adjusted to

reproduce data by *ab-initio*, electronic structure, calculations. Normally the total energy of the system is the variable with respect to an atom position. Alternatively it is possible to derive empirical potentials by trying to reproduce experimental data. Until recently, the second approach has proved more practical since electronic structure calculations are time consuming and computationally expensive. However, with the introduction of efficient software packages such as VASP [140], CASTEP [141], and SIESTA [142], it has meant that non-empirical fitting has become a practical alternative. Although it should be recognised that these DFT codes do neglect long-range van der Waals terms and often have difficulties with open shell transition metals, so that they are far from prefect.

2.4.1 Least Squares Fitting

No matter which method of fitting is used the aim of this is the same; to develop a model that will reproduce the existing data as accurately as possible. The statistical quantity most often used to measure this is the sum of squares. Ideally, this should be zero, however, in practice this will only happen for trivial cases. This is where the potentials can be guaranteed to completely reproduce the data and in most cases a value within a confidence limit of zero is expected. The sum of squares F is defined as:

$$F = \sum_{observables} w\left(f_{calc} - f_{obs}\right)^2 \tag{2.17}$$

Where f_{calc} and f_{obs} are the calculated and observed quantities and w is a weighting factor. There is no such thing as a unique fit since the final parameters will depend on the choice of weighting factor for each observable. The choice depends on several factors, such as the relative magnitude of the quantities and the reliability of the data.

The aim of fitting is to minimise the sum of squares by varying the potential parameters. There are several standard techniques for solving least squares problems. The simulation package GULP (General Utility Lattice Package) [143] uses a Newton-Raphson functional minimisation approach to solving the problem. This way avoids storing the co-variance matrix. One disadvantage is that near-redundant variables are not eliminated.

2.4.2 Fitting to energy surface

The release of reliable electronic software packages means that there is now a reasonable expectation of calculating, at least for a model system, a potential energy surface for a material. These codes also give the forces acting on each atom which can be used to determine the potential model.

When fitting an energy surface there is the need to include an energy shift because in some cases the self-energy of the atom is different for the two types of simulation. Currently, it is assumed to be a single additive energy term, which is the same for all structures and just moves the energy scale up and down. The justification of this is that often it is impossible to calculate the energy that corresponds exactly to their inter-atomic potential from a quantum mechanical calculation [144].

2.4.3 Empirical fitting

An alternative to the above fitting method is to fit the potential to existing experimental data. In this case the procedure serves two purposes:

1) The degree to which all data can be reproduced may serve as some guide as to how well the model used relates to the physical system of interest.

2) It provides a means of extrapolation of experimental data from one system to another. This is where the data may not be known or alternatively there may be unknown properties of the same material.

Essential properties can be derived using empirical fitting such as the experimental structure. The conventional way to obtain a potential is to adjust the parameters so that the forces on the atoms, at an experimentally determined structure, is zero. This is not a prefect strategy as a transition state rather then a minimum could satisfy it. In practice this is rare, except when symmetry constraints are imposed.

In very highly symmetric systems, like rock salt, the structural information alone is inadequate and the potential needs to be expressed as a binominal expansion of the experimental geometry. The first and second derivative need to be well reduced by the model otherwise the range of transferability will be poor. Typical sources of second derivative information are elastic, dielectric and piezoelectric constants.

Empirical derivations of potential parameters have been successful for a range of structures and techniques. Examples include: TiO_2 surfaces [129], morphology of carbonates [145] and oxygen vacancies on ceria surfaces [146]. A major disadvantage of the least squares fitting of energy surfaces and empirically data is that only a final set of parameters is obtained so there is no insight on the effect of the parameters on properties. Also the approach is essentially static, by fitting only certain configurations.

Having discussed the theory involved in deriving reliable interatomic potentials, we will now describe the potentials used in this work.

2.5 Potentials used in this work

In this section the potential parameters used in this thesis are discussed. Most of these are short-range interaction parameters that are found in previously published work [65, 68, 147]. However, in several cases, potential parameters have had to be derived for this study. This occurred when no suitable parameters could be found, or, when the available parameters were judged to be unsuitable. Although the full description of the modifications is in the relevant chapter, the final set of preferred potentials is reproduced here.

2.5.1 Magnesium-Oxygen Potential Parameters

The magnesium-oxygen potential parameters used in this study are those first reported by Lewis and Catlow [121]. A shell model is applied for the oxygen but the cation is considered to be unpolarisable. The positive charge reduces the polarisibility of the shell. In addition, many models derive positive shell charges for cations which is counter intuitive and hence the core position does not reflect the true position. The parameters were derived empirically and tested against experiment structures, lattice parameters, elastic and dielectric constants.

Buckingham potentials are used to describe all the interactions considered and the parameters used are shown in table 2.1.

Table 2.1: Magnesium oxide potential parameters

Magnesium Oxide			
Ion	Charges (e)		Core-shell int. eV $Å^{-2}$
	Core	Shell	
Magnesium (Mg)	2.000	-	-
Oxygen (O)	0.848	-2.848	74.92038

Buckingham Potentials			
Ion Pair (ij)	$A_{(ij)}$/eV	$\rho_{(ij)}$/Å	$C_{(ij)}$/eV$Å^{-6}$
Mg Core O Shell	1428.5	0.2945	0.00
O Shell O Shell	22764.0	0.1490	27.88

These potential parameters have had a long and distinguished career and have been applied to a variety of simulations, including MgO surfaces [148], thin films of oxides on oxides [92, 149], grain boundaries [62, 150], and solid-water interfaces [65]. This shows that this potential is transferable to number of situations and has the ability to give reliable results.

2.5.2 Calcite Potential Parameters

Dove *et al.* developed one of the first interatomic potentials to give comparable results for the structure and properties of calcite [151]. Another successful early interatomic potential for calcite was developed by Pavese *et al.* in 1992 [152]. This model used Buckingham potentials for the calcium-oxygen, oxygen-oxygen, and carbon-oxygen interactions. To account for the molecular structure of the carbonate group, three and four body potentials were also included. As in the magnesium-oxide potential described above a shell model was included on the oxygen ions. The potential parameters were fitted to structural properties, elastic constants, and

vibrational frequencies. The fitting process was performed at zero Kelvin so therefore neglects the effect of temperature.

Table 2.2: Calcite potential parameters

Calcite			
Ion	Charges (e)		Core-Shell int. eV $Å^{-2}$
	Core	Shell	
Calcium (Ca)	2.000	-	-
Carbon (C)	1.135	-	-
Oxygen (Oc)	0.587	-1.632	507.4

Buckingham Potentials			
Ion Pair (ij)	$A_{(ij)}$/eV	$\rho_{(ij)}$/Å	$C_{(ij)}$/eV$Å^{-6}$
Ca-Oc	1550.0	0.2970	-
Oc-Oc	16372.0	0.2130	3.47

Morse Potentials				
Ion Pair (ij)	$D_{(ij)}$/eV	$\alpha_{(ij)}$/$Å^{-1}$	r_0/Å	Coulombic subtraction (%)
C-Oc	4.71	3.80	1.18	0

Three- and Four-Body Potenials		
Ions	K/ eV rad^2	θ_o (°)
Oc-C-Oc	1.69000	120
Oc-C-Oc-Oc	0.11290	180

An improved calcite potential, where the Buckingham potential between the carbon-oxygen was replaced by a Morse potential, was introduced in 1996 [147]. Using lattice dynamics techniques, Pavese *et al.* obtained good agreement with experimental cell dimensions, bond lengths and thermal expansion coefficients at

several temperatures. The potential parameters developed by Pavese *et al.* in 1996 are shown in table 2.2 and used in this work.

This potential has also been shown to be versatile by reproducing simulation of growth on flat [153] and stepped and kinked surfaces [66, 69], the calcite-water interface [67, 154], and biomineralisation processes [155, 156].

2.5.3 Water Potential Parameters

The water potential used in this work is a modified version of the de Leeuw and Parker potential [65]. The de Leeuw and Parker potential was published with a polarisable model for water, whereby the oxygen polarisability was accounted for by a shell model. The potential parameters were derived to reproduce the experimental dipole moment, infrared frequencies, OH bond length, the HOH angle of the water monomer and also the structure of the water dimer. A Morse potential, of which the B parameter was fitted to infrared frequencies, was used to model the O-H intramolecular interactions. The O-O intermolecular forces were modelled with a 12-6 Lennard-Jones potential and the potential parameters were fitted to reproduce the water dimer structure. The O-H intermolecular interactions were described by a Buckingham potential. A three-body harmonic potential was also introduced to reproduce the directionality of the covalent bond. Finally, to try and mimic the effect of the lone pairs of the oxygen atoms, the electrostatic interactions between the hydrogen atoms and between the oxygen and hydrogen atoms of a water molecule were partially removed, thus making the hydrogen atoms less repulsive.

This model provided a good representation of the diffusivity and energy of interaction, however, the next nearest oxygen position is overestimated and hence so is the density. For short molecular dynamics simulation this potential worked well but for longer simulations (of the order of 300ps and above) the model was

shown to freeze. Therefore Kerisit and Parker in 2004 [68] replaced the Buckingham O-H intermolecular potential with a Lennard-Jones intermolecular potential. This enabled the potential to be run for a longer simulation (of the order of 1-2ns) with no freezing. Table 2.3 shows the water potential parameters used in this study.

Table 2.3: Water potential parameters

Water			
Ion	Charges (e)		Core-shell int. $eV.Å^{-2}$
	Core	Shell	
Water Oxygen (Ow)	1.250	-2.050	209.45
Water Hydrogen (Hw)	0.400	-	-

Lennard-Jones Potentials				
Ion Pair (ij)	$A_{(ij)}$ eV. $Å^n$	$B_{(ij)}$ eV.$Å^m$	n	m
Ow-Ow	39344.98	42.15	12	6
Hw-Ow	24.00	6.00	9	6

Morse Potentials				
Ion Pair (ij)	$D_{(ij)}$/eV	$\alpha_{(ij)}/Å^{-1}$	r_0/Å	Coulombic subtraction (%)
Ow-Hw	6.203713	2.22003	0.92376	50
Hw-Hw	0.00000	2.8405	1.50000	50

Three-body Potentials		
Ions	k $eV.rad^2$	θ (°)
Ow-Hw-Ow	4.19978	108.69

2.5.4 Mineral-Water Potential Parameters

The majority of the results presented in this study concerns processes at the mineral water interface. Chapter 4 is concerned with the calcite-water interface and the potential parameters used is that of Kerisit and Parker [66, 68] which was derived to be compatible with that of de Leeuw and Parker [157]. Buckingham potentials are used to describe the carbon-oxygen water, calcium-oxygen water and carbonate oxygen-water oxygen interactions. The potential parameters were derived so that a repulsive potential between the carbon atom in the carbonate group and the water oxygen was added to prevent unrealistic close contact. The water hydrogen-carbonate oxygen Buckingham potential was replaced by a 12-10 Lennard-Jones potential to improve agreement with the structure and energy of a monolayer on the $\{10\bar{1}4\}$ calcite surface. This was obtained from electronic structure calculations.

Chapter 5 is concerned, in part, with the magnesium oxide-water interface. The potential parameters are that of de Leeuw and Parker [65]. The magnesium-water oxygen interaction was modified from the magnesium-oxygen potential to compensate for the reduction in electrostatic interaction due to the former's fractional charge. The C parameter of the Buckingham potential function between lattice oxygen ions was also modified for the interactions between lattice oxygen ions and water oxygen ions assuming this represents London dispersion forces. Table 2.4 shows the mineral-water potential parameters used in this thesis.

Table 2.4: Mineral-Water Potential Parameters

Buckingham Potentials			
Ion Pair (ij)	$A_{(ij)}$/eV	$\rho_{(ij)}$/Å	$C_{(ij)}$/eVÅ^{-6}
C-Ow	435.0	0.3400	-
Ca-Ow	1186.6	0.2970	-
Oc-Ow	12533.6	0.2130	12.09
Mg-Ow	490.0	0.2945	-
O-Ow	22764.0	0.1490	28.92
Hw-O	396.27	0.25	-

Lennard-Jones Potentials				
Ion Pair (ij)	$A_{(ij)}$ eV. Å^n	$B_{(ij)}$ eV.Å^m	n	m
Hw-Oc	26.00	1.80	12	10

2.5.5 Mineral-Salt Water Potential Parameters

In order to increase the complexity of our simulations and make them more comparable to experiments we have considered the interaction of magnesium oxide in contact with salt water. The sodium chloride potential is that derived by Catlow *et al.* [124]. The chloride-water potential was derived by reproducing the structure and energetics of small halide-water cluster obtained by *ab initio* calculations by Kerisit *et al.* [158], whilst the sodium-water potential was based on that derived by Post and Burnham [159].

The calculations involving magnesium oxide-salt water interactions used the same sodium-water and chloride-water potential parameters as described above. However, there are no suitable magnesium-chloride potential parameters. In the literature there are a few examples of a magnesium-chloride potential being used [160-162] but these simulations have only considered the β- $MgCl_2$ structure. This is

important in the study of Ziegler-Natta catalysis. However, both the α- and β-$MgCl_2$ structures are abundant and only differ in the stacking of the layered structure [162]. Thus potential parameters were derived using both α- and β- $MgCl_2$ structures via the GULP program [143] and tested in DL_POLY [163]. The Mg-Cl potential parameters were varied while the chlorine-chlorine potential was the same as for NaCl. A full description of the derivation of the potential parameters and calculated crystal structures can be found in chapter 5.

Table 2.5: Mineral-salt water potential parameters

Sodium Chloride			
Ion	Charges (e)		Core-shell int. $eV.Å^{-2}$
	Core	Shell	
Sodium (Na)	1.0	-	-
Chlorine (Cl)	1.485	-2.485	29.38

Buckingham Potentials			
Ion Pair (ij)	$A_{(ij)}$/eV	$\rho_{(ij)}$/Å	$C_{(ij)}/eVÅ^{-6}$
Na-Cl	2314.70	0.2903	-
Na-Ow	2334.72	0.2387	-
Cl-Cl	1227.200	0.3214	29.06
Mg-Cl	772.9200	0.3430	-
O-Na	1226.840	0.3065	-

Lennard-Jones Potentials				
Ion Pair (ij)	$A_{(ij)}$ eV. $Å^n$	$B_{(ij)}$ eV.$Å^m$	n	m
Cl-Ow	0.045	3.48	12	6
Hw-Cl	0.03	2.38	9	6

2.5.6 Polymeric Additive Potential Parameters

Chapter 4 also considers the interaction of polyelectrolyte solutions on calcite surfaces. The polymeric additive in question is the calcium and sodium salts of polyacrylic acid (PAA). The PAA model is an oligomer consisting of 10 monomers and is assumed to be completely deprotonated. The charge on the polymer is -10 and the charge of each individual ion in the chain was determined by running the monomer through GAUSSIAN 03 [164]. GAUSSIAN 03 is an electronic structure computer program that predicts energies, molecular structures and vibrational frequencies of molecular systems. Geometry optimization was performed until a stationary point on the potential surface was found, and from this geometry the Mullikan charges were assigned to the ions of the polymer. The force field used to describe the potential energy of the geometry was a CHARMM22 force field [165], which is the 22nd version of the CHARMM program [166]. The CHARMM force field is a highly flexible computer program which uses empirical energy functions to model macromolecular systems. The potential energy of a molecule is expressed as a superposition of valence (or bonded) interactions that depend on the bonds of the structure and the non-bonded interactions. This depends only on the distance between the atoms. The valence interactions consist of a bond stretch, bond angle, dihedral angle torsion, and improper dihedral angle force constants. The non-bonded interactions consist of Coulomb, Lennard-Jones 6-12 and hydrogen bonding terms.

CHARMM describes the bond stretching and bond angles by use of a small harmonic approximation. The torsion energy term is a four-atom term based on the dihedral angle about an axis defined by the middle pair of atoms:

$$E\phi = \sum \left| k_\phi \right| - k_\phi \cos(n\phi) \tag{2.18}$$

Where n can equal 1,2,3,4,6. The energy constant may be negative, which indicates a maximum at the *cis* conformation. Also there may be several contributions with

different k_φ periodicities for a given set of four atoms. The improper torsion term has been designed both to maintain chirality about a tetrahedral extended heavy atom and to maintain planarity about certain planar atoms, such as a carbonyl carbon. In addition, the improper torsion term provides a better force field near the minimum-energy geometry, which is important for dynamics and vibrational analysis. The force constants are obtained by fitting to vibrational data and geometric constants are derived from crystallographic data.

The non-bonded terms describing van der Waals interactions are Lennard-Jones exponential-6 form. The non-bonding interactions between the crystal surface and the polymeric additive were derived by Duffy and Harding [76] from the CHARMM22 interactions for the Ca^{2+} and CO_3^{2-} ions and the head groups of Langmuir monolayers. A full description of the how we tested this potential for reliability is provided in chapter 4. Table 2.6 shows the polymeric additive potential parameters.

Table 2.6: Polymeric additives potential parameters

Polyacrylic Acid	
Ion	Charge (e)
Terminal CH_3 Carbon (T)	0.00
Backbone CH_2 Carbon (X)	-0.03
Carbonyl Carbon (C1)	0.37
Carbonyl Oxygen (A)	-0.67

Buckingham Potentials			
Ion Pair (ij)	$A_{(ij)}$/eV	$\rho_{(ij)}$/Å	$C_{(ij)}$/eVÅ^{-6}
Ca-A	815.80681	0.2970	-
Oc-A	9557.05860	0.2130	7.47
Na-A	410.99000	0.3065	-

Lennard-Jones Potentials				
Ion Pair (ij)	ε (eV)	σ (Å)	n	m
Ca-Cl	0.0039767	2.9998	12	6
Na-Cl	0.0039767	2.9998	12	6
Oc-Cl	0.0039767	3.2963	12	6
Ow-T	0.0056837	3.4760	12	6
Ow-X	0.0056837	3.4760	12	6
Ow-Cl	0.0039767	3.2963	12	6
Ow-A	0.0052070	3.0290	12	6
Hw-A	0.0032243	1.7145	12	6
Hw-Cl	0.0024625	1.9818	12	6
Hw-X	0.0035160	2.1615	12	6
Hw-T	0.0036451	2.0700	12	6
T-T	0.0065699	3.7400	12	6
T-X	0.0064268	3.8230	12	6
T-A	0.0058876	3.3845	12	6
T-Cl	0.0049707	3.6518	12	6
X-X	0.0062044	3.9230	12	6
X-A	0.0056837	3.4760	12	6
X-Cl	0.0043416	3.7433	12	6
Cl-Cl	0.0030264	3.5636	12	6
Cl-A	0.0039767	3.2963	12	6
A-A	0.0052070	3.0290	12	6

This chapter has described the interatomic potentials used to describe the interactions used in atomistic simulations. The next chapter will discuss the different computational techniques used in this thesis.

Chapter 3

Theoretical Methods

The previous chapter detailed the potential models used to describe the interatomic interactions. This chapter will describe the theoretical and computational techniques used to apply these potentials in order to gain information. Two atomistic simulation techniques have been employed in this thesis. The first technique is energy minimisation (EM). As the name suggests, this technique is used to minimise the total interaction energy so that the system reaches mechanical equilibrium. This technique has been used in the past, with great success to investigate the structure and stability of minerals in bulk [167, 168] and mineral surfaces [148, 169]. As with all techniques it has advantages and disadvantages. EM is a relatively fast technique; however this approach neglects the effect of temperature as the calculations are effectively performed at zero Kelvin. The second method we shall describe is called molecular dynamics. This approach includes the effect of temperature and allows the kinetic energy evolve with time to

sample low energy configurations. It is computationally more expensive then energy minimisation but is vital when trying to describe the interactions of liquids [65, 158, 170]. This chapter will also include different approaches for modelling 2-dimensional mineral surfaces and also 3-dimensional nanoparticles.

An important consideration when modelling materials is the choice of periodic boundary conditions, which are discussed next.

3.1 Periodic Boundary Conditions

Periodic boundary conditions are a common feature in solid-state computational chemistry as it is useful for describing crystalline solids. These are applied to lattice simulations in order to simulate an infinite system with a finite number of images. The simulation cell is surrounded by an infinite number of images. When a particle leaves the simulation box an image rejoins from the other side, as shown in figure 3.1. The system becomes periodic, with a periodicity equal to the dimensions of the box.

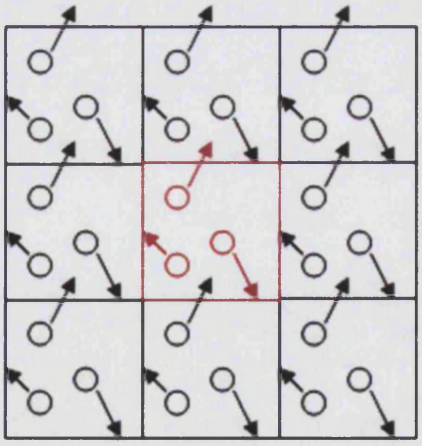

Figure 3.1: Schematic representation of periodic boundary conditions where the simulation cell is highlighted in red

The red cell in figure 3.1 indicates the simulation cell whereas the black cells indicate the images. The system no longer has a surface, which is necessary to simulate bulk crystals or in the case of liquids to prevent outer molecules boiling off into space. The work in this thesis is applied to simulating mineral surfaces. Therefore, we have to employ one of two strategies to simulate surfaces when using periodic boundary conditions.

1) Assume 3-dimensional periodicity and have a slab that repeats infinitely in two dimensions, while in the third direction the slab and its images are separated by a vacuum gap. The advantage of assuming 3-D periodicity is that the 3-D Ewald method can be exploited to model the electrostatic interactions but extra care must be taken to avoid slabs interacting with their images. In general, by having both surfaces in the slab identical there will be no dipole perpendicular to the surface.
2) Use 2-dimensional periodic boundary conditions. So the cell is periodic in only two directions, as the other one is used to create the surface. This uses the Parry summation which was described in the previous chapter.

3.2 Energy Minimisation

Interatomic potentials are used to describe the interaction energy of the system, however, if the system is in equilibrium the interaction energy should be at its minimum. The system should be at mechanical equilibrium with no net forces. There are two approaches to reach this global minimum and remove the net forces in EM. The first method is to perform a constant volume minimisation, where the cell dimensions are kept fixed but the ions are allowed to move. The second method is constant pressure minimisation, where both cell dimensions and ions are allowed to relax. The ions are at their minimised position when all forces are equal to zero:

$$\frac{\partial U}{\partial r} = 0 \tag{3.1}$$

Where ∂U is the change in the forces and ∂r is the change in position of the ion. In this study constant volume energy minimisation was performed using two approaches, both of which are iterative techniques, conjugate-gradient and Newton-Raphson methods.

3.2.1 Conjugate-Gradients

The conjugate-gradient technique [171] is an extension of the steepest descent method in which successive steps use previous information on the forces to direct the minimisation. In the steepest descent method, the new positions are calculated by:

$$r^{n+1} = r_n - \alpha_n S_n \tag{3.2}$$

Where r_n is the position at iteration n, α_n is a numerical constant chosen for each iteration to optimise the efficiency of the minimisation, and S_n is the displacement vector defined as:

$$S_n = -g_n \tag{3.3}$$

With

$$g_n = \frac{\partial U}{\partial r_n} \tag{3.4}$$

In general, the steepest descent method is not efficient. Each new displacement vector, or minimisation direction, is orthogonal to the last, but not to any previous

ones. Therefore, it is desirable to choose a set of directions where minimisation along any one will not interfere with the others. In the conjugate-gradient method, the displacement vector is obtained from information on the previous value of the gradients:

$$S_n = -g_n + \gamma_n S_{n-1} \tag{3.5}$$

Where:

$$\gamma_n = \frac{g_n^T \cdot g_n}{g_{n-1}^T \cdot g_{n-1}} \tag{3.6}$$

And $S_1 = g_1$. The superscript T refers to the transpose of the vector. Complete minimisation occurs when S_n is zero or close enough to zero to satisfy an accuracy criterion. The conjugate-gradient technique has the advantage that each iteration is very fast due to the fact that only the first derivative of the energy with respect to the positions is required. However, since α is initially approximated and the potential energy surface is not exactly harmonic, a large number of iterations have to be performed using the conjugate-gradient technique. A more efficient algorithm in terms of the number of iterations is employed by the Newton-Raphson technique.

3.2.2 Newton-Raphson

The Newton-Raphson method [172] provides a reliable estimate of α by including a second derivative of energy with respect to displacement:

$$\frac{\partial U}{\partial r} = g = kr \tag{3.7}$$

Then:

$$\frac{\partial^2 U}{\partial r^2} = k \tag{3.8}$$

As k is a matrix we will represent as W_{ij}:

$$W_{ij}(r) = \frac{\partial^2 U}{\partial r_{ij}^2} \tag{3.9}$$

Where W_{ij} is the bond strength between atom i and j:

$$force = g_i^n(r) = W_{ij}\left(r_i^{n+1} - r_i^n\right) \tag{3.10}$$

Where r_i^n is the position of atom i at iteration n:

$$r_i^{n+i} = r_i^n - \left(W_{ij}^{-1}\right)^n g_i^n \tag{3.11}$$

The Newton-Raphson method thus requires fewer iterations, however, the calculation and the inversion of W_{ij} is very expensive in terms of CPU time and memory. So a combination of the two methods can be used in-order to get reliable results in the most efficient time.

The constant pressure method employs Hooke's law by calculating the total stress or pressure on the unit cell and the second derivative of energy with respect to stress, i.e. the elastic constant to find the strain energy on the cell. The unit cell is adjusted by the strain iteratively until equilibrium is achieved. This is ideally suited to energy minimisation of bulk materials. When considering the energy of isolated particles and surfaces we use only the constant volume minimisation. All energy minimisation calculations are performed using the METADISE (Minimum Energy

Techniques Applied to the Dislocation, Interfaces and Surface Energies) code [173]. This code includes the developments from the MIDAS code, developed by Tasker [174], CHAOS [175], METAPOCS [176], and PARAPOCS [177].

As previously mentioned energy minimisation neglects the influence of temperature on the structure and reactivity of minerals. Therefore molecular dynamics was used throughout this work to study the systems of interest at a certain temperature.

3.3 Molecular Dynamics

Molecular dynamics is the numerical solution of classical equations of motion for atoms and molecules to obtain the time evolution of the system. The method includes kinetic energy explicitly by assigning all particles position and velocity. This allows atoms to "jump" over energy barriers and find global minimum. However due to the very short "real time" accessible to molecular dynamics simulations, this only applies to small energy barriers, i.e., of the order of a few k_BT. All molecular dynamics simulations in this work were performed with the computer code DL_POLY 2.0 [163] developed by W. Smith and T.R. Forester at the Daresbury Laboratory, UK. The increasing power of computers and the developments by eScience enable more complex systems to be simulated for longer times. A new development of the DL_POLY code has enabled systems of the order of millions of ions to be simulated more efficiently. This code DL_POLY 3.0 [178, 179] was developed by I.T. Todorov and W. Smith and has introduced the Domain Decomposition (DD) methodology in order to improve efficiency.

Molecular dynamics consists of solving Newton's laws of motion over a finite period for the ensemble:

$$a = \frac{F}{m} \tag{3.12}$$

Where a is the acceleration, F is the force and m is the mass. The forces acting on the ions are calculated using the same method as for energy minimisation. If the accelerations are known then you can evaluate the new velocities and new positions of the ions for an infinitely small time step.

$$v_i(t+\Delta t) = v_i(t) + a_i(t)\Delta t \tag{3.13}$$

$$r_i(t+\Delta t) = r_i(t) + a_i \frac{\Delta t^2}{2} \tag{3.14}$$

Where v_i is the new velocity and r_i is the new position at time step t. These Newton equations can be applied strictly for infinitesimal time steps. In practise, computer codes use integration algorithms to combat the errors that can occur because Δt is not infinitesimally small.

3.3.1 Integration Algorithms

Integration algorithms are used to update the positions and velocities of the ions at a finite time step. If the classical trajectory is continuous then an estimate of the positions, velocities and accelerations can be obtained by a Taylor expansion about time.

$$r(t+\partial t) = r(t) + v(t)\partial t + \frac{1}{2}a(t)\partial t^2 + \frac{1}{6}b(t)\partial t^3 + \ldots$$
$$v(t+\partial t) = v(t) + a(t)\partial t + \frac{1}{2}b(t)\partial t^2 + \ldots$$
$$a(t+\partial t) = a(t) + b(t)\partial t + \ldots$$
$$b(t+\partial t) = b(t) + \ldots \quad (3.15)$$

Where x is the position of the ion, v is the velocity, a is the acceleration and b is the third time derivatives of r. By using equation 3.15, one can calculate the position of a particle, $r(t)$, before and after the time step, δt.

$$r(t+\partial t) = r(t) + v(t)\partial t + \frac{1}{2}a(t)\partial t^2 + \frac{1}{6}b(t)\partial t^3 + \vartheta(\partial t^4) \quad (3.16)$$

$$r(t-\partial t) = r(t) - v(t)\partial t + \frac{1}{2}a(t)\partial t^2 - \frac{1}{6}b(t)\partial t^3 + \vartheta(\partial t^4) \quad (3.17)$$

Where ϑ is the order of accuracy. Adding 3.16 and 3.17

$$r(t+\delta t) + r(t-\delta t) = 2x(t) + a(t)\delta t^2 + \vartheta(\delta t^4) \quad (3.18)$$

Or

$$r(t+\delta t) = 2r(t) - r(t-\delta t) + \frac{\delta t^2}{m}f(t) + \vartheta(\delta t^4) \quad (3.19)$$

This is the basis of the Verlet algorithm [180] which is one of the most widely used method of integrating the equations of motion. The method is based on the ion position at time step t and the previous position at time step, $(t-\delta t)$, as well as the current force. From equation 3.19 one can see that the velocities do not appear. The velocities are not required to compute the trajectories, but are useful for estimating

the kinetic energy. To calculate the velocities in the system one can subtract equation 3.17 from 3.16.

$$v(t) = \frac{r(t+\delta t) - r(t-\delta t)}{2\delta t} + \vartheta(\delta t^2) \tag{3.20}$$

This implies that the velocities can only be calculated once $r(t+\delta t)$ is known and that they are subject to errors of the order δt^2. More accurate estimates of $v(t)$ can be made but only if more variables are stored. Another observation of the Verlet algorithm is that it is properly centred; meaning that $r(t-\delta t)$ and $r(t+\delta t)$ play symmetrical roles in equation 3.19. This makes it time-reversible. A major disadvantage of this algorithm is that in equation 3.19 a small term $(\vartheta(\delta t^2))$ is added to a difference of large terms $(\vartheta(\delta t))$. This adds some numerical imprecision.

A modification to the Verlet algorithm and the algorithm used in the DL_POLY 2.0 code is called the Verlet leapfrog algorithm [181]. The term leapfrog will become apparent once we have derived the algorithm.

$$v\left(t + \frac{1}{2}\delta t\right) = \frac{r(t+\delta t) - r(t)}{\delta t} \tag{3.21}$$

and

$$v\left(t - \frac{1}{2}\delta t\right) = \frac{r(t) - r(t-\delta t)}{\delta t} \tag{3.22}$$

Hence, equation 3.19 can be written as

$$\frac{r(t+\delta t) - r(t)}{\delta t} = \frac{r(t) - r(t-\delta t)}{\delta t} + \frac{\delta t}{m} f(t) + \vartheta(\delta t^3) \tag{3.23}$$

Then from equations 3.21 and 3.22

$$v\left(t+\frac{1}{2}\delta t\right)=v\left(t-\frac{1}{2}\delta t\right)+\frac{\delta t}{m}f(t)+\vartheta\left(\delta t^{3}\right) \tag{3.24}$$

and

$$r(t+\delta t)=r(t)+v\left(t+\frac{1}{2}\delta t\right)\delta t+\vartheta\left(\delta t^{4}\right) \tag{3.25}$$

The algorithm defines velocities that are half a time step behind, or in front of, the current time step. When the forces of the current time step, *f(t)*, have been calculated they are used in the first equation to advance the velocities from the half step behind to the half step ahead. Therefore, the velocities can be seen as to "leapfrog" over the current time step. When the atom velocities have been advanced, the position can be updated using equation 3.25. The main advantage is that numerical precision is improved.

The leapfrog method does not however handle velocities in a completely satisfactory matter [182]. A "velocity Verlet" algorithm has been proposed by Swope *et al.* [183] and can be implemented in DL_POLY 3.0. This algorithm does store positions, velocities, and accelerations all at time *t*, which minimises rounding errors. The advantage of this form is that it requires less computer memory because only one set of positions, forces and velocities need to be carried at any one time.

3.3.2 Time Step and Equilibration

The choice of time step, δt, in these equations is very important because if δt is too large atoms or shells will move an unphysical distance from which the system could not recover. If it is too small the simulation will require too many interations for the ions to move a significant distance or for a useful real time to elapse. In this work I have used a time step of $0.1\text{x}10^{-16}$s (0.1 femto seconds) or $0.2\text{x}10^{-16}$s (0.2 femto

seconds). The first part of the molecular dynamics simulations is to allow the system to come to equilibrium at a given temperature and pressure before the collection of data. This allows the ensemble to attain a thermalised distribution of velocities after a fixed number of steps. Typically, this requires a few tens of thousands of steps. Data are then collected without scaling of the velocities for as long as possible in order to make sure converged averages are obtained for the properties of the system we are interested in.

3.3.3 Ensembles

The conditions of molecular dynamics simulations are called ensembles. There are four different types of ensembles employed in this thesis.

- The microcanonical ensemble (NVE), where the number of particles, the volume and the total energy of the system are held constant.

$$\mathrm{H}_{NVE} = U + K.E \tag{3.26}$$

Where U is the potential energy and $K.E$ is the kinetic energy.

- The canonical ensemble (NVT) is where the number of particles, the volume and the temperature of the system are constant. A Nosé-Hoover thermostat [184] is used as a heat bath to keep the temperature constant. The Nosé-Hoover algorithm modifies Newton's equations of motion by including a friction coefficient, χ:

$$\frac{\partial v(t)}{\partial t} = \frac{f(t)}{m} - \chi(t)v(t) \tag{3.27}$$

This friction coefficient is controlled by the first order differential equation:

$$\frac{\partial \chi(t)}{\partial t} = \frac{N_f k_B}{Q}\left(T(t) - T_{ext}\right) \tag{3.28}$$

$$Q = N_f k_B T_{ext} \tau_T^2 \tag{3.29}$$

Where Q is the effective mass of the thermostat, τ_T is the specified time constant, N_f is the number of degrees of freedom in the system, $T(t)$ is the instantaneous temperature and T_{ext} is the temperature of the heat bath. Usually the specified time constant is in the range of 0.5 to 1ps. The Verlet leapfrog algorithm is modified using equations 3.27 to 3.28; however, as $v(t)$ is required to calculate T and therefore itself, several iterations are required to obtain self consistency. In the DL_POLY code, the number of iterations is set to three and the first prediction of $v(t)$ and T are obtained by means of a standard Verlet leapfrog algorithm. The conserved quantity, derived from the extended Hamiltonian for the system, is

$$\mathrm{H}_{NVT} = U + KE + \frac{1}{2}Q\chi(t)^2 + \frac{Q}{\tau_T^2}\int_0^t \chi(s)\partial s \tag{3.30}$$

- The isobaric-isothermal ensemble (NPT) is where the number of particles, the pressure and the temperature is held constant. The conditions can be isotropic, which means that only the cell dimensions vary, or anisotropic when both the cell dimensions and shape can change. In this work, the Melchionna modification of the Hoover algorithm was used [185], which involves a Nosé-Hoover thermostat and barostat that follows a similar algorithm as before. Like in the previous ensemble several iterations are required to obtain self consistency and in DL_POLY it uses 4 iterations with the standard Verlet leapfrog predictions for the estimates of the

instantaneous temperature and pressure. In this work only isotropic conditions are used.

There are a number of other ensembles. The most widely used of these is the grand canonical ensemble (μVT) is where the chemical potential of the system, the volume and the pressure are constant.

3.3.4 Properties from molecular dynamics

Calculated molecular dynamic properties can be separated into two classes: static system properties and dynamical system properties.

The static system properties can be further separated into thermodynamic and structural properties.

The thermodynamic properties include:

- Kinetic Energy: $\langle K.E.\rangle = \left\langle \frac{1}{2}\sum_{i}^{N} m_i v_i^2 \right\rangle$ (3.31)
- Temperature: $T = \frac{2}{3Nk_B}\langle K.E.\rangle$ (3.32)
- Configuration Energy: $U_c = \left\langle \sum_{i}\sum_{j>i}^{N} (x_{ij}) \right\rangle$ (3.33)

The structural properties include:

- Radial Distribution Function (RDF): $g(r) = \frac{V}{N^2}\left\langle \sum_{i}\sum_{j\neq i}^{N} \delta(r - r_{ij}) \right\rangle$ (3.34)

Where r is the distance along the x, y and z-axis. The radial distribution function is an example of a pair correlation function, which describes how, on average the atoms in a system are radially packed around each other. This proves to be a particularly effective way of describing the average structure of disordered molecules such as liquids.

Dynamic system properties are mainly correlation functions and include:

- The Mean Squared Displacement (MSD) (Einstein's relation):

$$2Dt = \frac{1}{3}\left\langle \left| r_i(t) - r_i(0) \right|^2 \right\rangle \tag{3.35}$$

MSD describes how far an atom has moved. If $\left\langle \left| r_i(t) - r_i(0) \right|^2 \right\rangle$ is plotted as a function of time, the gradient of the curve obtained is equal to 6 times the self diffusion coefficient of particle i. The motion of an individual molecule in a dense fluid does not follow a simple path. It follows a random path where each step is followed by another in a totally random direction. This is described as Brownian motion, which shows that the mean square of the distance travelled by a particle following a random walk is proportional to the time elapsed.

$$\left\langle r^2 \right\rangle = 6Dt + B \tag{3.36}$$

Where $\left\langle r^2 \right\rangle$ the mean square distance and t is time. D is the diffusion coefficient and B the Debye-Waller constant and refers to the size of the normal ellipsoid. In a molecular system, a molecule can move in three directions. By the definition of Brownian motion this can be random, forward or backward. Instead of adding the distance of each step, the square of the distance is added, and therefore always adding a positive quantity. So MSD is the average square distance which through its relation to diffusion is a measurable quantity but which also relates to the underlying motion of the molecules.

- The velocity correlation function (VACF) (Green-Kubo relation) is another method to obtain diffusion coefficients:

$$D = \frac{1}{3}\int_0^\infty \langle v_i(t).v_i(0)\rangle dt \tag{3.37}$$

Green-Kubo relations have been derived for many transport coefficients such as the shear viscosity and the thermal conductivity [186]. In a solid, the Fourier transform of the normalized VACF gives the frequency distribution of phonon states, i.e., the density of states [187].

3.3.5 Free Energy Calculations

The previous section discussed the main properties that can be obtained directly from a molecular dynamics simulation. However, properties such as entropy and free energy cannot be calculated directly. The Second Law of thermodynamics states that for a "spontaneous" reaction the associated entropy change ΔS should be positive. The ability to track the total entropy can be challenging as it requires the determination of the entropy change for both the system and the surroundings. As entropic effects are very useful in chemistry a more convenient concept is that of the Gibbs free energy G defined by the Gibbs equation:

$$\Delta G = \Delta H - T\Delta S \tag{3.38}$$

Where H is the enthalpy and T the temperature. For a spontaneous reaction ΔG is negative and where the system is at equilibrium ΔG is zero. For a system in which there are a fixed number of particles, constant volume and temperature (canonical ensemble), the corresponding function is the Helmoltz free energy ΔA defined as:

$$\Delta A = \Delta U - T\Delta S \tag{3.39}$$

Where ΔU is the internal energy of the system. Calculating free energy changes can be achieved by calculating the energy of a system in different configurations and building up a partition function. Free energy perturbation is a technique used to describe the energy difference between two systems or the free energy change associated with a chemical reaction. The free energy of a particular state A is related to the partition function Q:

$$A = -k_B T \ln Q \tag{3.40}$$

So if Q_1 and Q_2 are partition functions for states 1 and 2 then the difference in the free energies between the two states is given by

$$\Delta A = A_2 - A_1 = -k_b T \ln\left(\frac{Q_2}{Q_1}\right) \tag{3.41}$$

The term perturbation has been employed to indicate that states 1 and 2 differ by a small "perturbation". For successful application of the perturbation approach, the configurations generated for state 1 must be also representative of state 2. This means that there needs to be an "overlap" between the two states and a free energy change should ideally be no greater than $2k_BT$. Since MD simulations can contain many thousands of atoms it isn't possible to search enough of configuration space to use free energy perturbation. We would like to define the important degrees of freedom and average out the unimportant degrees of freedom in such a way that the thermodynamic properties of the system are maintained.

One approach to obtain thermal quantities from molecular dynamics simulations is to use the thermodynamic integration method. This method is based on the fact that the derivation of thermal quantities often yields mechanical properties. As an example, let us assume that we have two states A and B, of which we know the free

energy of state A but not state B at constant volume and temperature. The two states are linked by a reversible pathway, so therefore, by integration of the energy along this pathway can lead to the free energy of a state B. This path does not have to be a physical path and any parameter can be used as a thermodynamic variable, ϕ, providing that the potential energy, U, depends linearly on ϕ. So that for $\phi = 0$, U corresponds to the potential energy of the reference system. The derivative of the Helmholtz free energy $A(\phi)$ with respect to ϕ can be written as:

$$\left(\frac{\delta A(\phi)}{\delta \phi}\right)_{NVT} = \left\langle \frac{\delta U(\phi)}{\delta \phi} \right\rangle_{\phi} \tag{3.42}$$

Where $\left\langle \frac{\delta U(\phi)}{\delta \phi} \right\rangle_{\phi}$ is the ensemble average derivative of the potential energy in the system with respect to the thermodynamic variable. Therefore integration of Equation 3.42 yields the free energy difference between states A and B:

$$A(B) - A(A) = \int_{\phi=0}^{\phi=1} \left\langle \frac{\delta U(\phi)}{\delta \phi} \right\rangle_{\phi} d\phi \tag{3.43}$$

The free energy difference can be obtained from molecular dynamics simulations as it only depends on the ensemble average of the mechanical quantities. In chapter 5 we use this approach to calculate the free energy profiles of the dissolution of ions from carbonate surfaces. In this case, the thermodynamic variable is the distance between the surface and the dissolving ion.

Another approach is to define super atoms by joining together several atoms into one interaction unit. The interaction between the atoms on the super atom is defined by Potential of Mean Force (PMF). The PMF is the free energy of a system as a function of a reaction coordinate. Examples of reaction coordinates include bond distance [188] or a path in 3-dimensional space such as the path through a pore in a

membrane [189] or a path through a zeolite catalyst [190]. The reaction coordinate R is dependent on the coordinates of the atoms in the system:

$$R(r) = R(r_1, r_2, ..., r_N) \tag{3.44}$$

A system confined in physical terms to such a reaction coordinate *R(r)* is also restricted to a hyperspace *R(r)* in phase space, and would be characterised by the partition function *Q(R)* and a free energy of *A(R)*. The probability of a given configuration of a system being on the hyperspace *R(r)* is:

$$\pi(p^N, r^N; R') = \frac{\exp[-\beta H(p^N, r^N)]\delta(R' - R(r^N))}{\int dp^N dr^N \exp[-\beta H(p^N, r^N)]} \tag{3.45}$$

Where the system is characterised by the Hamiltonian *H(r,p)*. *H(r,p)* is the sum of the kinetic and potential energy at position r and momenta p. Integration of equation 3.45 over phase space yields the probability of the system being at the specified reaction coordinate:

$$\begin{aligned} P(R') &= \int dp^N dr^N \pi(p^N, r^N; R') \\ &= \frac{\int dp^N dr^N \exp[-\beta H(p^N, r^N)]\delta(R' - R(r^N))}{\int dp^N dr^N \exp[-\beta H(p^N, r^N)]} \\ &= \frac{Q(R')}{Q} \end{aligned} \tag{3.46}$$

Which in terms of free energy $A(R')$ reduces to:

$$\begin{aligned} A(R) &= -k_\beta T \ln P(R') - k_\beta T \ln Q \\ &= -k_\beta T \ln P(R') + \text{constant} \end{aligned} \tag{3.47}$$

The determination of $P(R')$depends on the application but there are three general approaches: Boltzmann sampling, Umbrella sampling and use of constraints. In this work we use constraints to calculate the probability of the system being at a specified reaction coordinate. The system in question is constrained at a particular value of reaction coordinate R_c:

$$\sigma(r;R_c) = R(r) - R_c \tag{3.48}$$

The constraints allow the Cartesian coordinates of the atoms to become dependent on each other and therefore it is necessary to transform to a set of generalised coordinates *(q,p)*, equating one of the coordinates to the reaction coordinate *R*. The free energy, $A(R')$, associated with a particular reaction coordinate R_c is obtained by the integration of the force to keep it at that reaction coordinate:

$$A(R_c) = \int_{\infty}^{R_c} A(R(r))dR \tag{3.49}$$

$$A(R_c) = \frac{\langle(\partial r/\partial R)[-\partial U/\partial r + k_\beta T\partial \ln(|J|)/\partial r]\delta(R' - R(r^N))\rangle}{\langle\delta(R' - R(r^N))\rangle} \tag{3.50}$$

Where $|J| = |\partial r/\partial q|$. If *R(r)* is linearly dependent on the Cartesian coordinates the Jacobian *J* is zero. This term may be neglected when the range of *R* is limited and this term is essential constant. In chapter 6 we see how this approach can be used to calculate the free energy change of the aggregation of mineral and carbonate nanoparticles.

3.4 Simulation of Mineral Surfaces and Nanoparticles

As previously mentioned in this chapter an effective method of determining the structure and stability of a surface is by using energy minimisation to determine its lowest energy state. In this work, the computer code METADISE [173] has been used to minimise bulk, surfaces and isolated particles using energy minimisation. METADISE has been applied to calculate surface energies and defect energies that will be described in Chapters 4 and 5 this code is used in the generation of mineral surfaces and isolated particles which shall now be described.

3.4.1 Simulation of Mineral Surfaces

As a way of describing the different types of surfaces, Tasker [191] assigned each surface as one of three types. The assignment built on the work by Bertaut, 1958 [192], in which he showed that when there is a dipole moment in the unit cell perpendicular to the surface, the surface energy diverges with increasing depth. Tasker showed that this divergence to infinity occurs on only certain charged surfaces. Figure 3.2 shows a schematic of the three types of surface described by Tasker. Type 1 surfaces consist of neutral planes with both anions and cations. Type 2 consists of charged planes arranged symmetrically so that there is no dipole moment perpendicular to the unit cell. Neither of these surfaces affects ions in the bulk of the crystal and should have modest surface energies. The type 3 surface is charged and there is a perpendicular dipole moment. Surface energies of these surfaces diverge and produce a polarising electric field in the bulk.

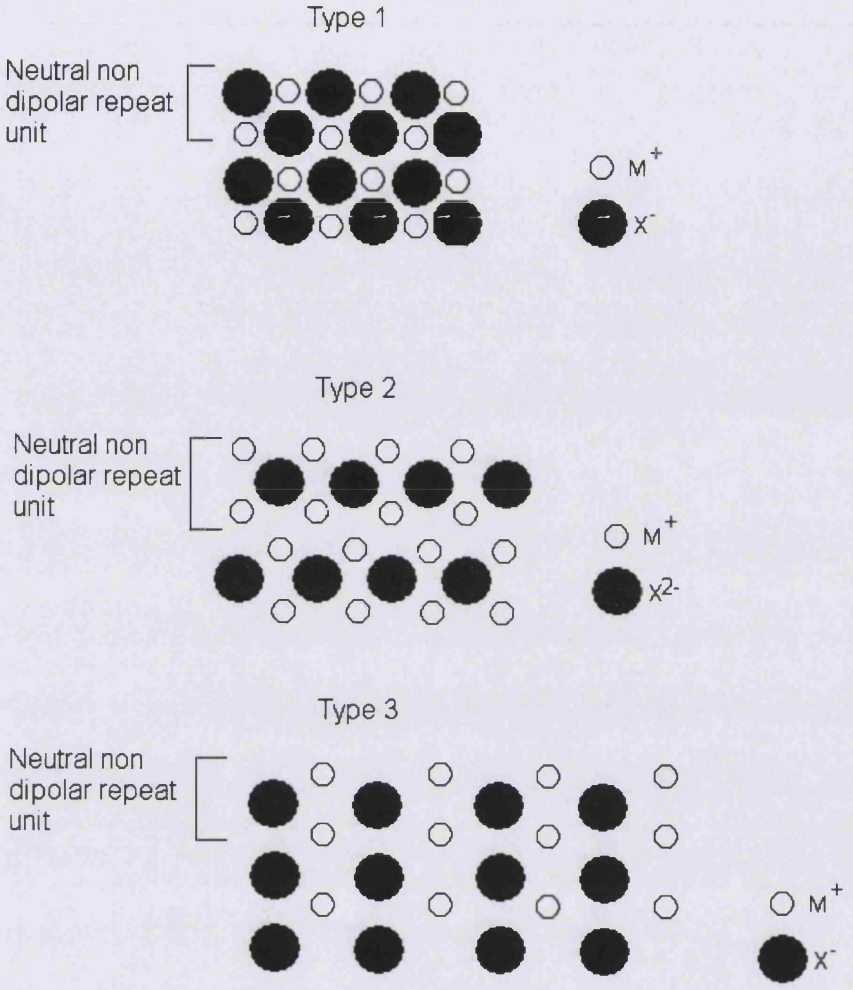

Figure 3.2: The three types of stacking sequences described by Tasker [191]

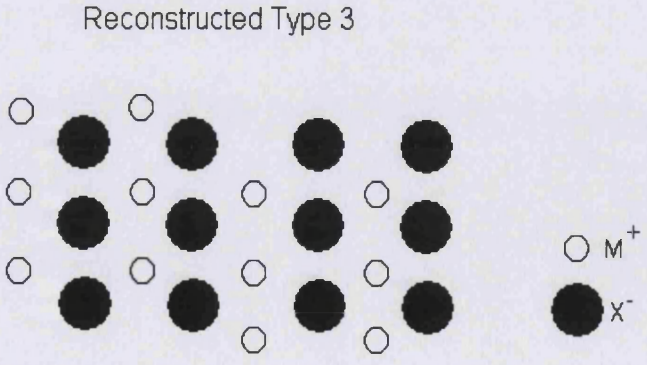

Figure 3.3: Reconstructed Type 3 stacking sequences [193]

Figure 3.3 shows that when a polar surface is cut, it reconstructs the surface into a non polar surface. This neutralising of the dipole can also be achieved by adsorption of foreign atoms, by a redox process, or by faceting a polar surface. The latter is where an unstable surface (often polar) facets so that it is composed of small stable surfaces. Figure 3.4 shows an example of a polar MgO surface faceting to replace a flat (111) surface by pyramids comprising the stable (100) surface. See figure 3.5 for a schematic of this process.

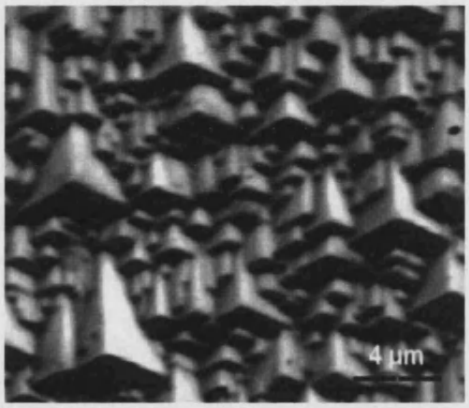

Figure 3.4: Faceting of the polar MgO (111) surface into neutral (100) planes [194]

Figure 3.5: Schematic of how a faceting surface copes with polar surfaces

3.4.2 Surface Energy Calculations

Two-Dimensional Approach

As noted above surface simulations consider the crystal to consist of a series of charged planes parallel to the surface and periodic in two dimensions. The complete crystal is formed by adding many charged planes. The problem is that the explicit simulation of many charged planes is computationally expensive. Thus, the usual convention is to use the two-region method developed by Tasker [195], which is used in the METADISE code. The simulated crystal is made up of two blocks; each of them is separated into two regions periodic in two dimensions. The atoms in the first region are those near the surface and are able to relax mechanically. Whereas those in region II are further away and are held fixed at their bulk equilibrium positions. They represent the rest of the crystal.

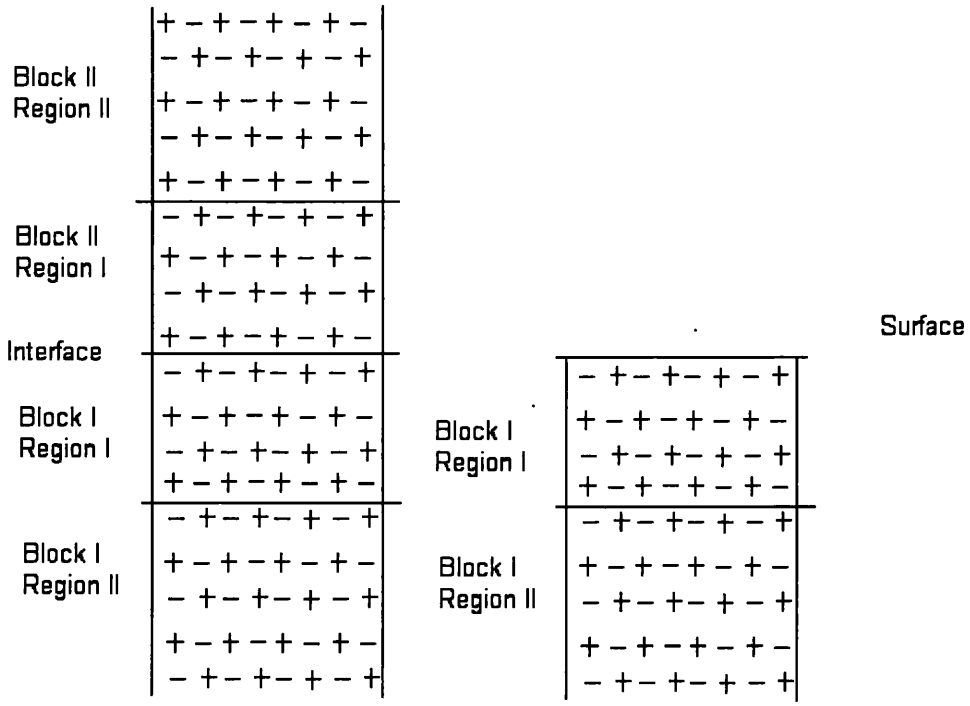

Figure 3.6: Schematic representation of the two region approach used in METADISE

The energy of the blocks is calculated by summing the energies of the interaction between all atoms. The energy of the block for a surface simulation is:

$$U_s = \left(E^S_{I-I} + E^S_{I-II}\right) + \left(E^S_{II-I} + E^S_{II-II}\right) \tag{3.51}$$

Where the first term is the energy of the ions in region I, i.e. E_{I-I} region I ions interacting with region I ions and E_{I-II} region I ions interacting with region II ions. The second term is the energy of ions in region II. A similar interaction scheme can be developed for the bulk.

$$U_b = \left(E^B_{I-I} + E^B_{I-II}\right) + \left(E^B_{II-I} + E^B_{II-II}\right) \tag{3.52}$$

The surface energy, γ, is given by:

$$\gamma = \frac{U_s - U_b}{A} \tag{3.53}$$

If the surface area, A, and the position in region II are constant:

$$E^S_{II-II} = E^B_{II-II} \tag{3.54}$$

the code can save some considerable CPU time by not calculating the energy of the interaction of the ions in region II. The Parry technique is employed to calculate the electrostatic forces while parameterised analytical functions describe the short-range interactions, as discussed in the previous chapter.

Three-Dimensional Approach

An advantage of the three-dimensional Ewald method compared to the two-dimensional Parry method is that it is extremely fast and efficient. Therefore, when carrying out molecular dynamics calculations on surfaces using DL_POLY [163] a special application of periodic three-dimensional boundary conditions is used. The system is first relaxed to the bulk structure and oriented so that two of the three lattice vectors are parallel to the surface. The third vector, which is now perpendicular to the surface, is then increased in size, thus introducing a gap into the crystal and producing repeating crystal slabs. The chosen surfaces are therefore on opposite sides of this crystal slab. This void must be large enough that there are no interactions between atoms on opposite surfaces. The crystal slab must also be thick enough so that the two surfaces on opposite sides do not interact.

This approach is used because the summation of the Coulombic energy for a three-dimensional simulation cell is very efficient. Using the DL_POLY code only two ensembles are available when simulating just a crystal slab in vacuum; the microcanonical (NVE) and canonical (NVT) ensembles. This is because if the volume was not kept fixed the slabs would reform the bulk structure, as this will always be thermodynamically more favourable than surfaces.

3.4.3 Crystal Morphology

Once the surface energies have been calculated METADISE can use this data to construct a 3-dimensional nanoparticle. It does this by calculating the equilibrium morphology by using a Wulff construction [196]. This approach takes the theory of Gibbs to generate the lowest surface energy. The surface energy is different for different facets. For a crystal consisting of a given number of atoms, the equilibrium shape is the shape which minimizes the surface energy. In a 2-dimension Wulff construction, for a polar coordinate system, a vector is drawn parallel to the normal

of the surface, and with its length proportional to the energy of the surface. At the endpoint of the vector a tangent is drawn. If repeated for all surfaces the tangents limit the equilibrium shape. If a particular surface has a high energy, it will not be present in the final construction. The constructions in 3-dimensions are in principle the same except a spherical coordinate system is used and at the end of the vectors a tangent plane is drawn.

3.4.4 Surface Area Calculations

Another important property of a surface simulation or indeed of a nanoparticle is the surface area. METADISE calculates the surface area as the area of the surface unit cell. Thus the surface energy is defined as the energy to cleave that unit cell. However for micro crystals it is not easy to define this area as they are not flat and there are corners, edges and bumps on the surface. So to try and get an accurate surface area and thereby estimate a surface energy, we applied a technique that was first developed by Lee and Richmond in 1971 [197]. This technique was first introduced to address the problem of protein folding, i.e. how much of the protein surface is accessible to the solvent. Lee and Richmond came up with the concept of solvent accessible surfaces as a way of quantifying hydrophobic burial. They modelled a probe sphere to trace the surface of their proteins.

In modelling a probe sphere the surfaces can be traced out depending on the type of surface you want to describe, as shown in figure 3.7.

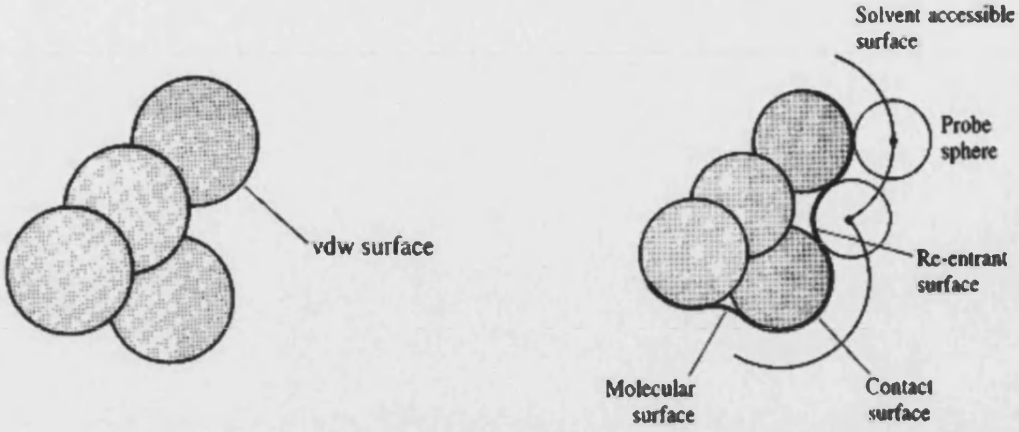

Figure 3.7: Diagram representing the different ways of determining the surface area [197]

There are five different ways of describing the types of surface area that can be attained:

1) Van der Waals surface: constructed from the overlapping van der Waals spheres of the atom.
2) Molecular surface: traced out by the inward-facing part of the probe sphere as it rolls on the van der Waals surface of the molecule.
3) Contact surface: consists of the regions where the probe is in contact with the van der Waals surface.
4) Re-entrant surface: regions occur where there are crevices too narrow for the probe molecule to penetrate.
5) The solvent accessible surface: the surface traced by the centre of the probe molecule.

We employed the molecular surface approach to trace out the surface of nanoparticles. The probe sphere that we use is 2.2 Å in diameter, which is approximately the diameter of a sphere of a water molecule.

In this chapter we have discussed the different theoretical methods used in this thesis. The next chapters will describe how these methods have been used in order to describe the structure and stability of mineral surfaces and mineral nanoparticles under different conditions.

Chapter 4

The Calcite-Water Interface

Calcite is one of the most abundant minerals in the earth's surface. It has a major role in many biological [198] and geochemical [199] processes as well as being used as a catalyst for chemical reactions [200, 201]. A great deal of processes is governed at the mineral-water interface, including dissolution and growth. The central aim of this chapter is to investigate the structure of water above different calcite surfaces and as water is a liquid, we need to employ a dynamical technique, namely molecular dynamics.

This chapter begins by describing the simulated structure of seven different calcite surfaces in vacuum. It is well known that the most stable calcite surface is the flat $\{10\bar{1}4\}$ surface [5]. However, not all surfaces are flat, indeed, the flat $\{10\bar{1}4\}$ surface is known to grow and dissolve at steps and kinks, thus even this surface is

not completely flat from an experimental view point [19, 69]. The two most abundant steps on the $\{10\bar{1}4\}$ surface are the acute and obtuse steps. Therefore, the structures and stability of vicinal surfaces containing the major steps and kinks are investigated. The different surfaces are then placed in contact with water to gain some insight into the structure of the interface when water is above these surfaces. However, firstly the calcite crystal structure is described and then a full description of the stability of the different calcite surfaces using the techniques described in chapter 3.

4.1 Calcite Crystal Structure

Calcite has a rhombohedral crystal structure with space group $R\bar{3}c$. The experimental unit cell parameters of calcite have been derived by x-ray diffraction methods [202] and the atomic coordinates from this are shown in table 4.1. The hexagonal unit cell parameters are a=b=4.9896Å and c=17.0610Å with $\alpha=\beta=90^{\circ}$ and $\gamma=120^{\circ}$. All simulations presented in this chapter use the Pavese potential of 1996 [147], which predicts a=b=4.797Å and c=17.482Å. The structural properties of bulk calcite, such as elastic constants and bulk modulus, compares well with experimental data [203, 204]. This potential has been shown to give reliable results for both static [66] and molecular dynamics simulations [153]. This potential has been used in the past to successfully describe processes on 2-dimensional surfaces [68, 205].

Table 4.1: Atomic coordinates from X-ray diffraction experiments [202]

Atom	Site	Oxidation	x	y	z
Ca	6b	+2	0.00	0.00	0.00
C	6a	+4	0.00	0.00	0.25
O	18e	-2	0.25682	0.00	0.25

4.2 Dry Calcite Surfaces

The flat $\{10\bar{1}4\}$ calcite surface is the most stable [68] and gives rise to its rhombohedral morphology. Two vicinal surfaces are considered; the $\{31\bar{4}8\}$ and $\{3\bar{1}\bar{2}16\}$, where each consist of flat $\{10\bar{1}4\}$ terraces and steps. Both step edges are neutral and the $\{31\bar{4}8\}$ acute step has the carbonate group on the edge of the step overhanging the plane below and the angle formed by the step edge and the lower terrace is 80° on the relaxed surface. The steps of the $\{3\bar{1}\bar{2}16\}$ surface is obtuse, therefore the carbonate groups on the step edge lean back with respect to the plane below. The step angle is 105° on the relaxed surface. Four kinked surfaces are also considered. On a step edge a kink is an offset where the edge jumps one or more atomic units. The four different kinked surfaces can be named by first the orientation of the step and then by the orientation of the partial step at the kink. Therefore the four surfaces are acute-acute (AA), acute-obtuse (AO), obtuse-acute (OA) and obtuse-obtuse (OO). On all kinked surfaces there are two different kinks, one terminated by a calcium ion and one terminated by a carbonate group. Figures 4.1-4.4 show the four different kinked surfaces and the layers of calcium carbonates have been colour coded in order to see the kinks. The light red colour indicates the top layer, a magenta colour is the second layer down and blue is the final layer of the surface. In figures 4.1-4.4 the view is looking down onto the surface.

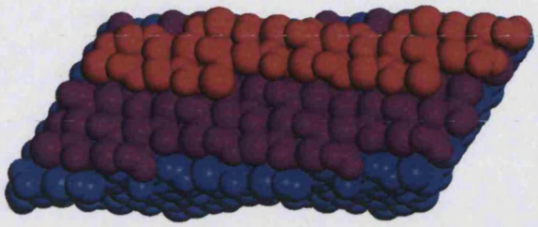

Figure 4.1: Initial configuration of an acute-acute (AA) kinked surface, where the red calcium carbonate layer is the top layer and the blue layer is the bottom layer

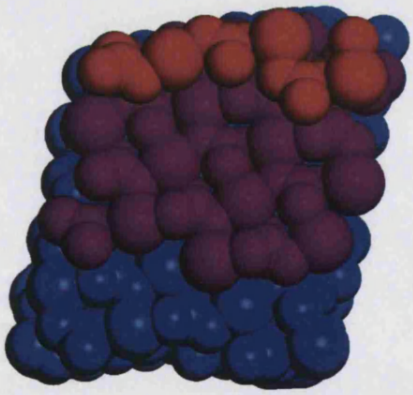

Figure 4.2: Initial configuration of an acute-obtuse (AO) kinked surface, where the red calcium carbonate layer is the top layer and the blue layer is the bottom layer

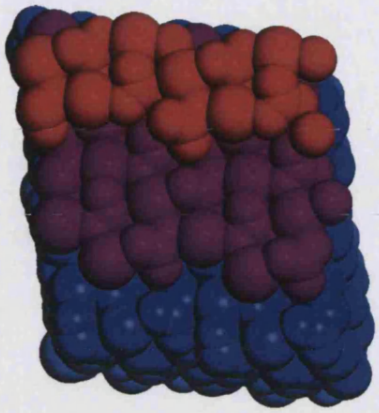

Figure 4.3: Initial configuration of an obtuse-acute (OA) kinked surface, where the red calcium carbonate layer is the top layer and the blue layer is the bottom layer

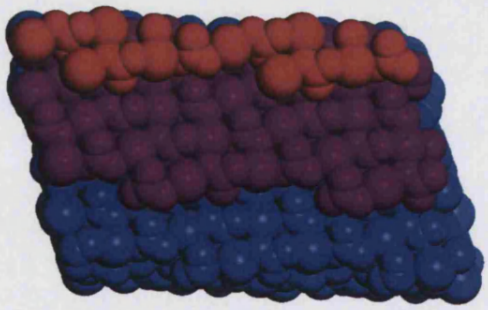

Figure 4.4: Initial configuration of an obtuse-obtuse (OO) kinked surface, where the red calcium carbonate layer is the top layer and the blue layer is the bottom layer

The angles of the acute kinks are 80° and the angles of the obtuse kinks are 110°. The seven surfaces were first energy minimised using the METADISE code [173]. Table 4.2 shows the surface energies of the seven minimised surfaces. The surface energies were calculated in the same way as described in chapter 3 using equations 3.51 to 3.53.

Table 4.2: Minimised surface energies of calcite surfaces using energy minimisation

Surface Orientation	Surface Energy (J/m^2)
Flat $\{10\bar{1}4\}$	0.64
Acute Step $\{31\bar{4}8\}$	0.95
Obtuse Step $\{3\bar{1}\bar{2}16\}$	0.72
Acute-Acute Kink	0.96
Acute-Obtuse Kink	0.97
Obtuse-Acute Kink	0.78
Obtuse-Obtuse Kink	0.77

The kinked surfaces are slightly higher in energy than its stepped counterparts and the surface energies of the two steps compare well with a previous study [66]. The surface energies of the kinks are very similar when on the same steps. As mentioned in chapter 3, energy minimisation neglects the effect of temperature on a simulation, and the system can become trapped in a local minima. It is well known that the carbonate groups are very mobile on a surface [66] and, therefore, we next considered all surfaces using MD simulation. An MD simulation using an NVT ensemble, at a temperature of 300K and ambient pressure was performed. The simulation was run for 400ps with the first 100ps used for equilibration. The thermostat used was a Nose-Hoover [184] with a relaxation time of 0.5ps. A vacuum gap of around 45Å was introduced between repeating slabs. Each slab was between 18 and 25Å thick, which corresponds to a simulation size of between 140 and 240 calcium carbonate units.

Table 4.3 shows the surface energies of the seven surfaces run in the MD simulation. The $\{10\bar{1}4\}$ surface is still the most stable with the two stepped surfaces being the next most stable. The surface energy was calculated as the difference between the MD-averaged potential energy of the calcite surface and the same quantity of bulk calcite divided by the surface area.

Table 4.3: Minimised surface energies of calcite surfaces using molecular dynamics

Surface Orientation	Surface Energy (J/m^2)
Flat $\{10\bar{1}4\}$	0.60
Acute Step $\{31\bar{4}8\}$	0.69
Obtuse Step $\{3\bar{1}\bar{2}16\}$	0.65
Acute-Acute Kink	0.87
Acute-Obtuse Kink	0.80
Obtuse-Acute Kink	1.01
Obtuse-Obtuse Kink	0.67

Using energy minimisation the difference between the two stepped surface energies is $0.23J/m^2$, whereas by allowing the carbonate groups to relax in molecular dynamics the difference reduces to $0.04J/m^2$. The acute step is still slightly less stable than the obtuse step, which is also found in other computational [69] and experimental studies [206]. However, both acute kinks are less stable than their obtuse counterparts by $0.07J/m^2$ on the acute step and $0.34J/m^2$ on the obtuse step. Figures 4.5 and 4.6 shows the final configuration of both acute kinked surfaces after the MD simulation.

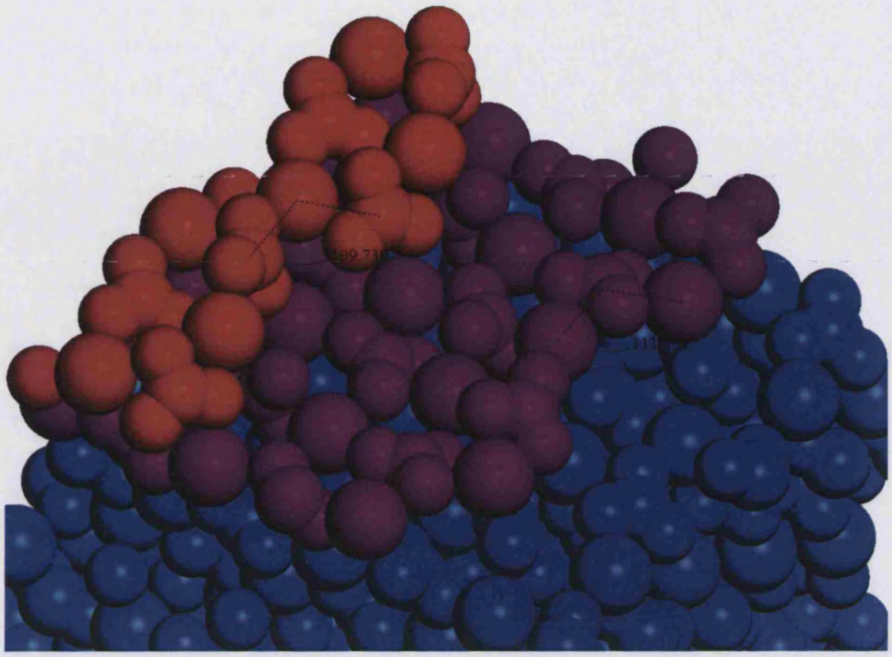

Figure 4.5: Final configuration of an obtuse-acute kinked surface after an MD simulation

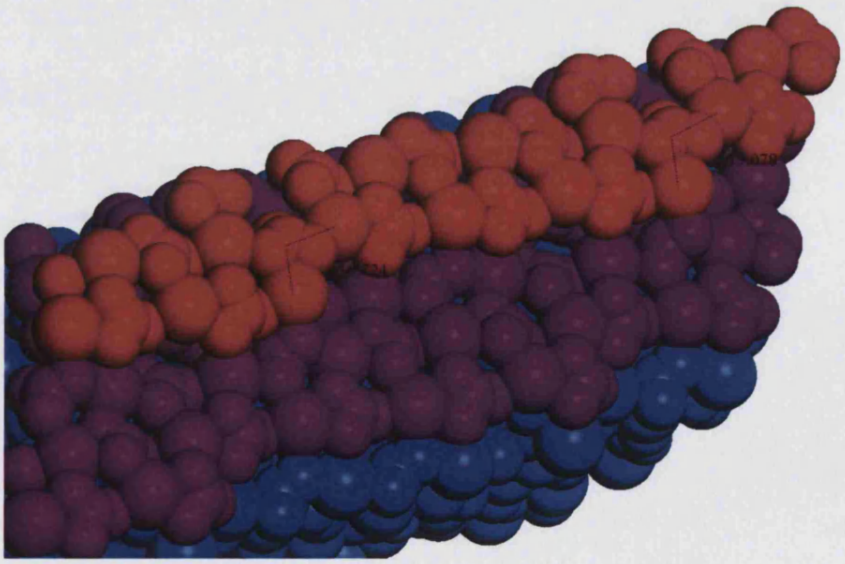

Figure 4.6: Final configuration of an acute-acute kinked surface after an MD simulation

Closer inspection of the acute kinked surfaces after an MD simulation in vacuum reveals that the acute kinks have reconstructed into obtuse kinks with angles ranging from 109° to 117°. The mobility of carbonate ions on the surface has caused the unstable acute kinks to form obtuse kinks. However, experimentally both acute and obtuse kinked surfaces are observed on the surface and provide the active sites for crystal growth [207, 208].

Based on the calculations preformed so far the least stable of the kinked surfaces is the acute-acute and obtuse-acute surfaces and when simulated at room temperature reconstruct to form obtuse kinks. This suggests that these surfaces would dissolve at a faster rate than their obtuse counterparts.

In the next section we shall discuss molecular dynamics simulations performed at room temperature where the seven calcite surfaces are in contact with a slab of water.

4.3 Wet Calcite Surfaces

The seven calcite surfaces were placed in contact with a slab of water of up to 34Å deep on the kinked surfaces and 18Å on the flat and stepped surfaces. An NPT molecular dynamics simulation was performed on each of the simulations using the Nose-Hoover thermostat and Hoover barostat with parameters for the relaxation time of 0.5ps. The simulations were run for 1ns each, with the first 200ps used in the equilibration period. A time step of 0.2fs was used and the simulation was performed at a temperature of 300K and ambient pressure. The water and the calcite-water potentials used are that of Kerisit and Parker [68] given in chapter 2.

4.3.1 Structure of Water above Calcite Surfaces

As discussed in chapter 1, x-ray scattering techniques have shown layering of water above the flat $\{10\bar{1}4\}$ calcite surface [5, 209]. This has also been observed in computational studies above calcite [67] and MgO surfaces [210]. In the case of calcite, the first two high areas of water density correspond to 2.3 ± 0.2Å and 3.5 ± 0.2Å above a flat $\{10\bar{1}4\}$ surface, which is in good agreement with experiments [5]. To illustrate the structure of water above a surface in 3-dimensions the water density was evaluated by splitting the cell into 0.3Å bins. The density was calculated by evaluating the number of times the species of interest passed through a given bin. Therefore a 3-dimensional representation of the water structure above any of the calcite surfaces can be obtained.

Figure 4.7 shows the 3-dimensional projection of the structure of water above a flat $\{10\bar{1}4\}$ calcite surface. The dark blue colour indicates a calcium ion and pale purple through to red indicates the water density. The same colour scheme is used to represent calcium ions and high and low areas of water density in all stepped and kinked surfaces.

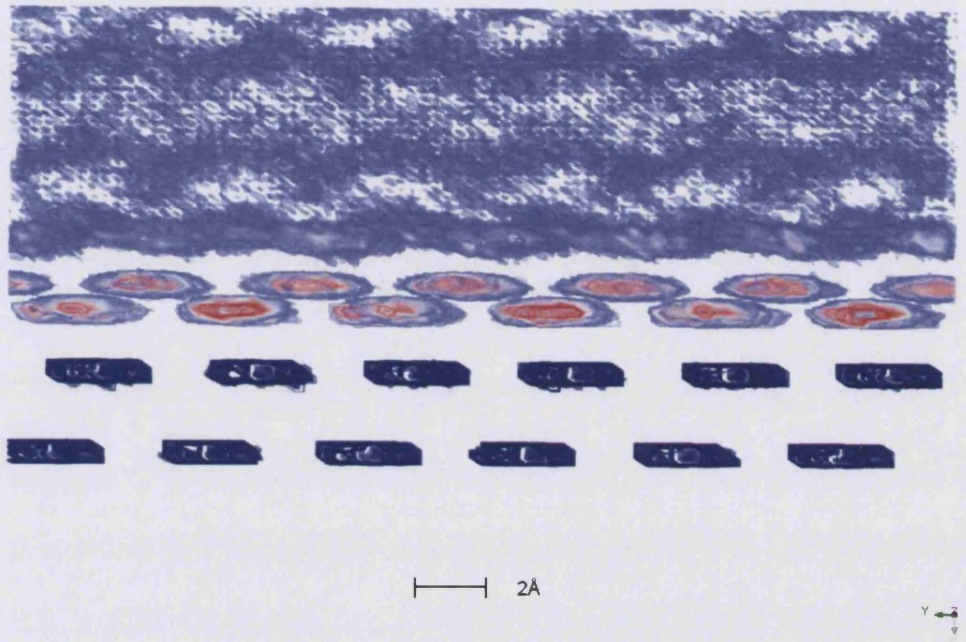

Figure 4.7: 3-dimensional projection of the structure of water above a flat {10$\bar{1}$4} calcite surface. Dark blue indicates a calcium ion, red indicates high water density and pale purple indicates low water density

Figure 4.7 shows the layers of high water density found at around 2.5Å, 3.5Å and 5Å above the surface. The first layer is associated with bonding between the calcium ions on the surface and the oxygen atoms from the water molecule. The second layer at 3.5Å above the surface corresponds to hydrogen bonding between the oxygen of the carbonates on the surface and hydrogen of the water molecules. The heights of the first two layers agree with previous experimental studies [5] and molecular dynamics simulations [67]. It is interesting to note that the distance and layering in the second layer of water is almost a mirror of the position of the carbonates of the second layer of solid below the surface.

The same technique is applied to studying the structure of water above stepped and kinked surfaces. Figures 4.8 and 4.9 show the structure of water above an acute and obtuse stepped calcite surface, respectively.

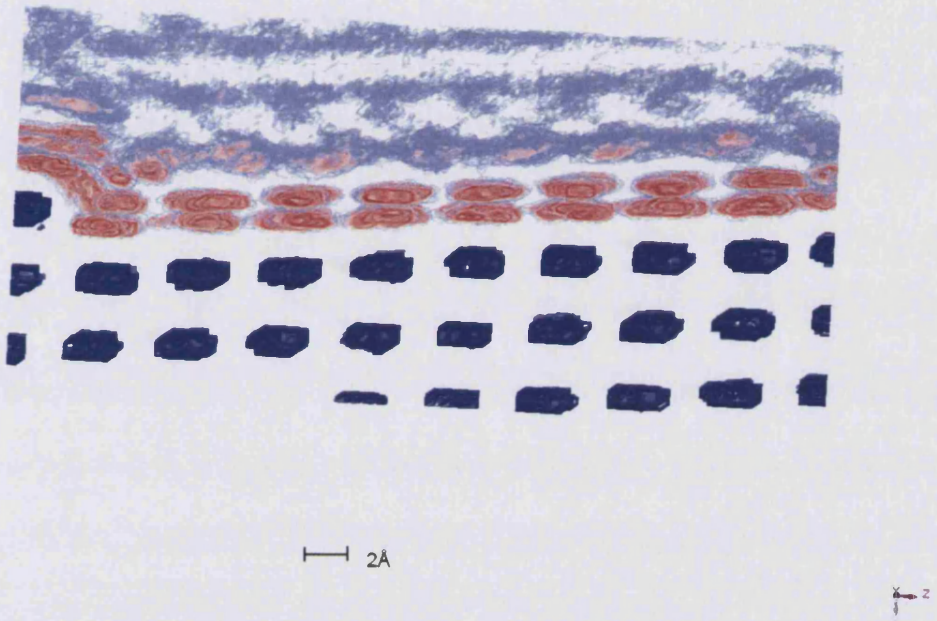

Figure 4.8: 3-dimensional projection of the structure of water above an acute stepped calcite surface. Dark blue indicates a calcium ion, red indicates high water density and pale purple indicates low water density

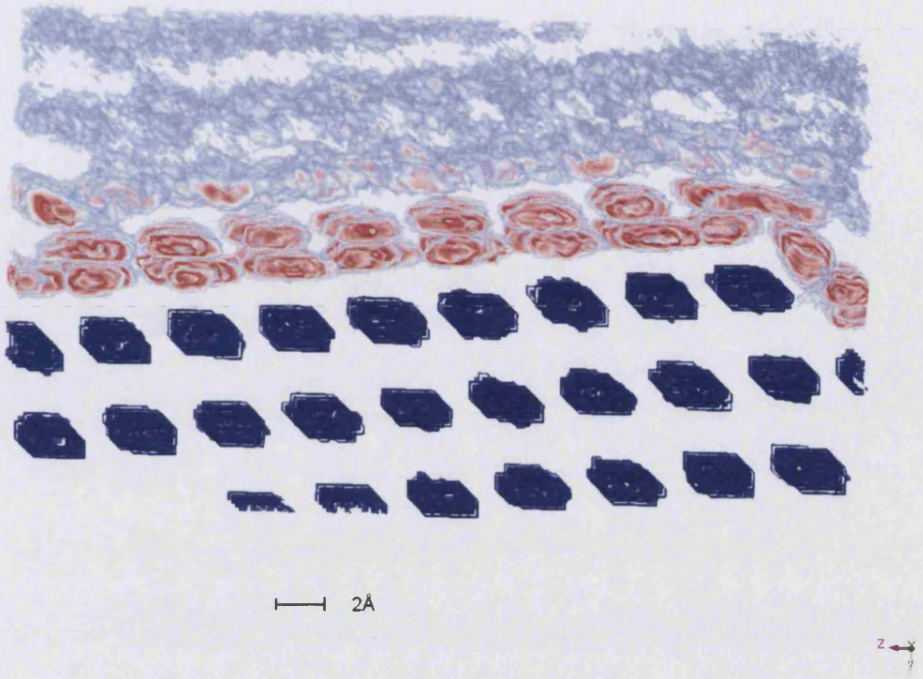

Figure 4.9: 3-dimensional projection of the structure of water above an obtuse stepped calcite surface. Dark blue indicates a calcium ion, red indicates high water density and pale purple indicates low water density

Figures 4.8 and 4.9 show that the presence of the step does not significantly affect the position of the water molecules in the hydration layer. Interestingly, the fact that the layering of water is commensurate with the step height and hence this means that the step does not greatly affect the layering of the outer hydration layers. Of the water molecules coordinated to a calcium ion, only those directly adjacent to the step are disrupted. This is expected, as the stronger the water-surface bonds the more resistant to local distortion there will be. At the acute step, the second water molecule associated with the calcium ion of the step edge is not as strongly bonded as that of the flat surface and appears to delocalise between two possible adsorption sites. The extra room available for water to adsorb at the obtuse step leads to two new adsorption sites appearing along the step edge. For both stepped surfaces, the first and second bulk water layers are disrupted in the vicinity of the step but the effect is more pronounced at the obtuse step. Figures 4.8 and 4.9 suggest that the thickness of the water slab needs to be increased in order to allow the water

structure to fully converge to its bulk value. Therefore, it is clear that the effect of the steps on the structure of water is much more long-range in the direction normal to the surface than it is in the direction normal to the step edge.

A feature of the acute kinked surfaces simulated in vacuum and at room temperature was that the kinks reconstructed to obtuse angled kinks. Therefore, before studying the structure of water above the surface in more detail it is worth looking at the final configuration of the two acute kinked surfaces interacting with water (figure 4.10 and figure 4.11). The water has been removed and the view is face down on the surface.

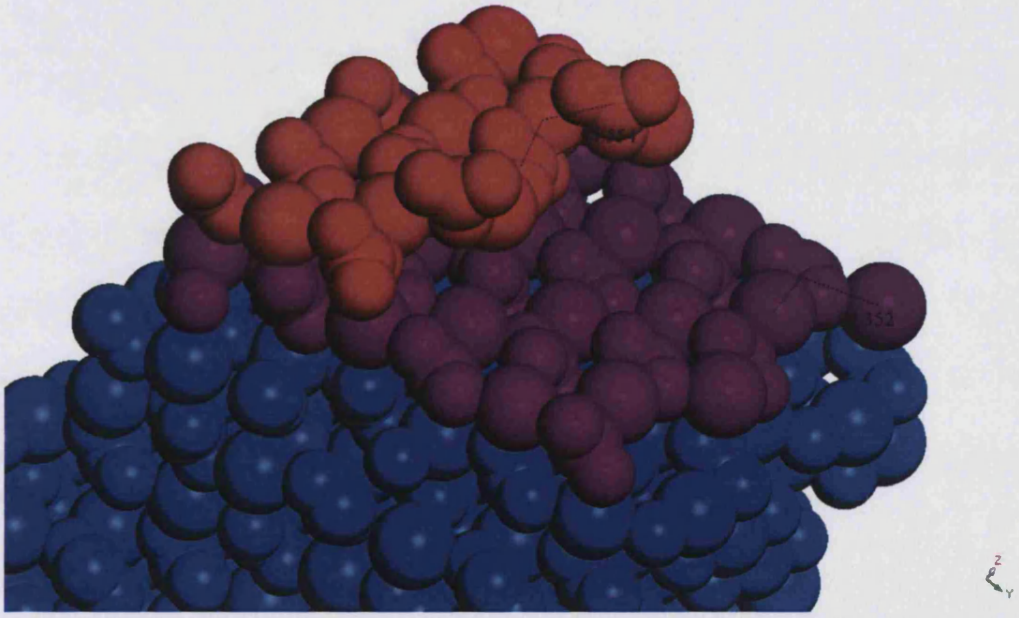

Figure 4.10: Final configuration of an obtuse-acute kinked calcite surface run with water above the surface

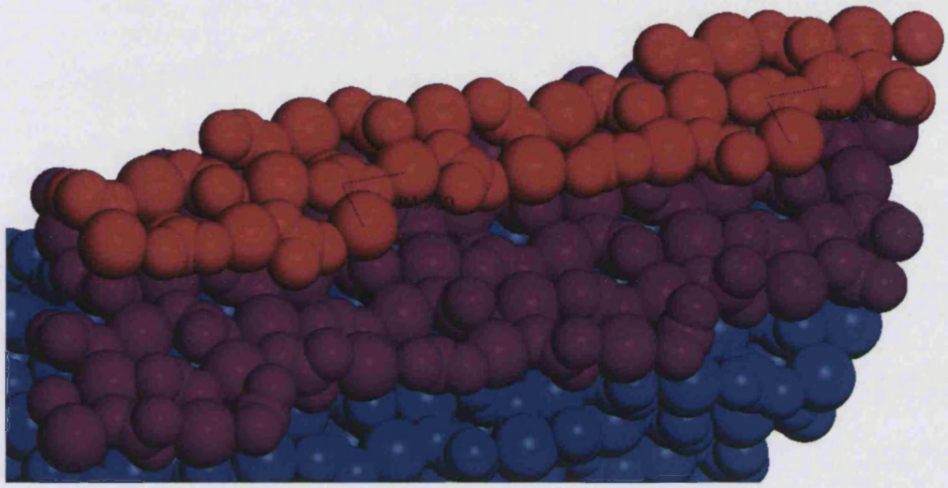

Figure 4.11: Final configuration of an acute-acute kinked calcite surface run with water above the surface

The final configuration reveals that the acute kinks have been stabilised somewhat by the water. The angles are still slightly above 90° but less than the final configuration simulated in vacuum. The 3-dimensional projections from the flat and stepped surfaces reveal points of adsorption that has occurred along edges and therefore by studying the structure of water above kinked surfaces we may be able to understand how the adsorption of water has stabilised the kinks on the surface.

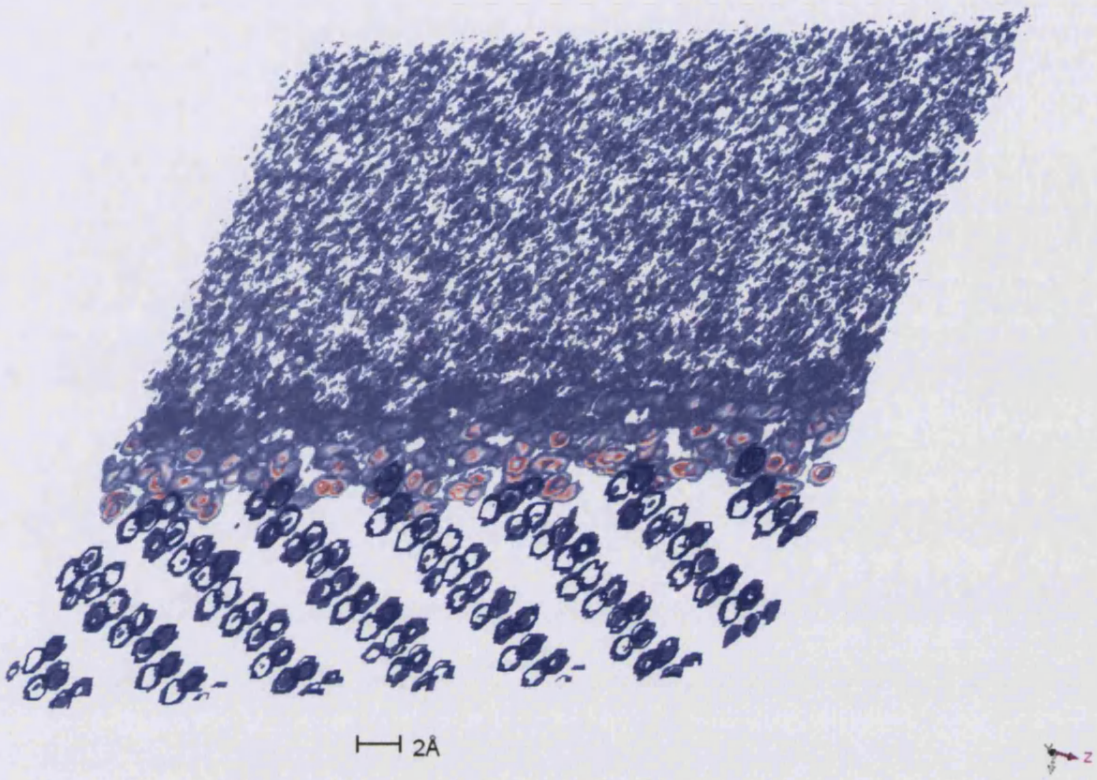

Figure 4.12: 3-dimensional projection of the structure of water above an acute-acute kinked calcite surface. Dark blue indicates a calcium ion, red indicates high water density and pale purple indicates low water density

A larger 34Å slab of water was placed above the four kinked surfaces so that the water structure could fully converge to its bulk value. Figures 4.12-4.15 shows the structure of water above all four kinked surfaces.

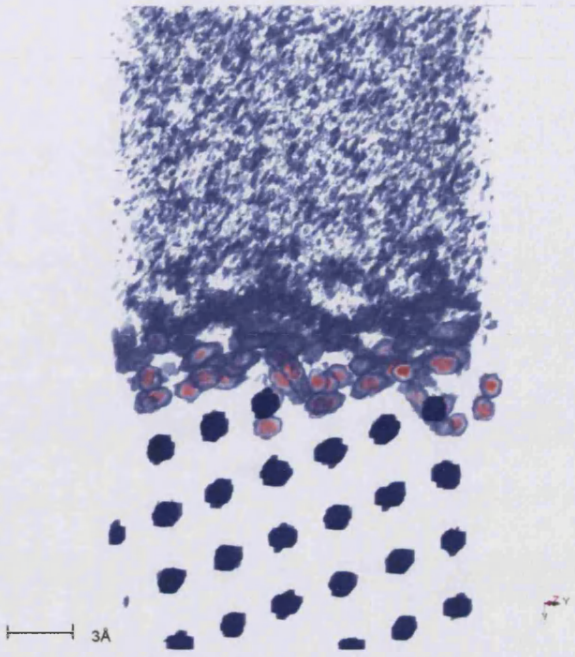

Figure 4.13: 3-dimensional projection of the structure of water above an acute-obtuse kinked calcite surface. Dark blue indicates a calcium ion, red indicates high water density and pale purple indicates low water density

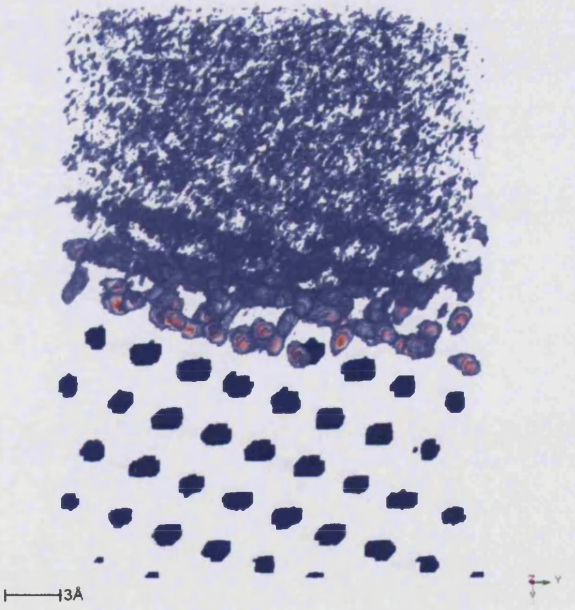

Figure 4.14: 3-dimensional projection of the structure of water above an obtuse-acute kinked calcite surface. Dark blue indicates a calcium ion, red indicates high water density and pale purple indicates low water density

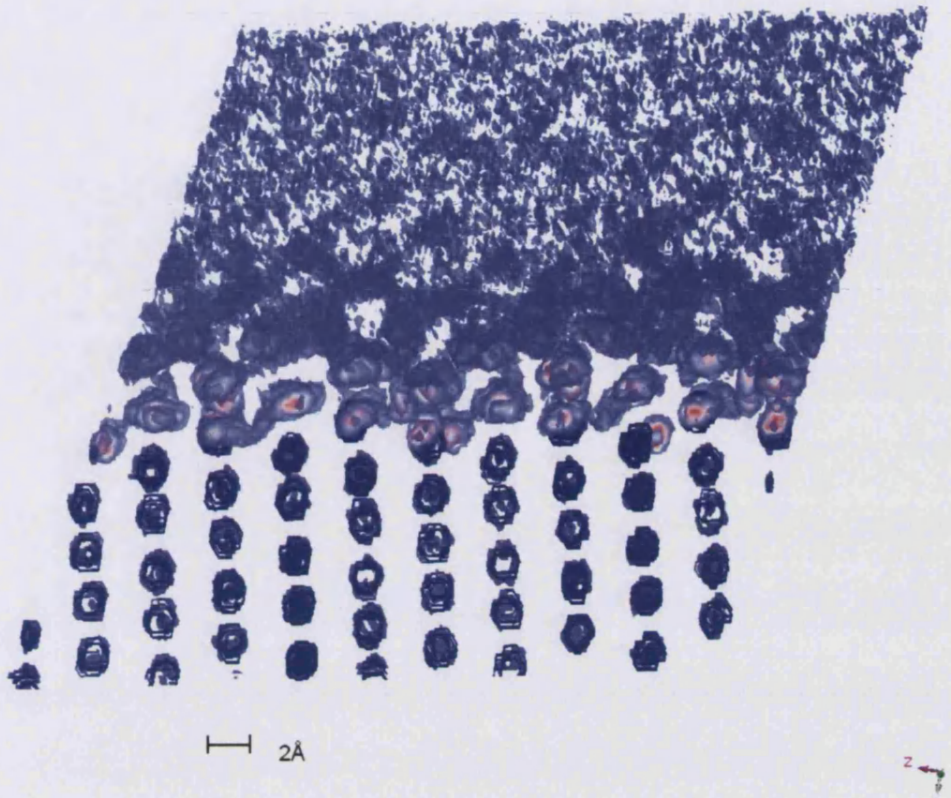

Figure 4.15: 3-dimensional projection of the structure of water above an obtuse-obtuse kinked calcite surface. Dark blue indicates a calcium ion, red indicates high water density and pale purple indicates low water density

The 3-dimensional projections do not show the ordered layering that was associated with the flat and stepped surfaces. The introduction of kinks has disrupted the layers of water in the second hydration layer above the surface. In all the projections there are regions of high density in the first layer which corresponds to the adsorption of water molecules on the surface. There is also increased localisation of water around the kink sites. Figure 4.16 shows a close up of the obtuse-acute kinked surface with the calcium terminated kink site circled. A water molecule, shown by the red area next to the circled calcium ion, has absorbed on to the surface. The position it has taken up is almost the lattice site of where a carbonate ion should be.

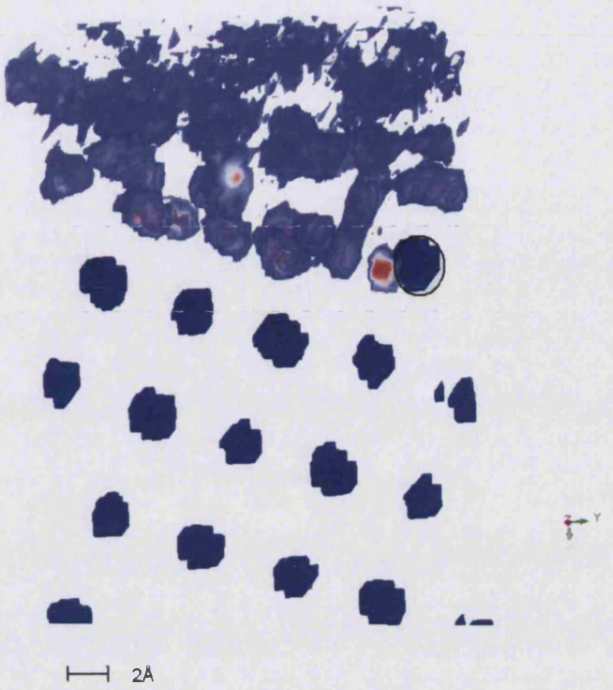

Figure 4.16: A Close up of a 3-dimensional projection of the calcium terminated kink site (circled) on the obtuse-acute kinked surface

This kinked surface has an obtuse step and, as in the obtuse stepped surface shown previously, there is delocalisation of water around the step edge as the water molecules alternate on two possible adsorption sites. However, it is still difficult to gauge how close the next nearest neighbour water molecules are to the various different surface sites. This can be achieved by examining the RDF of a calcium ion on the calcite surface and water.

The RDF provides a graphical representation of the amount of order the water has on the different surface sites. Figure 4.17 shows the RDF of a calcium ion on, a) a flat; b) an acute step; c) an obtuse step; d) an acute-acute kink; e) an acute-obtuse kink; f) an obtuse-acute kink,; and g) an obtuse-obtuse kink with water.

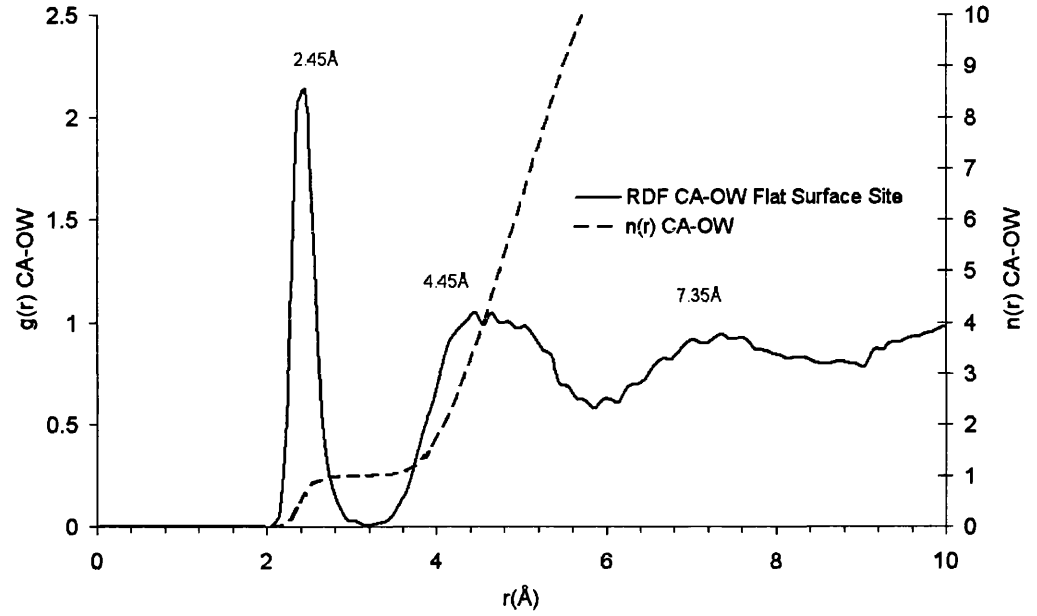
2.45Å
4.45Å
7.35Å
RDF CA-OW Flat Surface Site
n(r) CA-OW
g(r) CA-OW
n(r) CA-OW
r(Å)

a)

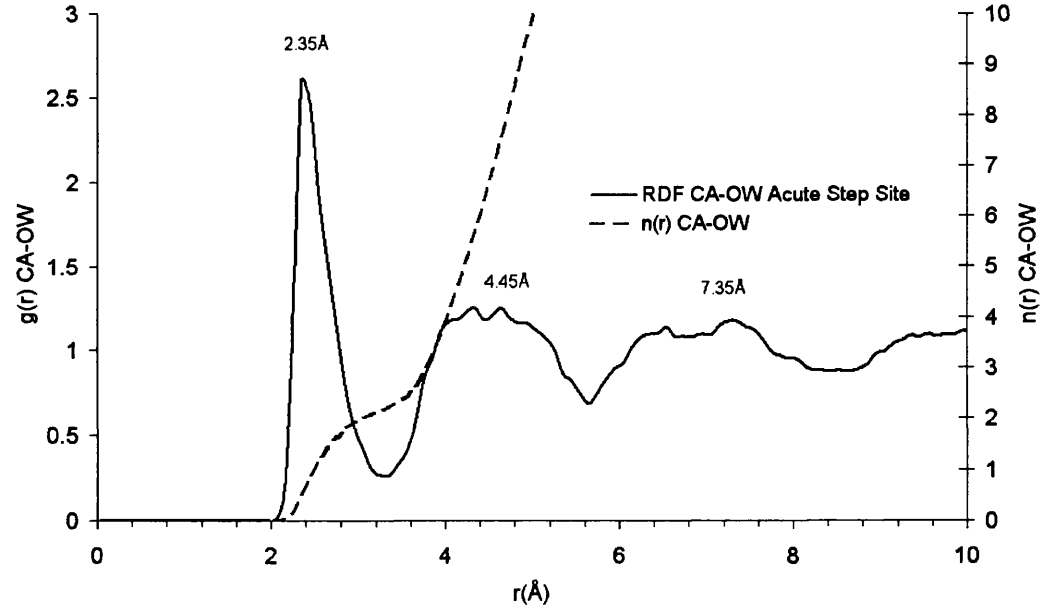
2.35Å
4.45Å
7.35Å
RDF CA-OW Acute Step Site
n(r) CA-OW
g(r) CA-OW
n(r) CA-OW
r(Å)

b)

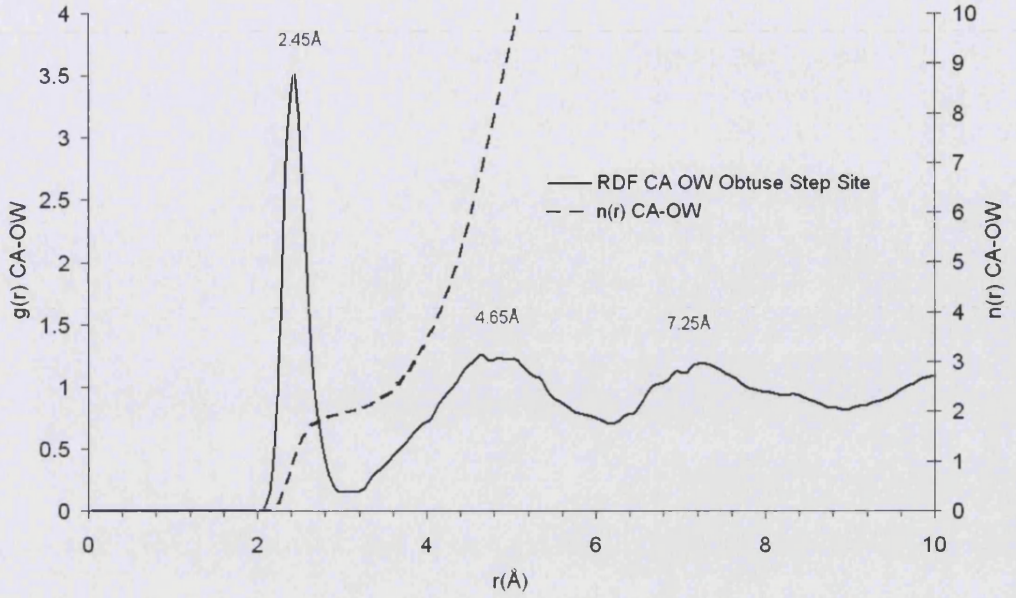
2.45Å
4.65Å
7.25Å
RDF CA OW Obtuse Step Site
n(r) CA-OW
g(r) CA-OW
n(r) CA-OW
r(Å)

c)

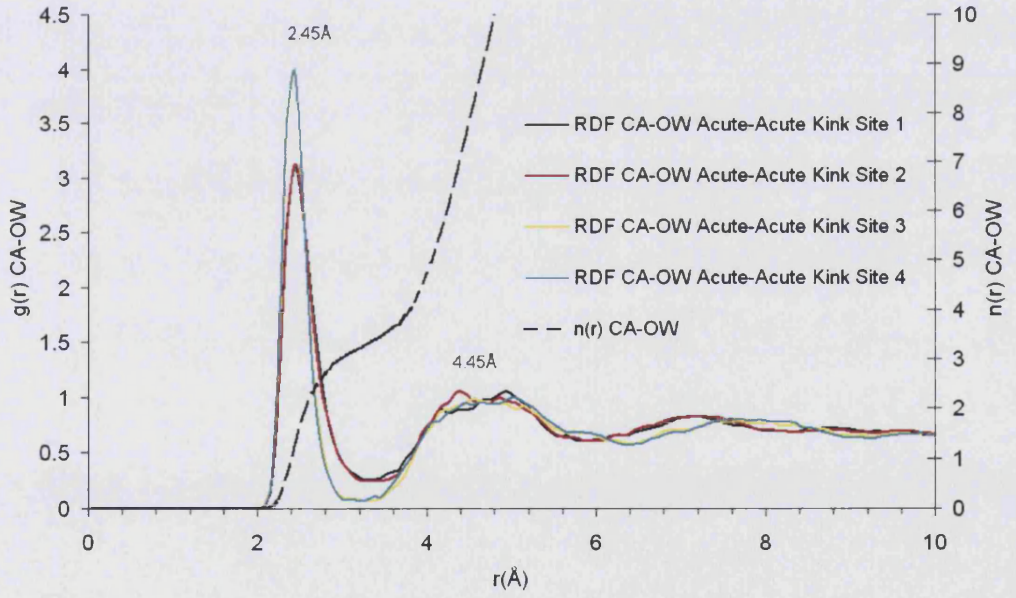
2.45Å
4.45Å
RDF CA-OW Acute-Acute Kink Site 1
RDF CA-OW Acute-Acute Kink Site 2
RDF CA-OW Acute-Acute Kink Site 3
RDF CA-OW Acute-Acute Kink Site 4
n(r) CA-OW
g(r) CA-OW
n(r) CA-OW
r(Å)

d)

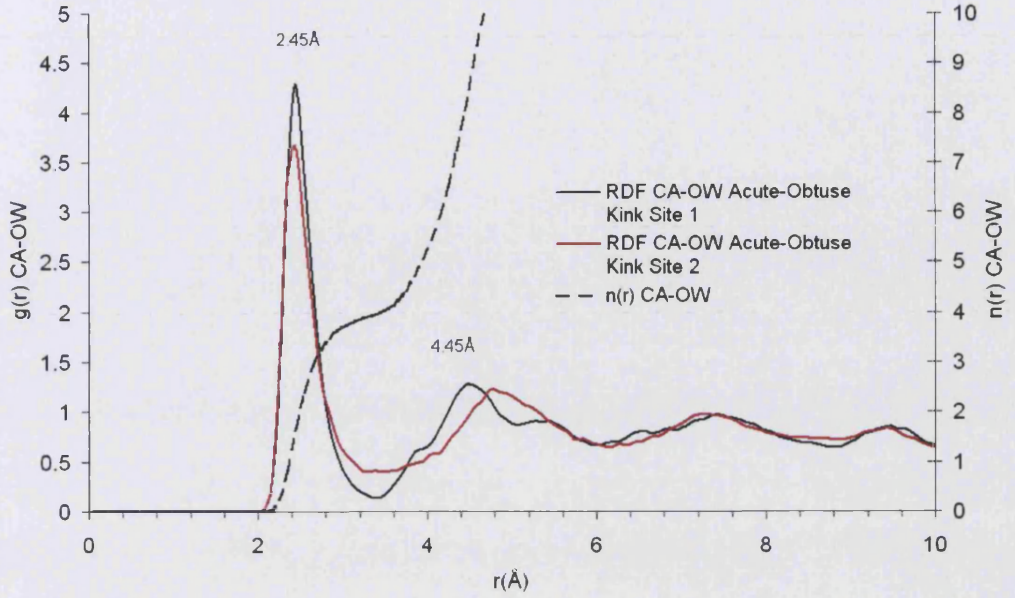
2.45Å
4.45Å
RDF CA-OW Acute-Obtuse Kink Site 1
RDF CA-OW Acute-Obtuse Kink Site 2
n(r) CA-OW
g(r) CA-OW
n(r) CA-OW
r(Å)

e)

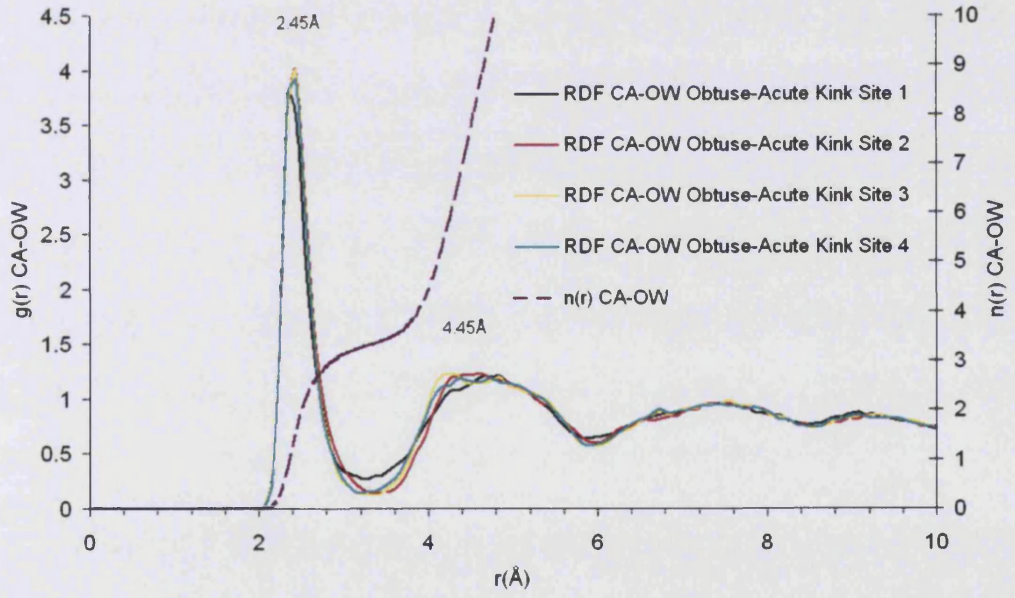
2.45Å
4.45Å
RDF CA-OW Obtuse-Acute Kink Site 1
RDF CA-OW Obtuse-Acute Kink Site 2
RDF CA-OW Obtuse-Acute Kink Site 3
RDF CA-OW Obtuse-Acute Kink Site 4
n(r) CA-OW
g(r) CA-OW
n(r) CA-OW
r(Å)

f)

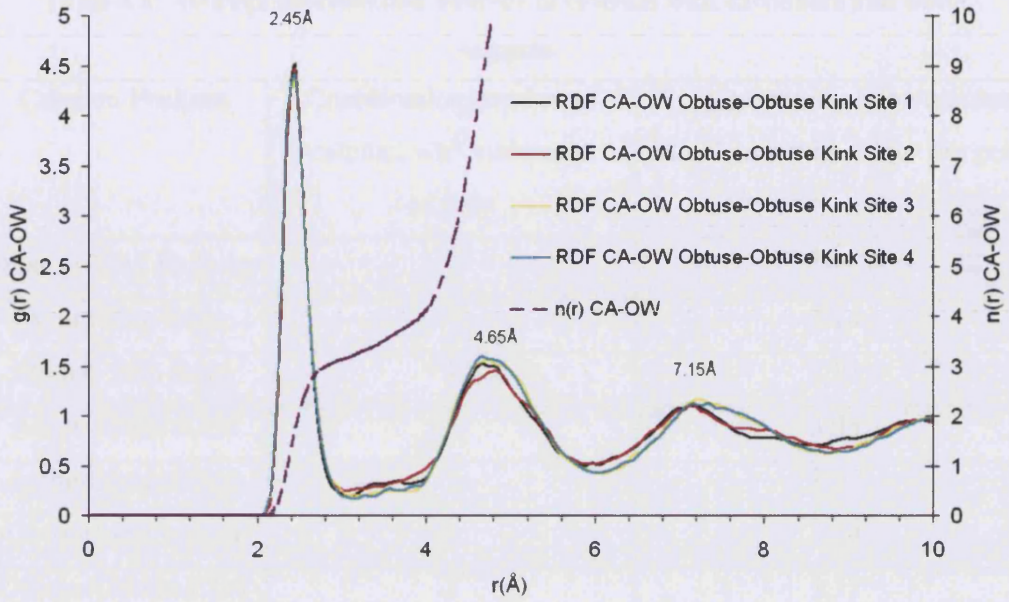

g)

Figure 4.17: Radial Distribution Function of a calcium ion on a) flat, b) acute step, c) obtuse step, d) acute-acute kink, e) acute-obtuse kink, f) obtuse-acute kink, and g) obtuse-obtuse kink and water

Figures 4.17d-g shows all RDF of the kink sites to see if there are any differences between sites on the same surface. The RDF from these different kink sites on the same surface shows no difference in the position of the nearest neighbouring water molecules. The RDF reveals that on all surfaces the next nearest neighbouring water molecule is 2.45Å from the calcium ion on a flat, stepped or kinked site. The RDF on the flat, acute and obtuse steps are very similar with peaks at 2.45Å, 4.50Å and 7.35Å. Interestingly, the only kinked surface that also has a third distinct peak is the obtuse-obtuse kinked surface. Integration of the area underneath the first minimum of the RDF will give the coordination number of a calcium ion in the different sites of the surface. As expected, a calcium ion on the flat surface has a coordination number of 1 with water oxygen and the same trend follows on the other surface sites. Table 4.4 shows the average coordination number of a calcium ion with the carbonate oxygen and water oxygen.

Table 4.4: Average coordination number of calcium with carbonate and water oxygens

Calcium Position	Coordination number of calcium with carbonate oxygen	Average coordination number of calcium with water oxygen
Flat $\{10\bar{1}4\}$ Surface	5	1.00
Acute Step Edge	4	2.14
Obtuse Step Edge	4	2.02
Acute-Acute Kink	3	3.35
Acute-Obtuse Kink	3	3.95
Obtuse-Acute Kink	3	3.34
Obtuse-Obtuse Kink	3	3.37

It is interesting to note that the coordination number of the calcium ion increases from 6-6.95 as the position on the surface changes. This increase in coordination number could be due to calcium ions having an increased effective size due to there being more strain at these positions.

One property that can be calculated for indicating how tightly bound a water molecule is in the first hydration layer of the calcite surface is the water residence time. This is obtained from the residence-time correlation function [211], which is defined as:

$$\langle R(t) \rangle = \left\langle \frac{1}{N_0} \sum_{i=1}^{N_i} \theta_i(0)\theta_i(t) \right\rangle \tag{4.1}$$

Where N is the number of water molecules in the first hydration layer and θ_i is the Heaviside function, which is 1 if the ith water molecule is in the first hydration layer at time t and zero otherwise. A water molecule was counted as having left the first layer if it has done so for at least 2ps. Since our water is a dynamic model this

allows a water molecule enough time to be counted in the residence time. The residence time can be obtained by integration of $\langle R(t) \rangle$:

$$\tau = \int_0^\infty \langle R(t) \rangle dt \tag{4.2}$$

Table 4.5 shows the residence time of a water molecule in the first hydration layer at different sites of a calcite surface.

Table 4.5: Average residence time (ps) of a water molecule in the 1st hydration shells on different calcite site and the surface energies of the surface in vacuum

Calcite Surface Site	Residence Time in the 1st Hydration Shell (ps)	Surface Energy (J/m^2)
Flat $\{10\bar{1}4\}$ Surface	292.15 ± 122.84	0.60
Acute Step Edge	247.61 ± 122.34	0.69
Obtuse Step Edge	295.73 ± 119.49	0.65
Acute-Acute Kink	194.71 ± 105.54	0.87
Acute-Obtuse Kink	283.48 ± 218.87	0.80
Obtuse-Acute Kink	117.38 ± 53.48	1.01
Obtuse-Obtuse Kink	150.77 ± 51.16	0.67

The residence time of a water molecule on a flat surface is in good agreement with previous studies [68, 204]. The residence times of the first hydration shell at the step edges are of the same order as the flat surface, which again implies that the layering of water above stepped surfaces is not disrupted by the introduction of a step. The residence times around the two kinks on an acute step are similar to the residence time at the acute step. However, the two kinks on an obtuse step have a much lower residence time than on a pure obtuse step. It is difficult to interpret these residence times accurately due to the very high errors associated with the calculations.

It is interesting to point out that the two most stable surfaces, the flat and obtuse steps, have the two highest residence times and the least stable obtuse-acute kinked surface has the lowest residence time. This indicates that the more stable the surface is the more likely a water molecule will adsorb on to the surface. Furthermore, experimentally the slowest growth and dissolution will be associated with the flat surface and the faster growth is at the obtuse surface kinks. The experimental kinetics correlates better with the rate of exchange with water. If we are to explore the rates in more detail we need information on the free energies of growth and dissolution.

The next section investigates the dissolution of ions from the flat and stepped surfaces.

4.4 Free Energy of Dissolution from Calcite Surfaces

4.4.1 Dissolution from a Flat Surface

In 2005, Kerisit *et al.* used the thermodynamic integration method to investigate the free energy of adsorption of ions onto the flat neutral $\{10\bar{1}4\}$ calcite surface [68]. The study showed that the free energy profile is strongly influenced by the water density above the surface and that there are two main energy wells which correspond to the formation of the inner- and outer-sphere complexes. In this chapter we describe the free energy profile to remove matter from the surface. The molecular dynamics simulations described in this chapter were all performed using thermodynamic integration to describe the free energy change of dissolving a surface ion into solution. All systems were simulated in the NVT ensemble by use of the Nose-Hoover thermostat [184] with a relaxation time of 0.5ps. All calculations were performed at a temperature of 300K and zero applied pressure.

The Coulombic interactions were calculated using the smooth particle mesh Ewald sum [212]. In all simulations we use a real space cut-off of 8Å and the same cut-off was used for the short-range interactions. The trajectories were generated using the Verlet-Leapfrog algorithm with a time step of 0.2fs. The mass of the shells were set to 0.2a.u and their motion treated as that of the cores following the adiabatic approach first introduced by Mitchell and Fincham [213].

The free energy of dissolution of a calcium ion and a carbonate ion from the flat $\{10\bar{1}4\}$ surface was first investigated. The starting configuration of all the dissolution calculations was taken from the end of the 1ns MD NPT simulation so that the system is already at equilibrium. Twenty independent calculations above the flat calcite surface were performed, where the calcium ion was pulled out of the surface and constrained at heights ranging from 0.4 to 9Å above the surface. The force in the direction of the normal to the surface is averaged over a further 160ps. The free energy is obtained by integrating the average force as a function of distance from the relaxed position of the ion in the surface. Therefore, the procedure, as a whole, involves the dissolution of an ion and the creation of a vacancy on the surface.

Figure 4.18 shows the free energy profile of the dissolution of a calcium and a carbonate ion from the $\{10\bar{1}4\}$ flat surface. There is an increase of free energy which converges at around 5Å above the surface, where the water density approximates the bulk value.

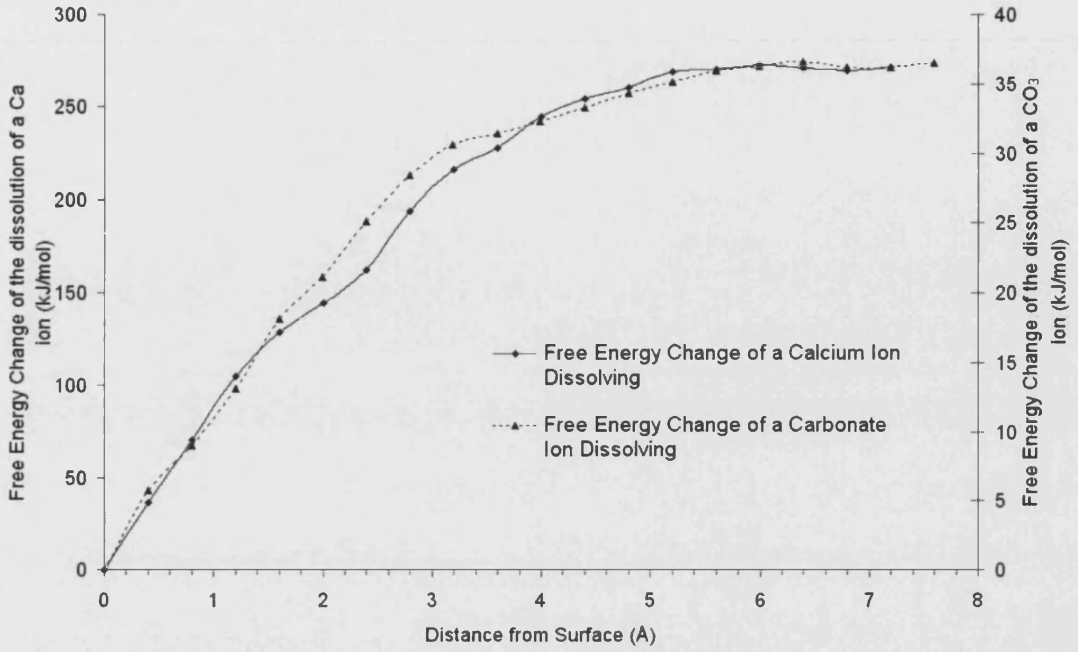

Figure 4.18: Free energy profile of the dissolution of a calcium and carbonate ion from a flat calcite surface

The ion that is being dissolved can still interact with the vacant site, even though there are layers of water between. There is no local minimum and hence there seems to be no stabilisation of an inner-sphere complex and only the formation of an outer-sphere complex causes convergence of the free energy. Another important feature of figure 4.18 is that the calcium ion free energy profile converges at around 270kJ/mol whereas the carbonate ion free energy profile converges a great deal lower at around 36kJ/mol. This clearly shows that the rate determining step for dissolution is the removal of the cations.

In addition to the free energy profiles of dissolving ions from the surface we have also performed MD simulations of dissolving an "on-top" ion from the surface, i.e., the dissolution of an isolated ion sitting in a lattice site above the plane of the surface. To allow comparisons to be made, a vacancy is created on the other face of the mineral slab and therefore the system has no net charge. The free energy

profiles of an "on-top" calcium and carbonate ion being dissolved are shown in figure 4.19.

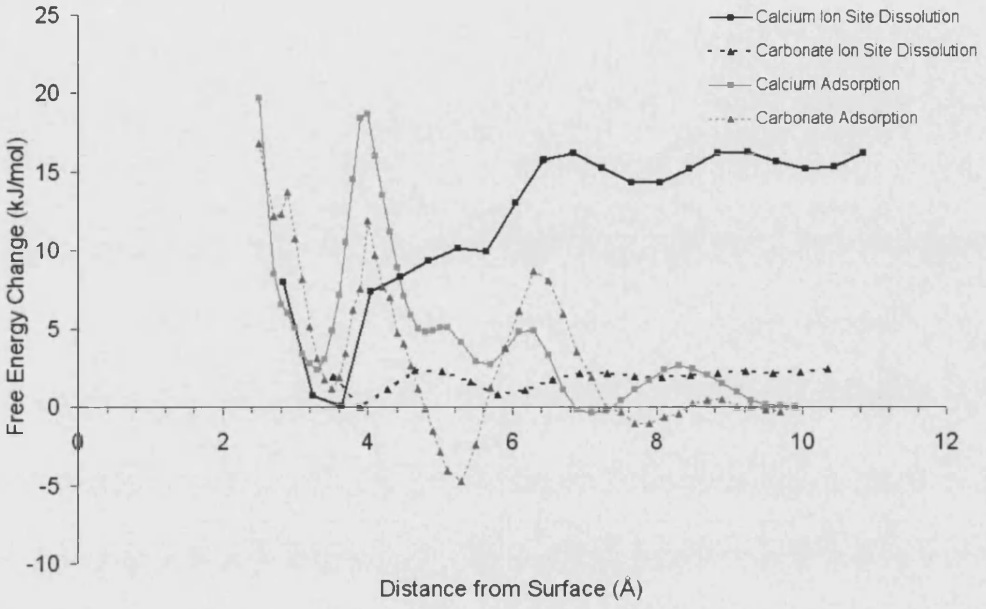

Figure 4.19: Free energy profile of the dissolution of a calcium and carbonate ion from the "on-top" site. For reference, the free energy of adsorption of calcium and carbonate ions has been included from the Kerisit and Parker study [68].

We find that the calcium and carbonate ion free energy change is 16.2 and 2.4kJ/mol, respectively. It is not surprising that in any dissolution process, these "on-top" ions are likely to dissolve first. In addition, the figure above shows that the inner-sphere complex at 3.2Å is more stable than the outer sphere complex at about 4.5Å, in contrast to the study performed by Kerisit. In these simulations the slab is oppositely charged to the leaving ion. However, previous results on the interaction of the charged ions on neutral surfaces found that the outer-sphere complexes were most stable [67, 68].

4.4.2 Dissolution from Stepped Surfaces

The same process was repeated for the acute and obtuse steps. The ions chosen in these simulations were those that formed the edge of the steps. Figure 4.20a shows the free energy profile of the dissolution of a calcium ion from the acute and obtuse stepped surfaces, and for comparison the free energy of removing calcium from a flat surface. The free energy needed to dissolve a calcium ion from a flat surface is far greater than the free energy to dissolve an ion from a stepped surface. This is in agreement with both experimental [72] and computational studies [71, 154].

The sensitivity of the simulation results suggests it is not possible at the moment to propose whether or not one step is easier to dissolve than another because the free energies are so close, with an energy difference of 5.2kJ/mol. However, what is apparent is that with an energy difference of 104.9kJ/mol, the dissolution of calcium ions from a flat surface is far more unfavourable than from a stepped surface.

The same procedure was followed for simulating the dissolution of a carbonate ion from flat and stepped surfaces. Figure 4.20b shows the free energy of dissolution of a carbonate ion from these surfaces. Again, the same trend is shown with a dramatic decrease in free energy from the edge compared to the flat surface. Indeed, the difference between the dissolution free energy from flat and stepped surfaces is 10.9kJ/mol. However, the free energy of dissolution is much lower than that of calcium.

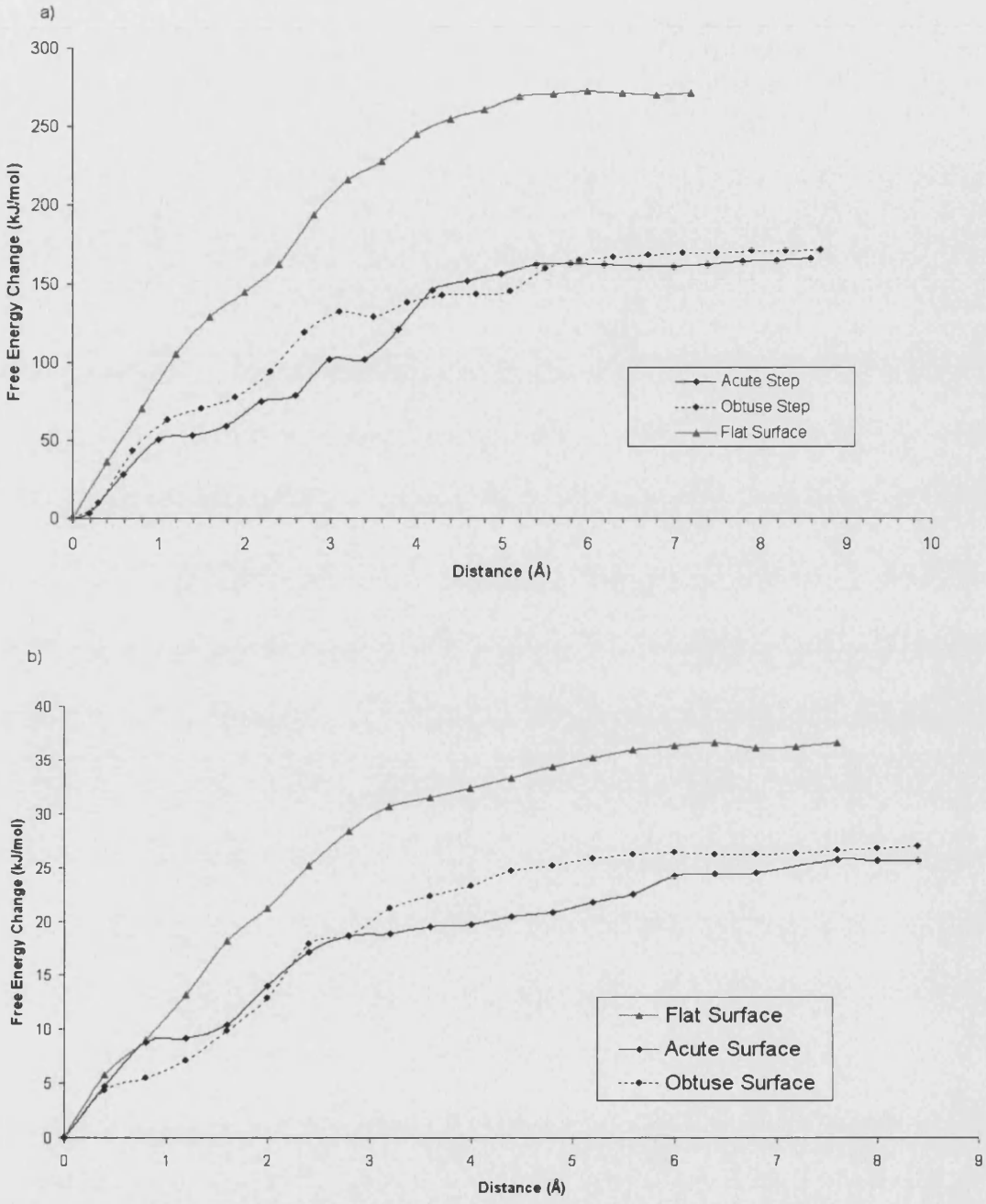

Figure 4.20: Free energy profile of the dissolution of (a) a calcium ion and (b) a carbonate ion from stepped surfaces

In all cases the dissolution of an isolated ("on-top") ion is more favourable than that of a step-edge ion, which in turn is more favourable than that of an ion from a terrace. The ratios of the free energies for the different processes are reasonably constant. This suggests that this approach could be used for developing more sophisticated parameterisations of solid-on-solid dissolution models [71, 72]. These models assume a linear relationship between the dissolution energy and the number of first shell surface bonds that need to be broken. For example, in this model it is suggested that if there is an isolated ion on the surface (an "on-top" ion), its dissolution energy should be four times less than a surface ion on a step and five times less than a surface ion on a flat surface. Figure 4.21 illustrates a schematic representation of the solid-on-solid model.

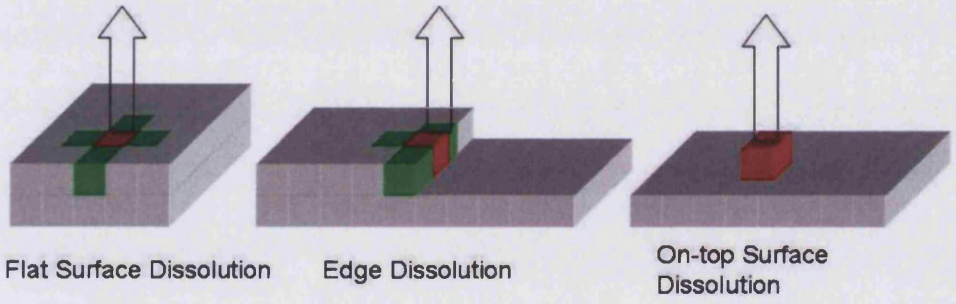

Figure 4.21: Schematic representation of the solid-on-solid model where the red cube is the dissolving atom and the green cubes are the atoms whose bonds need to be broken

From the above results, it is suggested that by considering an explicit dynamic model of water the energy differences do not follow the same trends as in the solid-on-solid model. In both calcium and carbonate dissolution simulations, the free energy change of dissolution from a flat surface site is 16 times greater than that of an "on-top" ion offering evidence that the interaction with interfacial water molecules is playing a role in the dissolution process.

The next section of this chapter involves a more complex simulation when we consider the interaction of the flat $\{10\bar{1}4\}$ calcite surface and a polymeric additive, polyacrylic acid. However, before considering the mineral-polymeric additive interactions, a brief introduction to polyacrylic acid is needed and how a reliable potential was derived.

4.5 Polyacrylic Acid in Water

Acrylic acid or 2-propenoic acid has the formula $C_3H_4O_2$ and it is the simplest unsaturated carboxylic acid with both double bond and carboxyl group linked. Acrylic acid is a clear, colourless liquid with a characteristic acrid odour and is miscible with water. Polyacyrlic acid (PAA) can be readily formed into the sodium and calcium salt with both salts behaving differently in solution. The sodium PAA salt dissociates into a negatively charged macroion and mobile sodium counterions [214]. It can be used, for example, as a dispersing agent for pigments and as an encrustation inhibitor in laundry detergents [215]. The calcium PAA salt reveals that the solution exhibits a complex phase behaviour depending on the nature and the concentration of the counterions [216, 217].

The potential model of PAA and its salts are described in chapter 2. The potential was derived from a recent study where the interactions between steric acid and calcite surfaces were studied [77, 155]. To test the potential, two MD simulations were performed. The first MD simulation contained each polymer in vacuum and the second was to evaluate its stability in aqueous conditions. Figure 4.22 shows the initial configuration of the calcium PAA salt and figure 4.23 shows the initial configuration of the sodium PAA salt. Each has a chain of ten monomers and the negative charge is countered by five calcium ions and ten sodium ions. The cations were placed randomly along the chain.

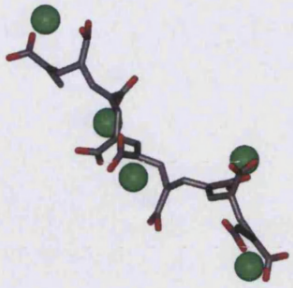

Figure 4.22: Initial configuration of PAA-Ca

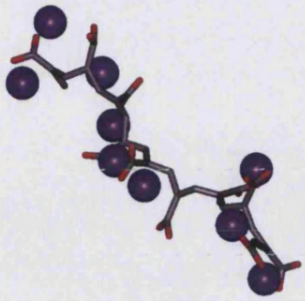

Figure 4.23: Initial configuration of PAA-Na

A 1ns MD simulation was performed in vacuum using an NVT ensemble at 300K and zero applied pressure to test the stability of the potential. Figures 4.24 and 4.25 shows the final configurations of the two salts. Both show that the potential is flexible enough to keep the chain together even though the chain would not like to be as rigid as in the initial configuration. This is due to the negatively charged carboxylate groups trying to bond with a maximum number of cations.

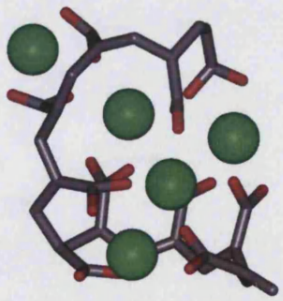

Figure 4.24: Final configuration of PAA-Ca after a 1ns MD simulation in vacuum

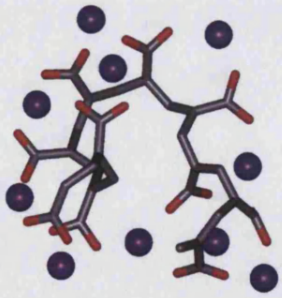

Figure 4.25: Final configuration of PAA-Na after a 1ns MD simulation in vacuum

The same starting configurations shown in figures 4.22 and 4.23 were also used in a simulation which included water. A single PAA salt was immersed in a box of water and a molecular dynamics simulation was performed in the NPT ensemble at 300K and zero applied pressure. The cubic simulation cell had a side length 29.8Å on average and contained just over 1100 water molecules. A Nose-Hoover thermostat and Hoover barostat with parameters for the relaxation time of 0.5ps was employed for the MD simulation. The simulations were run for 1ns each with the first 200ps used in the equilibration period. Figure 4.26 and 4.27 shows the evolution of the potential energy of the two systems as a function of time.

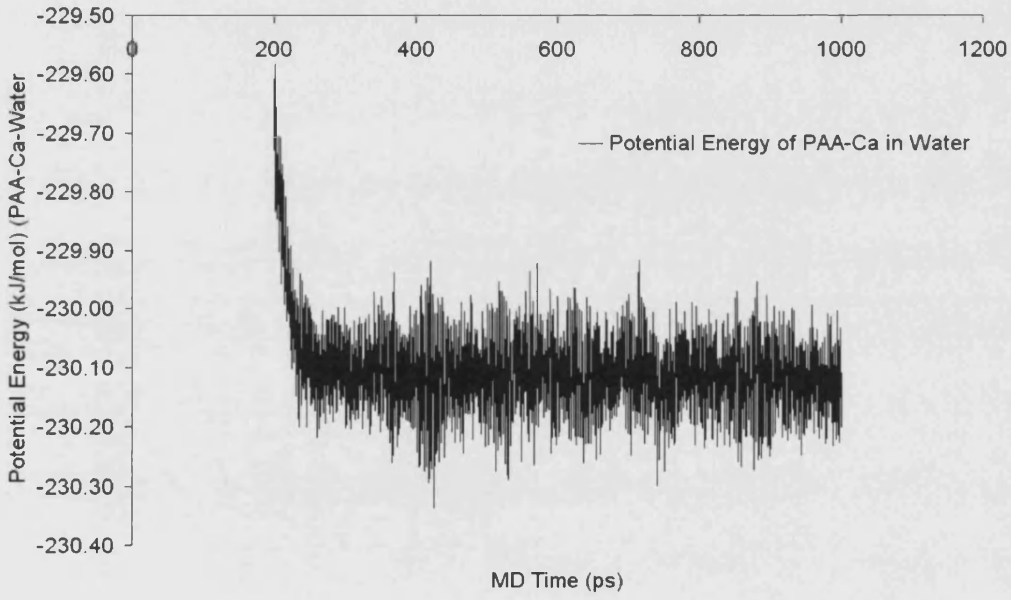

Figure 4.26: Evolution of potential energy as a function of time for the PAA-Ca in water simulation

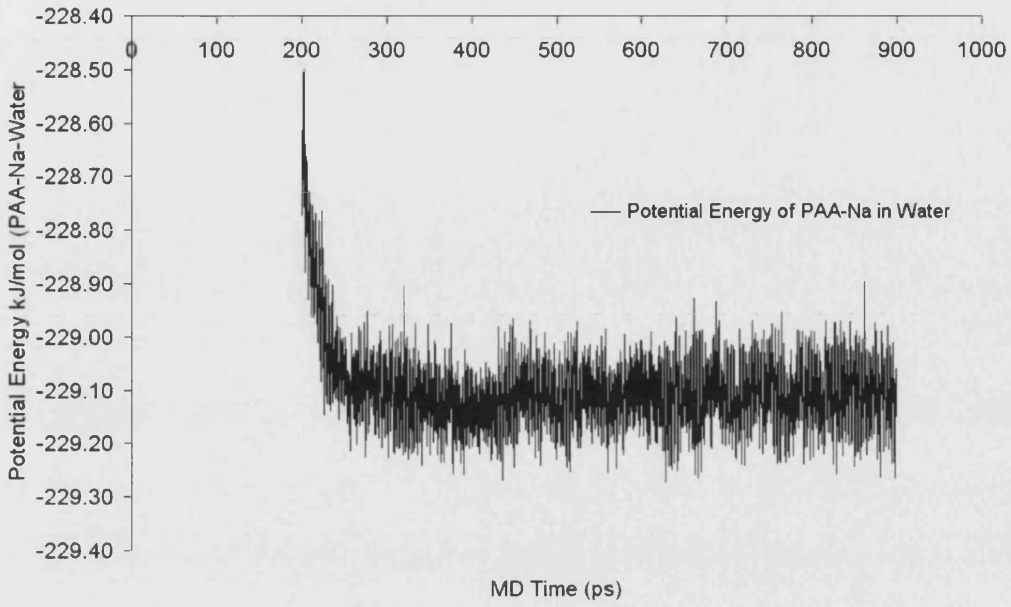

Figure 4.27: Evolution of potential energy as a function of time for the PAA-Na in water simulation

The potential energy converges to an average value of -230.1kJ mol^{-1} for the calcium salt and -229.1kJ mol^{-1} for the sodium salt. This indicates that both systems have reached equilibrium and the configuration adopted for each polymeric additive is at its most stable.

The final configurations of the PAA molecules are shown in figure 4.28 for the calcium salt and 4.29 for the sodium salt.

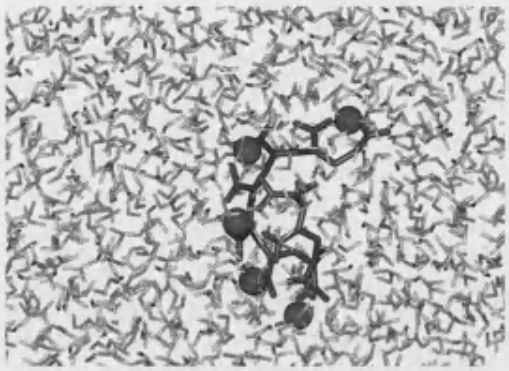

Figure 4.28: Final configuration of PAA-Ca after a 1ns MD simulation in water

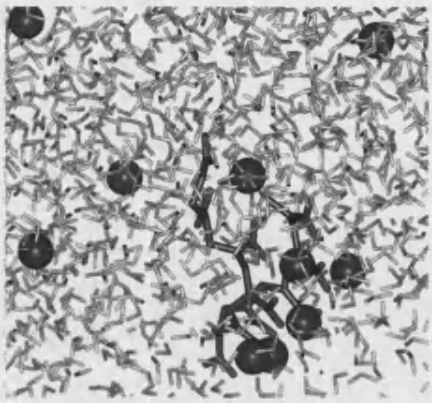

Figure 4.29: Final configuration of PAA-Na after a 1ns MD simulation in water

The MD simulations of the PAA salts in water show that the two salts behave in different ways. As found experimentally [216, 217], the calcium ions on the PAA-Ca salt stays very closely coordinated with the carboxylate groups. The calcium ions stay approximately 2Å away from the carboxylate groups. In contrast, the sodium ions in PAA-Na are easily solvated into solution. Figure 4.29 reveals that five of the sodium ions are solvated by water and the other five stay closely coordinated to the carboxylate groups, at a distance of 2Å. The easily solvated sodium ions and the highly coordinated calcium ions with the carboxylate groups are also seen in a MD study performed with the PAA salts by Molnar in 2005 [214]. To assess the orientation of carboxylate groups with each other, the RDF for carboxylate carbon ions is evaluated. Figure 4.30 displays the RDF of carboxylate carbon atom pairs.

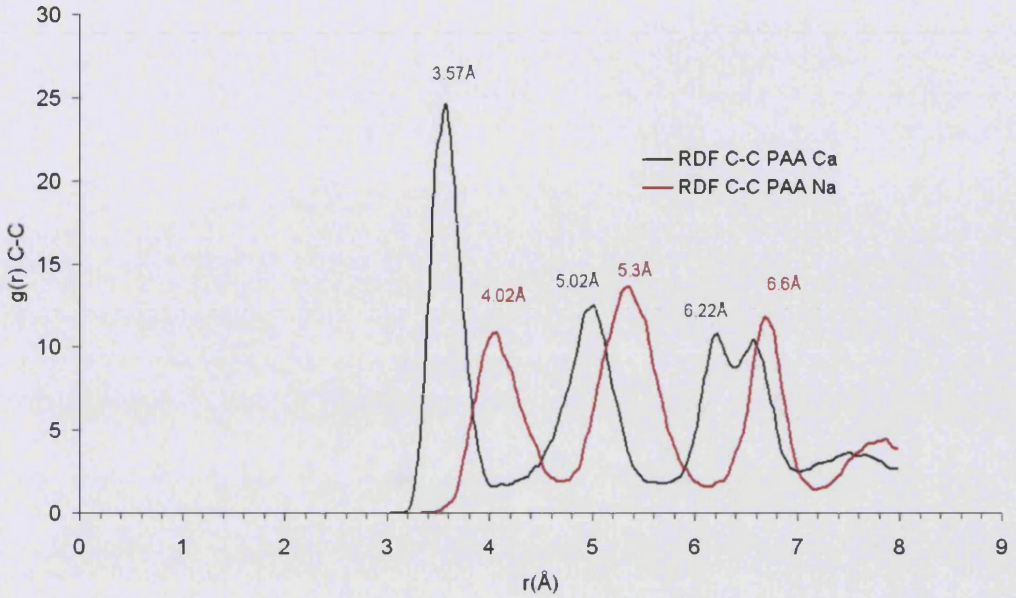

Figure 4.30: RDF for carboxylate carbon ions on PAA (black line for the calcium salt and red line for the sodium salt)

The RDF reveals that the calcium salt has a slightly more close-packed structure than the sodium salt. The first peak on the calcium salt is at 3.57Å whereas the first peak on the sodium salt is 0.45Å further away at 4.02Å.

Table 4.6 shows the residence times and average coordination number of the calcium and sodium ions with the oxygen of the water and the oxygen of the carbonate. In the MD simulation some of the sodium ions are easily solvated and their average residence times and average coordination numbers with the oxygen of the carbonate is the lowest. The highly coordinated calcium ions with the oxygen of the carbonates are reflected in the average residence times, which were calculated to be 529.21±101.12.

Table 4.6: Average residence time and average coordination number of calcium and sodium ions from PAA molecule with oxygen-water and oxygen-carbonate

Cation	Average residence time with oxygen-water (ps)	Average coordination with oxygen-water	Average residence time with oxygen-carbonate (ps)	Average coordination with oxygen-carbonate
Ca	80.21±14.42	4.09	529.21±101.12	3.69
Na	24.79±14.52	2.99	277.92±5.21	4.05
Solvated Na	30.63±4.17	5.55	174.61±0.64	1.01

4.6 Polyacrylic Acid on Flat Calcite Surface

Two MD simulations were set up where each of the PAA salts were immersed in water above a flat $\{10\bar{1}4\}$ calcite surface. The calcite surface area was 24.10 by 23.98Å and each simulation contained a 30Å thick slab of water and corresponds to just fewer than 650 water molecules. The polymer was initially placed 8Å above the surface. A vacuum gap of 55Å was included between repeating solid/aqueous slabs. To ensure that no water molecules drifted across the vacuum gap while the simulation evolved, all systems were subjected to a 200ps MD simulation at NVE ensemble and at zero temperature. This removed any excess energy formed from the packing of water molecules to set up the starting configuration. The final configurations of the NVE MD simulations were used as the starting configuration of the NVT MD simulations at 300K and zero applied pressure. A Nose-Hoover thermostat, with a relaxation time parameter of 0.5ps, was used for the MD simulations. The simulations were each run for 600ps, with the first 200ps used for the equilibration period.

4.6.1 Interfacial Energy

One of the properties that can be estimated from these simulations is the interfacial energy of the polymeric additive in solution on a calcite surface. This gives an indication as to how easily the polymer can be adsorbed onto the surface. The interfacial energy was calculated from the difference between the energies of two-dimensional blocks of atoms. The blocks of atoms were made up of either a slab of calcite crystal, terminated by the $\{10\bar{1}4\}$ surface, liquid water, liquid water with the polymeric additive immersed within, or a combination of these [155].

The interfacial energy is calculated by equation 4.3:

$$\gamma_{CW} = \frac{\left(E_I - \frac{E_{II}}{2} - \frac{E_{III}}{2}\right)}{A} \tag{4.3}$$

Where γ_{CW} is the crystal/water interfacial energy, E_I is the average potential energy of the crystal water MD simulation, E_{II} is the average potential energy of a solid/solid MD simulation, E_{III} is the average potential energy of a water/water MD simulation, and A is the surface area of the solid. The crystal/water interfacial energy is calculated from the difference between the energy of a pure crystal and a pure water block, as shown in figure 4.31. This method has been successfully applied to calculating the interfacial energies between hydrophobic SAM's and calcite surfaces [76, 77, 155].

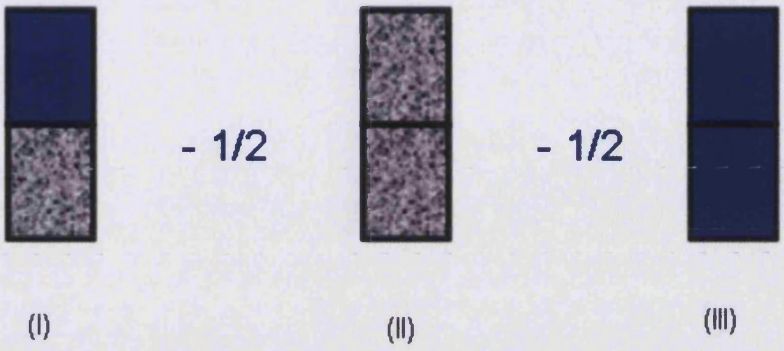

Figure 4.31: Schematic representation of the crystal/water interfacial energy. The marble grey block indicates a solid and a blue block indicates a slab of water.

The same strategy can be used to calculate the interfacial energy of hydrophilic polymeric additives, such as PAA, in solution on calcite surfaces. Figure 4.32 shows a schematic representation of the polymeric additive in solution/solid interfacial energy:

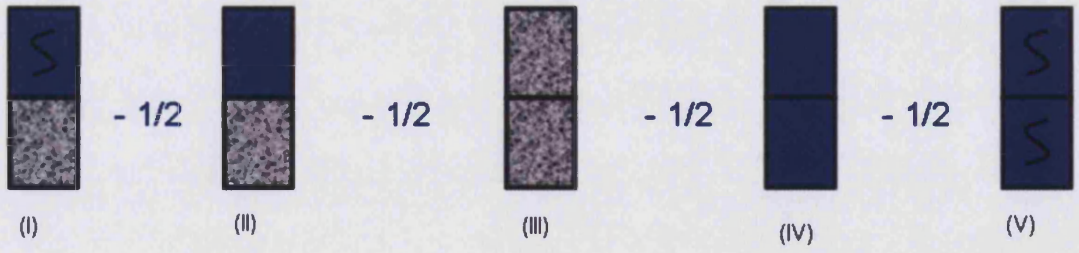

Figure 4.32: Schematic representation of the crystal/polymeric additive in solution interfacial energy. The marble grey block indicates the crystal, a blue block indicates a slab of water, and a blue block with a black line in it indicates a polymeric additive solution.

Using the schematic shown in figure 4.32 the interfacial energy can be re-written as in equation 4.4:

$$\gamma_{CWP} = \frac{\left(E_I - \frac{E_{II}}{2} - \frac{E_{III}}{2} - \frac{E_{IV}}{2} - \frac{E_V}{2}\right)}{A} \tag{4.4}$$

Where γ_{CWP} is the crystal/polymeric additive in solution interfacial energy, E_I is the average potential energy of the crystal water MD simulation, E_{II} is the average potential energy of a crystal/water MD simulation, E_{III} is the average potential energy of a crystal/crystal MD simulation, E_{IV} is the potential energy of the water/water MD simulation, E_V is the potential energy of the polymeric additive in solution MD simulation and SA is the surface area of the solid. In each case the reason for dividing the energy by two is so that it cancels out the vacuum/solid and vacuum/aqueous interfacial effects and therefore the only difference should be the different polymeric additive used in the simulation.

Figures 4.33 and 4.34 show the final configuration of the 600ps MD simulation of a PAA-Ca and PAA-Na molecule, respectively, on the flat calcite surface.

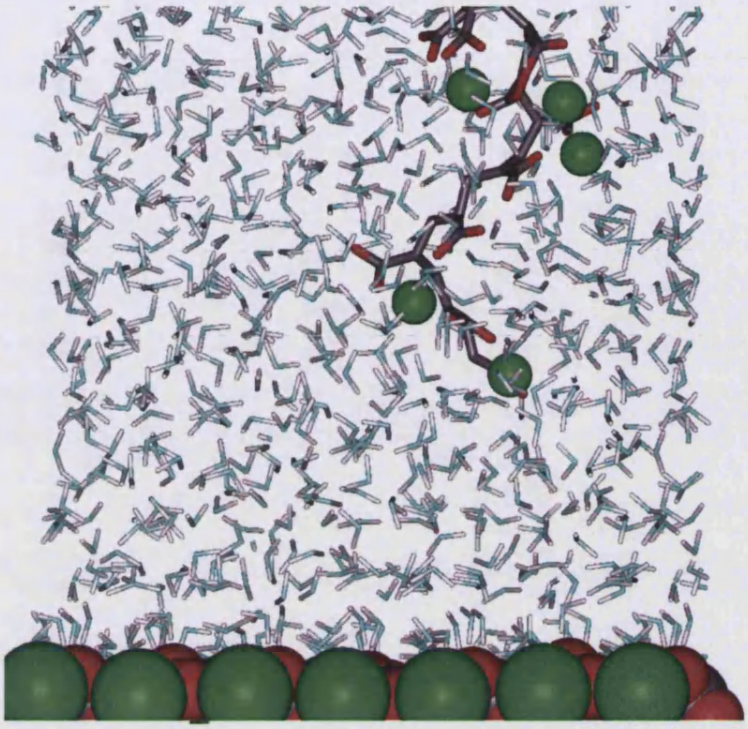

Figure 4.33: Final configuration of a PAA-Ca molecule in solution on a flat calcite surface

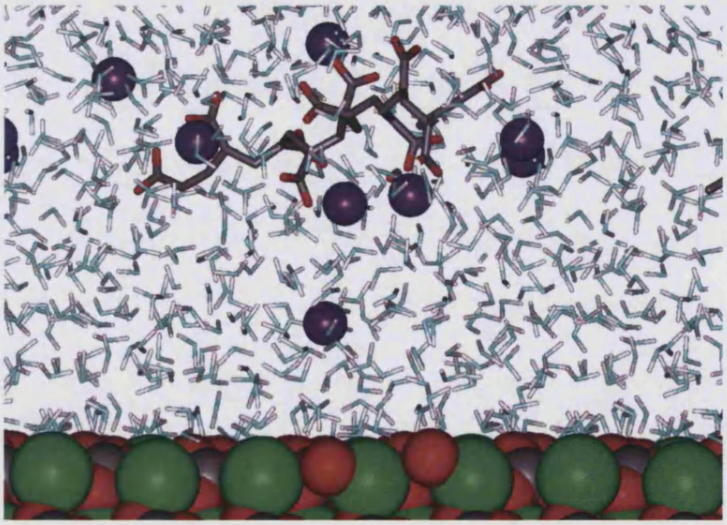

Figure 4.34: Final configuration of a PAA-Na molecule in solution on a flat calcite surface

The final configurations of both molecules indicate that there has been no adsorption on the surface of the flat calcite surface. One explanation for this is that there is no driving force for adsorption. As was shown in section 4.3.1, there are layers of water that form above the surface of the flat calcite surface. In a previous study of adsorption of ions onto the calcite surface, the layering of water has an effect on the free energy of adsorption [67, 68]. Therefore, there are free energy barriers to overcome when passing through areas of high water density.

The RDF between the carbons of the carboxylate groups on each chain were compared (figure 4.35).

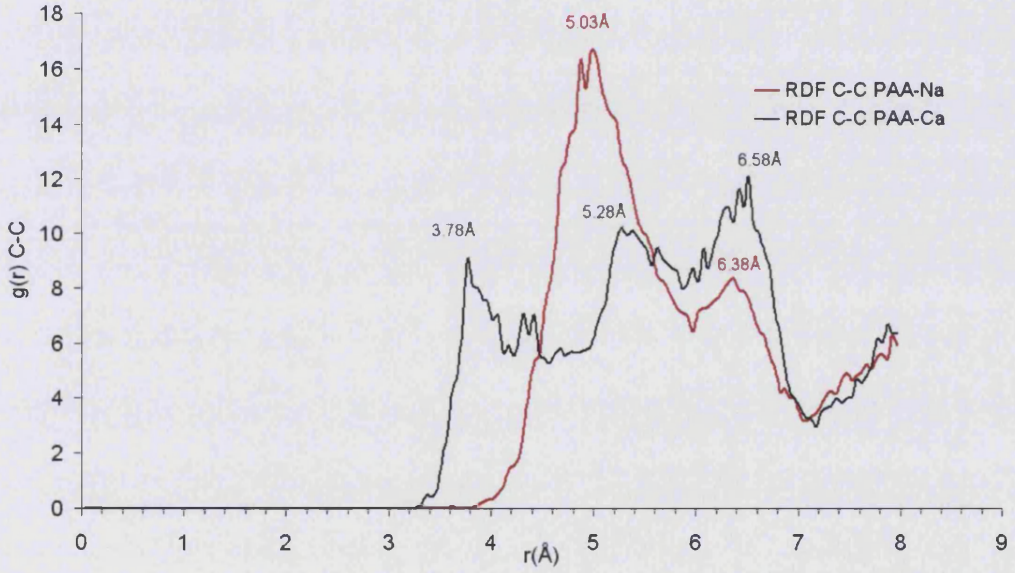

Figure 4.35: RDF for carboxylate carbon ions on PAA above a flat calcite surface (black line for the calcium salt and red line for the sodium salt)

On comparison with figure 4.30, the RDF of the two PAA salts has far less structure and, in the case of the sodium salt, has lost its first peak at 4.02Å. The RDF of the sodium salt has only two peaks at 5.03 and 6.38Å, which indicates that the introduction of the calcite surface has created a more open PAA chain. The sodium ions are still been solvated by water but there is also a surface that it can interact

with. The peaks on the calcium salt are around 0.2Å further apart than a PAA-Ca molecule in aqueous solution.

As previously noted, when the PAA molecules are fully coordinated to their cations there seems to be no adsorption on the surface. Therefore, a second set of simulations were set up with a cation from the salt starting off adsorbed onto the surface. This is effectively creating a positively charged surface and a negatively charged molecule in solution. Figures 4.36 and 4.37 show the initial configuration of the calcite surface with an adsorbed cation and the PAA molecule in solution, for the calcium and sodium salts respectively.

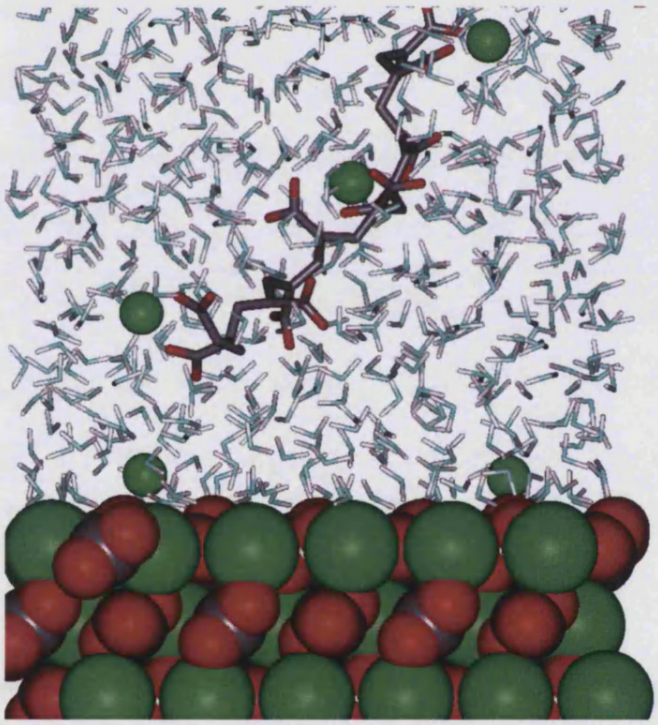

Figure 4.36: Initial configuration of a PAA-Ca molecule in solution with calcium ions adsorbed on a flat calcite surface

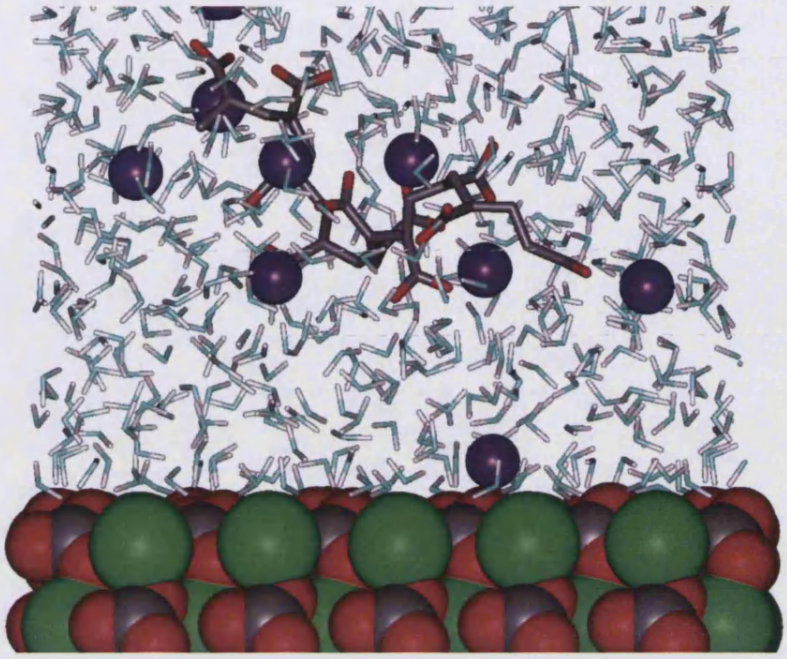

Figure 4.37: Initial configuration of a PAA-Na molecule in solution with sodium ions adsorbed on a flat calcite surface

Figures 4.38 and 4.39 show the final configurations after a 600ps MD simulation of the calcite surfaces with cations adsorbed on the surface for the calcium and sodium salts, respectively.

Figure 4.38 shows that one of the calcium ions stays adsorbed onto the surface and that the PAA-Ca salt is attracted to the ion and adsorbs onto the surface. However, the easily solvated sodium ions, in figure 4.39, do not stay adsorbed onto the surface. Therefore no adsorption of PAA-Na occurs.

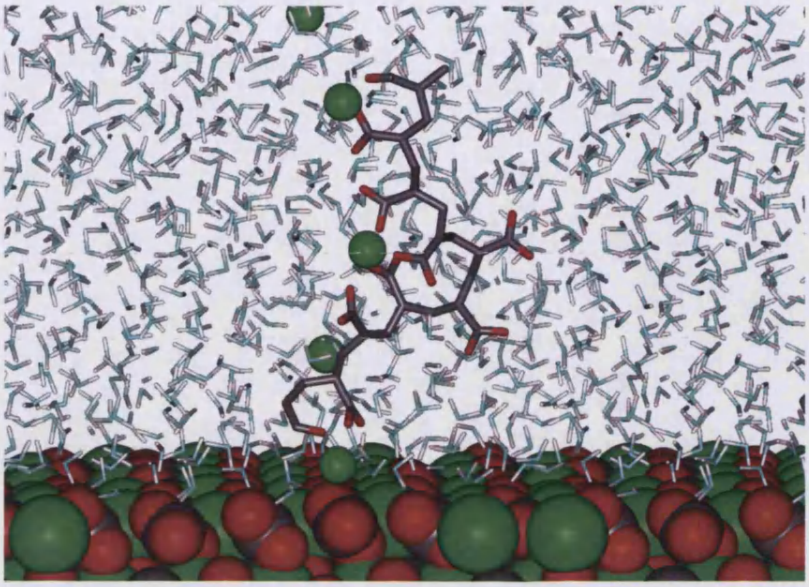

Figure 4.38: Final configuration of a PAA-Ca molecule in solution with calcium ions adsorbed on a flat calcite surface

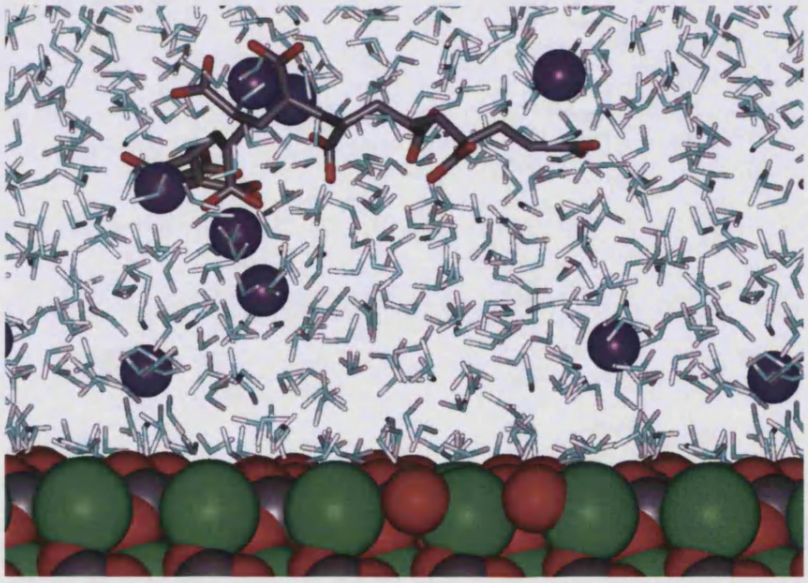

Figure 4.39: Final configuration of a PAA-Na molecule in solution with sodium ions adsorbed on a flat calcite surface

A comparison of the RDF of the carbon of the carboxylate groups on the PAA molecules (figure 4.40) reveals that the adsorbed PAA-Ca molecule has again three distinct peaks, 3.68Å, 4.88Å and 6.53Å.

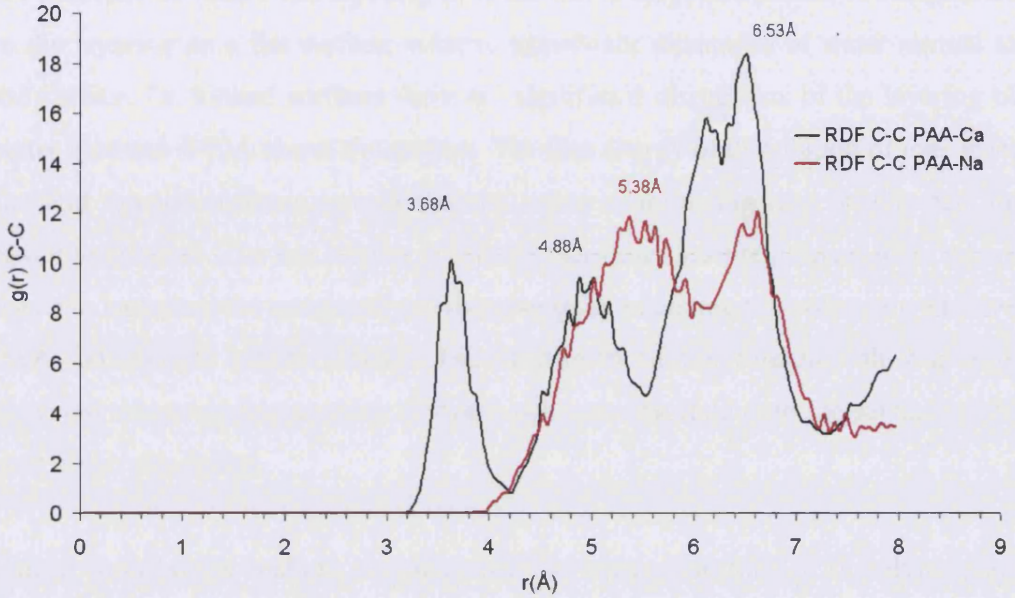

Figure 4.40: RDF for the carboxylate carbon ions on PAA above a flat calcite surface where the surface is an opposite charge to the polymeric additive (black line for the calcium salt and red line for the sodium salt)

The separations of these three peaks are closer together than the three peaks of the fully dissolved PAA-Ca molecule. Interestingly, the PAA-Ca molecule does not adsorb flat onto the surface. Further investigations are needed to follow, in order to examine the most stable adsorption sites on a calcite surface.

The interfacial energy of the crystal/water and crystal/water/PAA-Ca interface can be obtained by using equations 4.3 and 4.4. The crystal water interfacial energy for the $\{10\bar{1}4\}$ flat surface is calculated to be $0.02 J/m^2$. This value is lower than previous energy sited in the literature [155]. The interfacial energy for the system with an absorbed PAA-Ca molecule on it is calculated to be $0.11 J/m^2$. This increase in energy may be reduced if the polymeric additive is to adopt a different adsorption position, however further investigations must be completed before this can proved.

This chapter has examined the structure and stability of different calcite surfaces in the presence of water. The layering of water above stepped surfaces is comparable to the layering on a flat surface, with no significant disruption of water normal to the surface. On kinked surfaces there are significant disruptions of the layering of water between 4-10Å above the surface. The free energy of dissolution of ions from flat and stepped surfaces reveals that the lower coordinating ions on the step are easier to dissolve. The last section in this chapter describes preliminary work where we have increased the complexity of the system by including the polymeric additive, PAA, on the flat calcite surface. The adsorption of the calcium salt was only observed when a calcium cation from the salt was adsorbed onto the surface at the start of the simulation.

Future work would include obtaining the free energy profiles of dissolving ions from kinked surfaces to fully understand the effect of water structure on the stability of surfaces. Also the free energy profile of adsorbing polymeric additives onto calcite surfaces would give an estimate of the effect of the structure of water on the adsorption of molecules.

The next chapter discusses the structure and stability of minerals with a finite surface and dimensions in the nanoscale.

Chapter 5

Structure and Stability of Mineral Nanoparticles and their Interaction with Water

The work presented so far in this thesis has dealt with the structure and stability of aqueous solutions on calcite surfaces. These calcite surfaces are periodic in 2-dimensions and effectively have an infinite surface area. In this chapter we consider the structure and stability of two different minerals, periclase and calcite, that have a finite surface in the nanoscale. Both minerals have important catalytic [218, 219] and geological [220, 221] uses and in this chapter we investigate the structure of the aqueous solution around mineral nanoparticles.

As with the previous chapter, we use molecular dynamics simulations to investigate the structure of aqueous solutions around a nanoparticle. This chapter finishes with a study into the effect of charged nanoparticles on the distribution of ions in salt water. However, firstly we use energy minimisation to evaluate the effect of shape, size and morphology on the surface energies and surface reactivity of the mineral periclase, MgO.

5.1 Magnesium Oxide Crystal Structure

The mineral periclase, or magnesium oxide, has a relatively simple structure. It is a face-centred-cubic with six coordinate oxygens and cations. Magnesium oxide has the space group Fm3m and a=b=c= 4.198 Å. Since it is cubic all angles are at 90°. All simulations presented in this chapter use the Lewis and Catlow magnesium-oxygen potential [121] and this potential has been shown to reproduce crystallographic and experimental data [173]. Table 5.1 shows the atomic coordinates derived by x-ray diffraction methods.

Table 5.1: Atomic coordinates from x-ray diffraction experiments [222]

Atom	Site	Charge	x/a	y/b	z/c
Mg	4a	+2	0	0	0
O	4b	-2	0.5	0.5	0.5

5.2 Magnesium Oxide Surface Energy

The method of generating nanoparticles has been described in a previous chapter using the Wulff construction to obtain 3-dimensional polar plots. The morphologies of MgO expressing {100}, {110} and {111} surfaces are shown in figure 5.1.

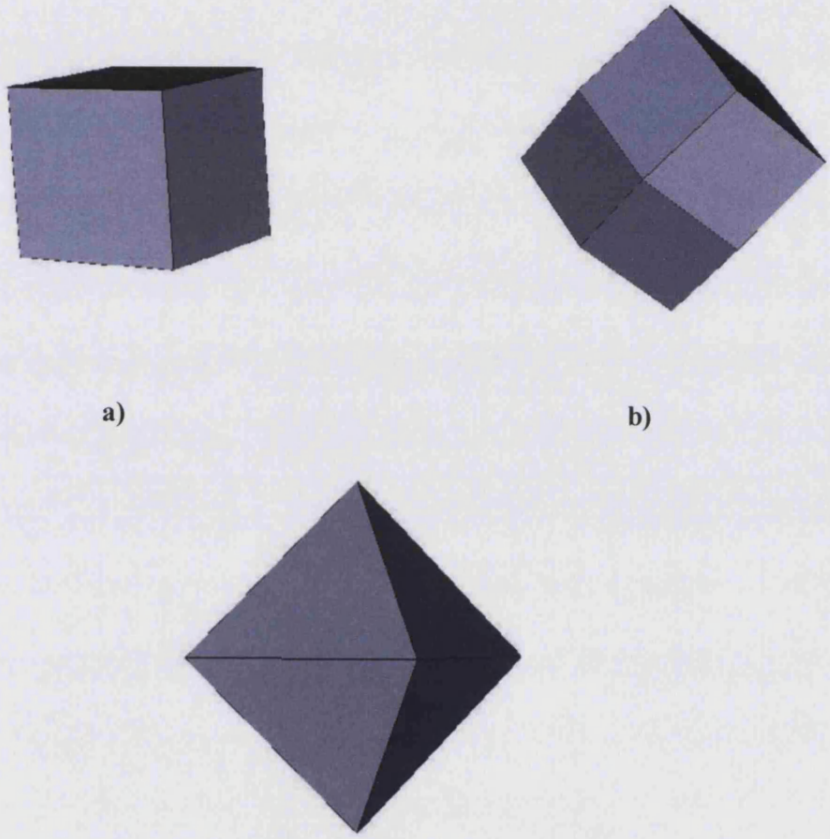

Figure 5.1: Morphology of MgO showing a) {100}, b) {110} and c) {111} surfaces

The most stable surface is the {100} surface [148]. In order to test convergence, the surface energies of MgO nanoparticles were calculated as a function of size using

METADISE. The surface energy of the nanoparticles used is the molecular surface area, with a probe size of 2.2Å, and energy minimisation technique used is the BFGS (Broydon [223], Fletcher [171], Goldfarb [224] and Shanno [225]) iterative gradient method. All nanoparticles are simulated using no periodic boundary conditions. Figure 5.2 shows that for the {100} cubic MgO nanoparticle as the size increases from 1.01nm through to 5.28nm the surface energy converges to a value of 1.43J/m^2. However, for the least stable {111} morphology the surface energy continues to increase as a function of size.

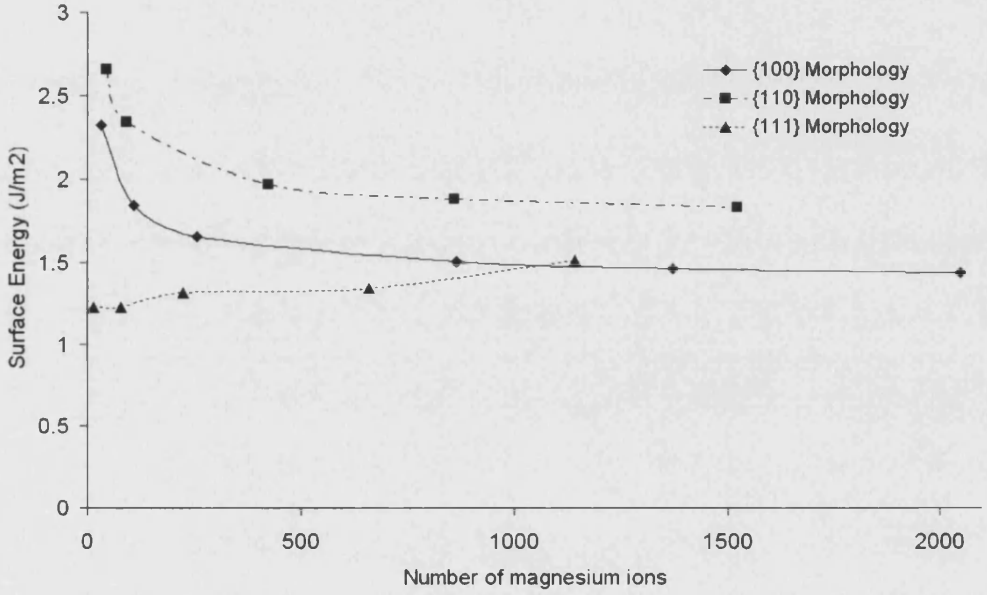

Figure 5.2: Surface energy as a function of size of low index surfaces of MgO nanoparticles

Since the energy is converging for increasingly sized {100} nanoparticles we can be confident to look at the reactivity at different positions on the surface.

5.3 Surface Reactivity of MgO Nanoparticles

In water, the surface of magnesium oxide is very likely to dissociatively adsorb water to form a hydroxylated surface [2, 226]. We can use both energy minimisation calculations and thermodynamic data to estimate the free energy of dissociatively adsorbing water. The full reaction of the whole particle would result in the conversion of periclase, an oxide, to brucite, a hydroxide.

$$2MgO_{(s)} + 2H^{+}_{(aq)} \rightarrow Mg(OH)_{2(s)} + Mg^{2+}_{(aq)} \qquad (5.1)$$

Table 5.2: Thermodynamic data at 298.15K [227]

Substance	$\Delta H_f^{\ominus}$ kJ/mol	$\Delta G_f^{\ominus}$ kJ/mol
$MgO_{(s)}$	-601.7	-569.4
$H^{+}_{(aq)}$	0	0
$Mg(OH)_{2\,(s)}$	-924.5	-833.6
$Mg^{2+}_{(aq)}$	-466.85	-454.8

The free energy of this process for nanoparticles can be estimated using energy minimisation because the thermal effects of free energy, including entropy, are likely to be small for the solid, thus the energy will be sufficient for that component. The entropic contribution for the aqueous component can be calculated from thermodynamic data. So the change in enthalpy of the system is in effect the free energy change. By using the data in table 5.2, we can calculate the free energy change of hydrating oxygen in different positions on the 5.28nm diameter MgO nanoparticle. Therefore, we can predict the most likely position that the dissociative adsorption of water would occur. Three starting positions were chosen on the surface; the corner, edge and side of the nanoparticle. Figure 5.3 shows the MgO

nanoparticle having been dissociatively adsorbed water in these three different positions.

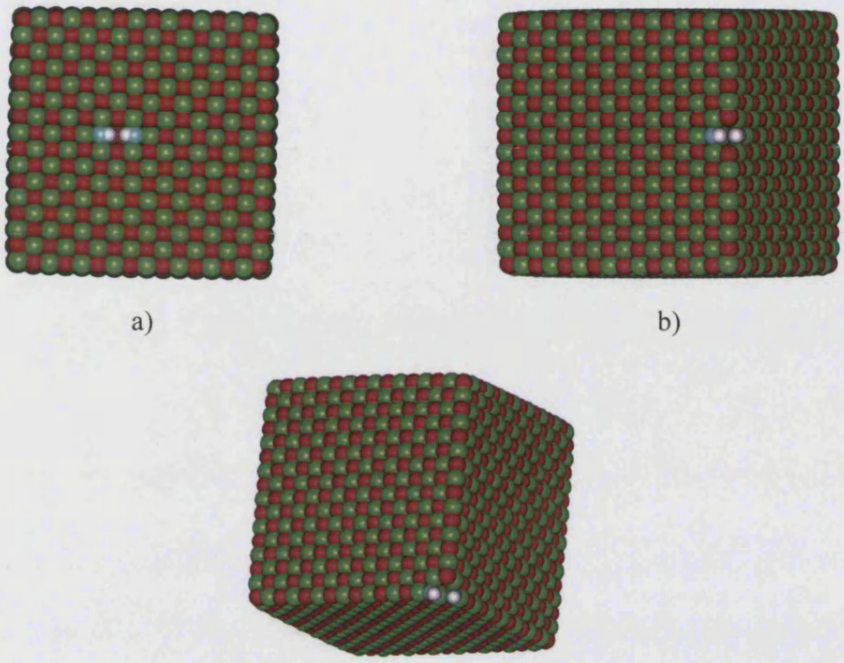

Figure 5.3: Dissociatively adsorbing water at the MgO nanoparticle surface in three different positions: a) Side, b) Edge and c) Corner

Table 5.3 shows clearly that the most stable place for the initial dissociatively adsorbed water on an MgO nanoparticle surface is at the corner.

Table 5.3: Free energy change of dissociatively adsorbing water at different positions on the surface of a 5.28nm diameter nanoparticle

Position of dissociatively adsorbing water	ΔG_f^{Θ} (H^+) kJ/mol
Side	-75.89
Edge	-244.84
Corner	-368.70

These calculations were then used to predict the mechanism of hydration on a MgO nanoparticle surface. For example, by identifying the most favourable change in free energy as we adsorb water onto the nanoparticle surface we can predict whether the adsorption will continue along the edge of the crystal, move into the side or attack another corner. Figure 5.4a shows the starting point of initial hydration. The hydration can continue either (i) at another corner (figure 5.4b), (ii) along the edge (figure 5.4c), or (iii) along the side (figure 5.4d). Table 5.4 shows the free energy change and one can compare the effect of this second adsorption. From these results, it is clear that adsorption would initially take place at the corners and then work its way along the edges of the crystal. Only after that is complete would adsorption of water continue along the side of the surface.

Table 5.4: Free energy change of two dissociatively adsorbing water molecules in different positions on a MgO nanoparticle surface

Position	ΔG_f^{Θ} (H^+) kJ/mol
Corner	-368.70
2 Corners (i)	-259.14
Corner and edge (ii)	-258.60
Corner and side (iii)	-204.12

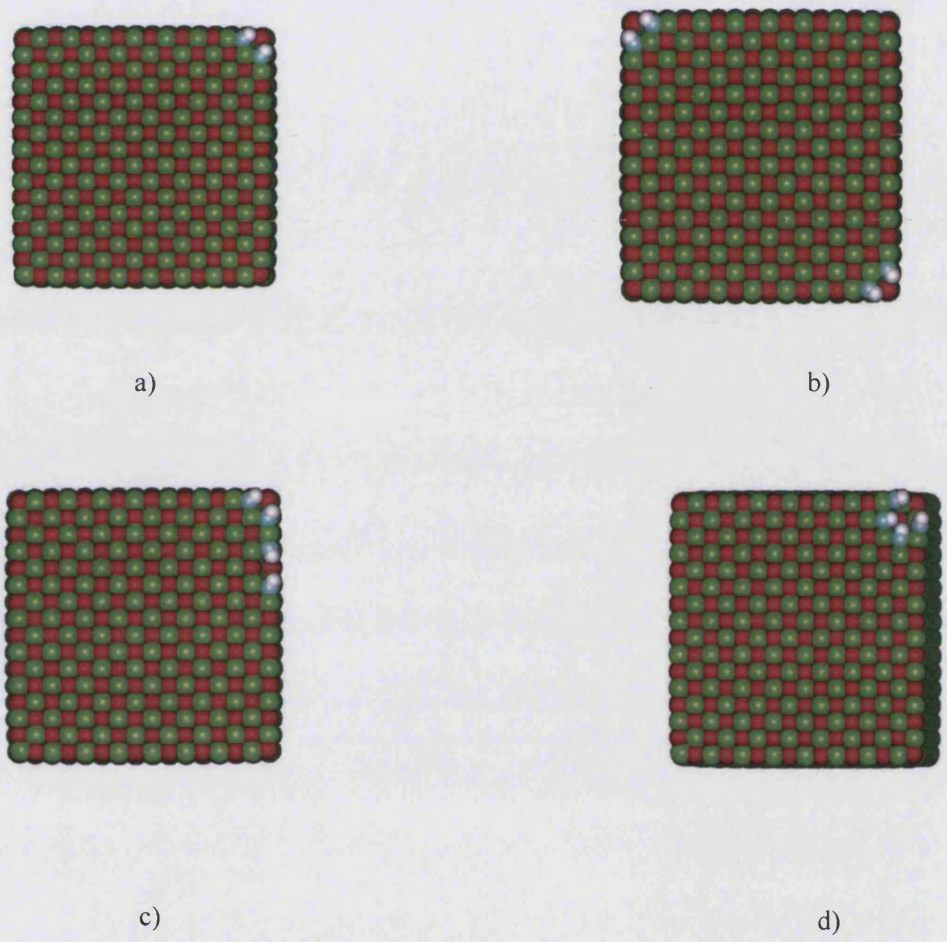

Figure 5.4: Dissociatively adsorbed water at a) the corner, b) two corners, c) the corner and continuing along the edge, d) the corner and continuing along the side

In summary, the simulations demonstrate that the most reactive part of a nanoparticle is the lower coordinated corner site. These calculations are still highly idealised, ignoring both molecular motions in the solid and the effect of introducing significant amounts of water. This next section studies the structure and dynamics of a single MgO nanoparticle in water.

5.4 MgO Nanoparticle in Pure Water

A 1.7nm MgO nanoparticle was submerged in a water box containing 2613 water molecules. The cubic simulation cell had a side length of 39.5Å on average and contained 10764 species. The MgO nanoparticle was held fixed in the centre of the simulation cell. The simulation was run for 600ps using an NPT ensemble, employing the Nose-Hoover thermostat and Hoover barostat with a relaxation time parameter of 0.5ps. The simulation was performed at a temperature of 300K and ambient pressure. The water potential parameters are that of Kerisit and Parker [68], and those used for the magnesium oxide-water interactions are that of de Leeuw and Parker [65]. Figure 5.5 shows the starting configuration of the MD simulation.

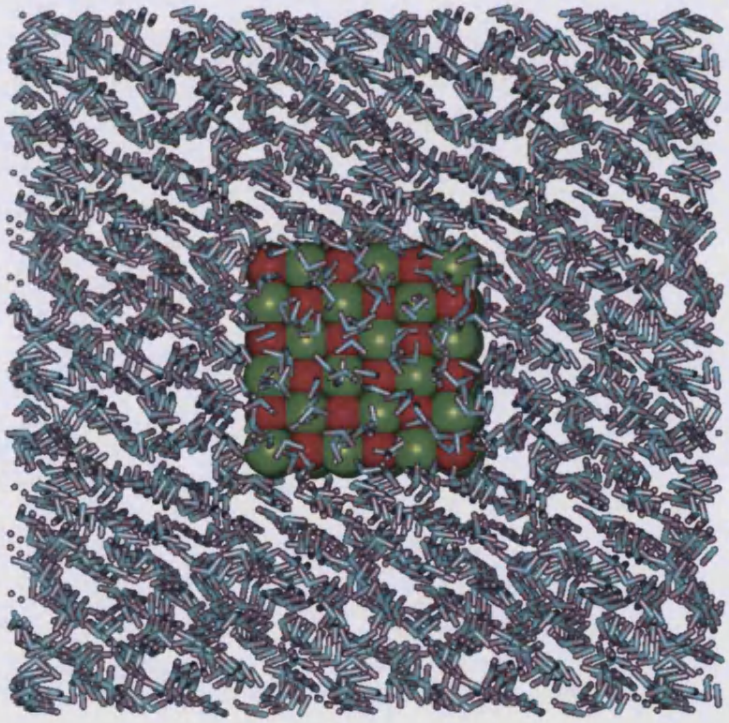

Figure 5.5: Starting configuration of a single MgO nanoparticle in water

The nanoparticle was fixed in position, and prevented from rotation by holding the central four cations fixed. We then investigated the structure of water around the nanoparticle. However, before considering the structure of water around the MgO nanoparticle we need to ensure that the system has run long enough so that it is in equilibrium. Figure 5.6 shows the potential energy of the molecular dynamics simulation as a function of time.

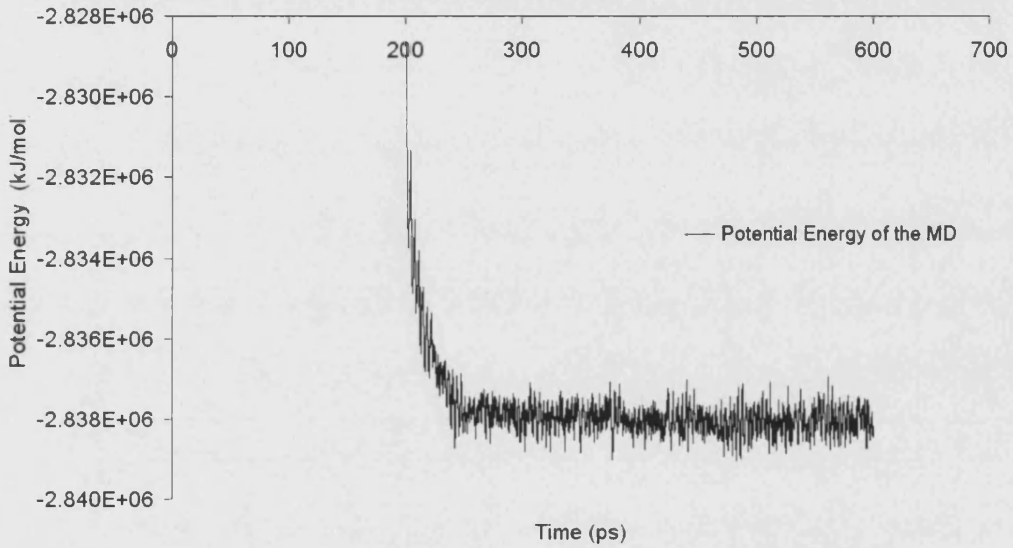

Figure 5.6: Potential energy as a function of MD time of an MgO nanoparticle in water

Figure 5.6 shows that the potential energy converges at around 250ps and therefore can be confident that the system has reached equilibrium. In Chapter 4 the structure of water above a surface was shown by splitting the simulation cell into a number of 0.3Å bins and then summing the number of times a water molecule passes into that bin. Therefore, a 3-dimensional projection of the water structure can be shown from the MD simulation. The same technique was applied to the magnesium oxide nanoparticle in water. Figure 5.7 shows the 3-dimensional projection of the structure of water around an MgO nanoparticle. The colour blue indicates a

magnesium ion density and pink through to dark red indicates water density. To aid in the visualisation of the water structure the picture is showing half the nanoparticle cut through the x-axis. Figure 5.7 shows a highly ordered structure of water around the nanoparticle with at least four distinct layers of water above the surface, which corresponds to ordering up to 8-10Å above the surface. The distance between the surface of the nanoparticle and the first layer of water corresponds to about 2.5Å. The slight smearing of blue around the magnesium ions is due to the vibrations around their lattice sites.

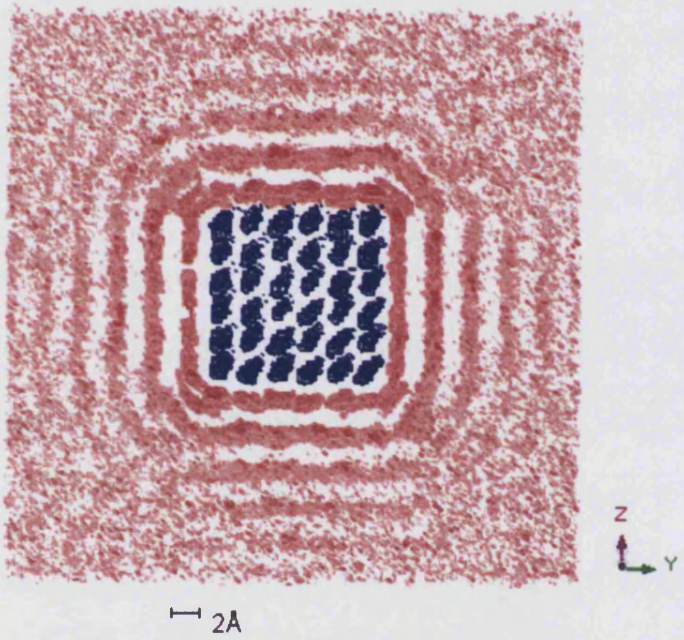

Figure 5.7: 3-dimensional projection of the structure of water around a 1.7nm MgO nanoparticle. The colour blue indicates a magnesium ion. Pink indicates a lower number of water molecules, whereas dark red indicates a high number of water molecules.

The water structure above sides of the nanoparticle mimics the flat surfaces. However, around the corners and edges of the nanoparticle there is significant disruption of the distribution of the water density. Figure 5.7 shows an interstitial position of water in-between the first two layers at the corner and edge sites. Above

the second layer of water the layering is not as apparent as above the flat surfaces. The difference in water density could be highly significant for the rates of growth and dissolution. The fluctuations in water density is likely to slow the transport of ions and molecules to flat surfaces, but the fluctuations are absent from edges and corners. A possible way of distinguishing different sites in the nanoparticle-water system is to compare the residence time of a water molecule in the first hydration layer. By defining the surface of the nanoparticle in terms of whether a magnesium ion is on the side, edge or corner of the nanoparticle, it can give an indication of the dynamics of water at each position. Table 5.5 shows the average residence time and average coordination number at the side, edge and corner of the MgO nanoparticle.

Table 5.5: Water residence time at the nanoparticle surface and magnesium coordination number

Magnesium Position	Average Water Residence Time/ps	Average Coordination Number to MgO Oxygen	Average Coordination Number to Water Oxygen
Side	180.8 ± 36.83	5.0	1.7
Edge	126.4 ± 32.49	4.0	2.8
Corner	126.5 ± 47.51	3.1	4.0

Table 5.5 shows that the average coordination number follows the expected trend. The residence times around the corners and the edge are less than the residence time around the flat side magnesium ions. Interestingly, the residence times at the edge and corner are similar. The total coordination number for magnesium at the side edge and corner is 6.7, 6.8 and 7.1 respectively. The coordination number of magnesium in bulk MgO is 6. The reasoning behind the high coordination number at these sites could be that the effective size of the magnesium is larger. Also the increasing coordination number suggests that the water molecules are spending less time on average at these sites.

There is no structural change of this highly ionic nanoparticle in the presence of water compared with the simulation run at vacuum. However there have been experimental [97] and computational evidence [98] that water around a nanoparticle can stabilise its structure. Therefore in this next section we consider a nanoparticle with a different composition (calcite) in water to see if any of the structural effects are observed.

5.5 Calcite Nanoparticle in Pure Water

A 1.5nm calcite nanoparticle was immersed in water and a molecular dynamics simulation was performed in the NPT ensemble at 300K and zero pressure. The cubic simulation cell had a side length of 36.5Å on average and contained just under 2000 water molecules. The simulation was run for 400ps with a time step of 0.1fs. The stable $\{10\bar{1}4\}$ surface was used to create its rhombohedral morphology. The calcium-carbonate oxygen RDF from this simulation is shown in figure 5.8a. For comparison, the calcium-carbonate oxygen RDF obtained from the simulation of bulk calcite is given in figure 5.8b. Figure 5.8a shows a loss in crystalline structure compared to the bulk crystal. Indeed, the peaks in the RDF of the nanoparticle are not as clearly defined as in the bulk RDF. However, their position changes by 0.05Å at most and thus remains almost the same.

In order to consider the effect of the water on the crystalline structure of the nanoparticle, the same particle was modelled in vacuum. The calcium-carbonate oxygen RDF $g(r_{Ca\text{-}O})$ of the nanoparticle in a vacuum is shown in figure 5.8c. The nearest neighbour $r_{Ca\text{-}O}$ is the same distance, 2.33Å; however, the next three peaks have merged into one at 3.88Å. This suggests a change in the structure and that the nanoparticle in a vacuum is more amorphous than in water.

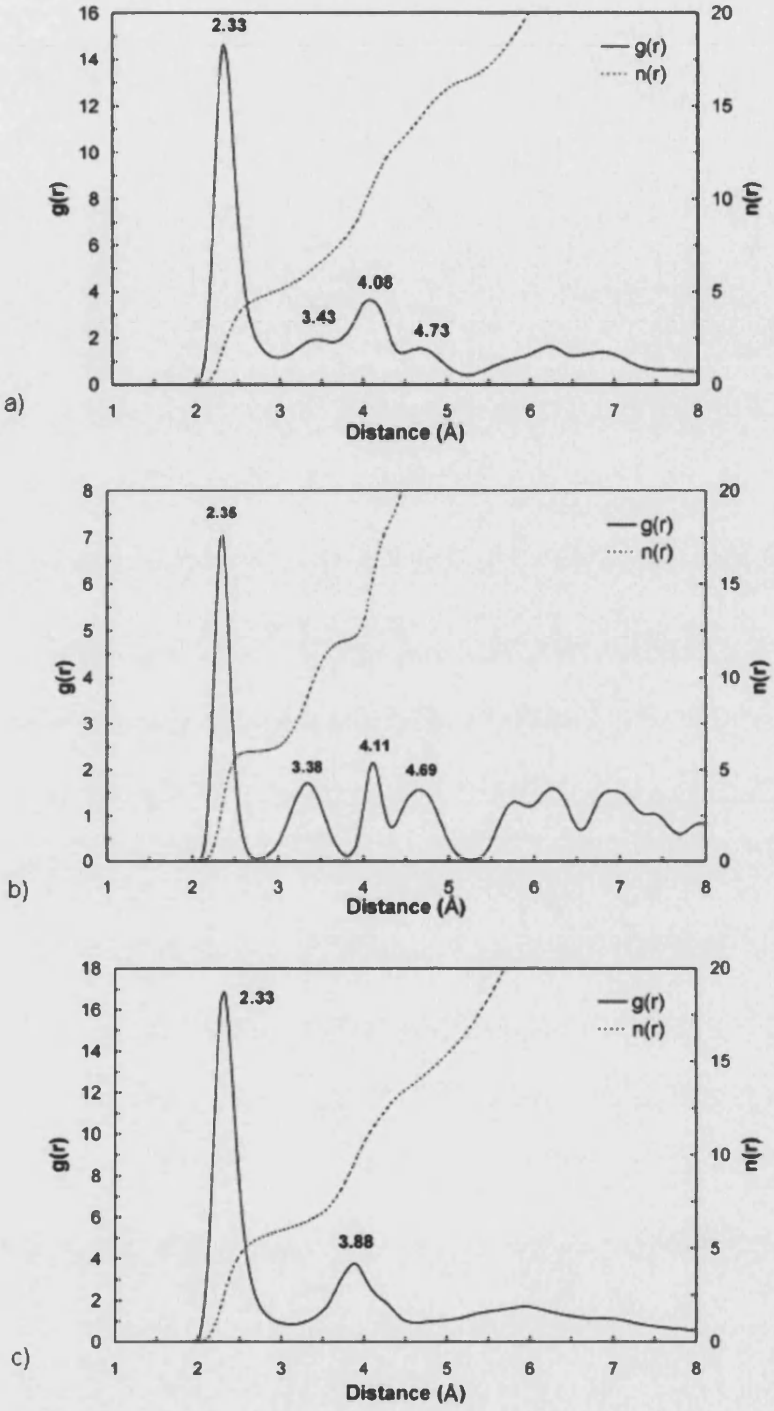

Figure 5.8: Calcium-carbonate oxygen RDF of a) nanoparticle in water, b) bulk and c) nanoparticle in vacuum

In comparison with the MgO nanoparticle, this calcite nanoparticle has far fewer atoms. Indeed there is only one calcium carbonate unit in a bulk-like position in this nanoparticle. Figure 5.9 shows the water structure surrounding the calcite nanoparticle. The picture has been cut half-way through the calcite nanoparticle along the z-axis in-order to aid in visualising the water structure.

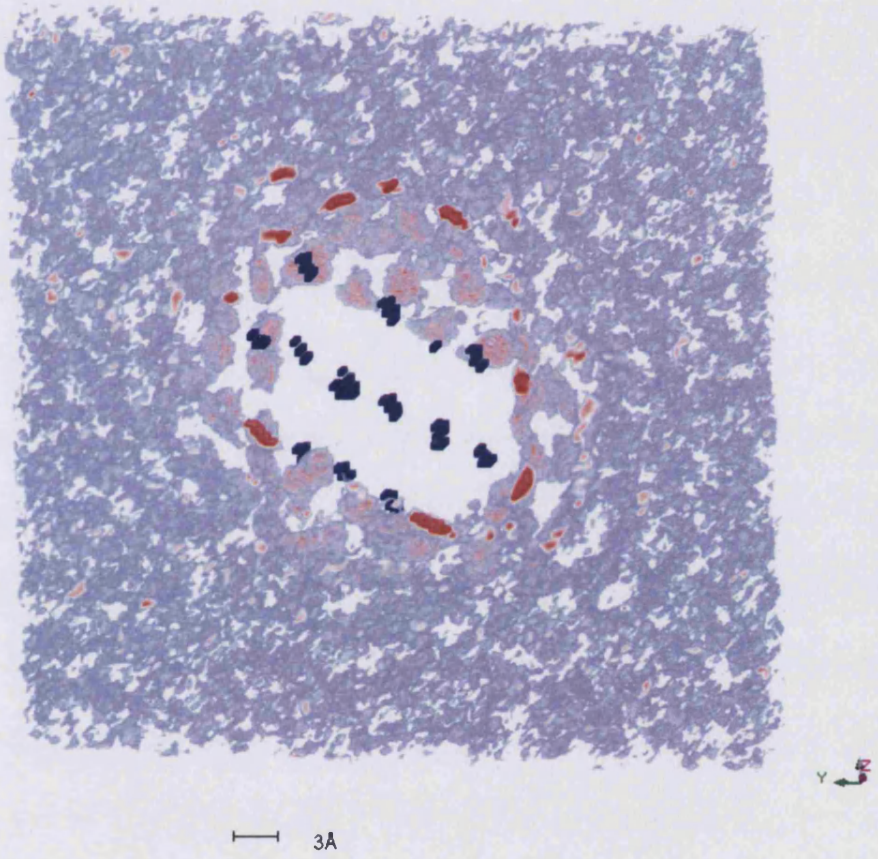

Figure 5.9: 3-dimensional projection of the structure of water around a 1.5nm calcite nanoparticle. The colour blue indicates a calcium ion. A whitish-pink colour indicates a lower number of water molecules, whereas a darker red indicates a high number of water molecules.

Figure 5.9 indicates that the layering around the calcite nanoparticle is not as profound as in the MgO nanoparticle. There is localisation of water molecules around each calcium ion but there is not the 4 layers observed in the MgO

simulation. Table 5.6 shows the average residence time of a water molecule in the first hydration shell of each type of calcium ion together with the average calcium coordination number.

Table 5.6: Water residence time at the nanoparticle surface and calcium coordination number with carbonate and water oxygen

Calcium position	Average Water Residence Time/ps	Coordination Number with Carbonate Oxygen	Average Coordination Number with Water Oxygen
Side	29.53 ± 14.03	5	1.1
Edge	33.95 ± 4.80	4	2.6
Corner	33.35 ± 5.89	3	3.6

As in the previous simulation, the change in the coordination number follows the expected trend depending on the calcium position on the nanoparticle. The water residence time only deviates a little from ion to ion and is much lower than in the first hydration layer of a flat $\{10\bar{1}4\}$ surface. This was calculated in chapter 4 to be 292ps and compared well with previous computational studies [68]. However, these residence times are very similar to that in the hydration shell of an isolated calcium ion in solution [68], which is in agreement with results from NMR studies where the residence time for an oxygen of a water molecule in the first hydration layer of a calcium ion was found to be less than 100ps [228]. Both structural and dynamical calculations suggest that the calcite nanoparticle has considerably less effect on the water structure than that of the ideal infinite surface, and surprisingly, more closely resembles that of an isolated calcium ion.

To investigate at what size a calcite nanoparticle starts to behave more like a 2-dimensional surface rather than an isolated ion in solution, further calculations with larger nanoparticles need to be performed.

A further important consideration when generating predictions for experiments is that there is no requirement for the nanoparticle in solution to be charge neutral. Indeed, there is a large body of work on colloids suggesting these charge effects are crucial (see section 1.3.4). Thus in the last section we consider the interaction of charged MgO nanoparticles with electrolyte solutions and begin to investigate the nature of the electric double layer around nanoparticles.

5.6 Charged MgO Nanoparticle in Salt Water

The charge density above flat mineral surfaces has been the subject of many computational [158, 229] and experimental studies [230]. The layering of water molecules around mineral nanoparticles immersed in pure water is evident from the previous simulations. The rest of this chapter is concerned with the effect of a mineral nanoparticle immersed in salt water. One important issue arose immediately, namely that there is not a suitable magnesium-chlorine potential in the literature. Previous atomistic studies of $MgCl_2$ had only considered the beta structure [161] and therefore, a new potential was derived that could be used for both the alpha and beta structures.

5.6.1 Magnesium Chloride

The magnesium-chlorine interaction was derived by fitting the potential to the structures of both the alpha and beta $MgCl_2$ structure using the GULP code [143]. The potential was derived from a calcium-chlorine potential [229] so that the chlorine-chlorine interaction remained unchanged. The alpha structure has a rhombohedral structure with the space group $R\bar{3}m$. The experimental unit cell parameters of the alpha structure have been derived by x-ray diffraction methods

[231] and the atomic coordinates from this is shown in table 5.7. The unit cell parameters are a=b=3.595Å and c=17.59Å with $\alpha=\beta=90^{o}$ and $\gamma=120^{o}$.

Table 5.7: Atomic coordinates from x-ray diffraction experiments for alpha $MgCl_2$ [231]

Atom	Site	Oxidation	x/a	y/b	z/c
Mg	3a	2	0	0	0
Cl	6c	-1	0	0	0.273

The beta structure also has a trigonal structure but the layering of the chlorine atoms is closer together, with the space group $P\bar{3}m1$. The experimental unit cell parameters of the beta structure have also been derived by x-ray diffraction methods [232] and the atomic coordinates from this are shown in table 5.8. The unit cell parameters are a=b=3.641Å and c=5.927Å with $\alpha=\beta=90^{o}$ and $\gamma=120^{o}$.

Table 5.8: Atomic coordinates from x-ray diffraction experiments for beta $MgCl_2$ [232]

Atom	Site	Oxidation	x/a	y/b	z/c
Mg	1a	2	0	0	0
Cl	2d	-1	0.3333	0.6667	0.23

Table 5.9 shows the comparison of the experimental unit cell parameters with the calculated unit cell parameters for both structures using the newly derived potential.

Table 5.9: Comparison of the experimental unit cell parameters for both alpha and beta $MgCl_2$ structures with calculated parameters

	Structure			
	Alpha		Beta	
Property	Expt. [231]	Calculated	Expt. [232]	Calculated
a(Å)	3.595	3.609	3.641	3.603
c(Å)	17.590	17.404	5.927	5.941
a/c	0.204	0.207	0.614	0.606
Mg-Cl distance (Å)	2.330	2.360	2.500	2.360

The magnesium-chlorine bond distance was obtained by running both structures through a MD simulation using an NPT ensemble for 1ns. A Nose-Hoover thermostat, a Hoover barostat with a relaxation time of 0.5ps and a time step of 0.2fs were used. Both structures were stable at 300K and zero applied pressure therefore, this potential was used to describe the interaction between magnesium oxide nanoparticles and salt water.

5.6.2 Magnesium Oxide Nanoparticle in Salt Water

The sodium and chlorine ions were randomly distributed in the simulation cell to make up a 0.63M salt water concentration. At pH 7, magnesium oxide would be expected to have a positive charge associated with it because its point of zero charge is at 10-12 [233-235]. Any pH that is lower than the point of zero charge will produce in a material with a net positive charge and any pH that is higher gives a negative charge. Thus a sodium ion was positioned 2.7Å from the particle to give it a +1 effective charge. The charged MgO nanoparticle in salt water was run in a 600ps MD simulation using the same conditions as in the MgO pure water simulations.

Figures 5.10, 5.12 and 5.13 show the water, sodium and chlorine structure around a positively charged MgO nanoparticle, respectively. From the figures 5.12 and 5.13, it can be seen that the simulation would need to be run longer because although the water structure is highly defined, the sodium and chlorine ions are not uniformly dispersed around the nanoparticle. However, the MD simulations do give an insight into the structure of the electrolyte solution and show an electric double layer forming.

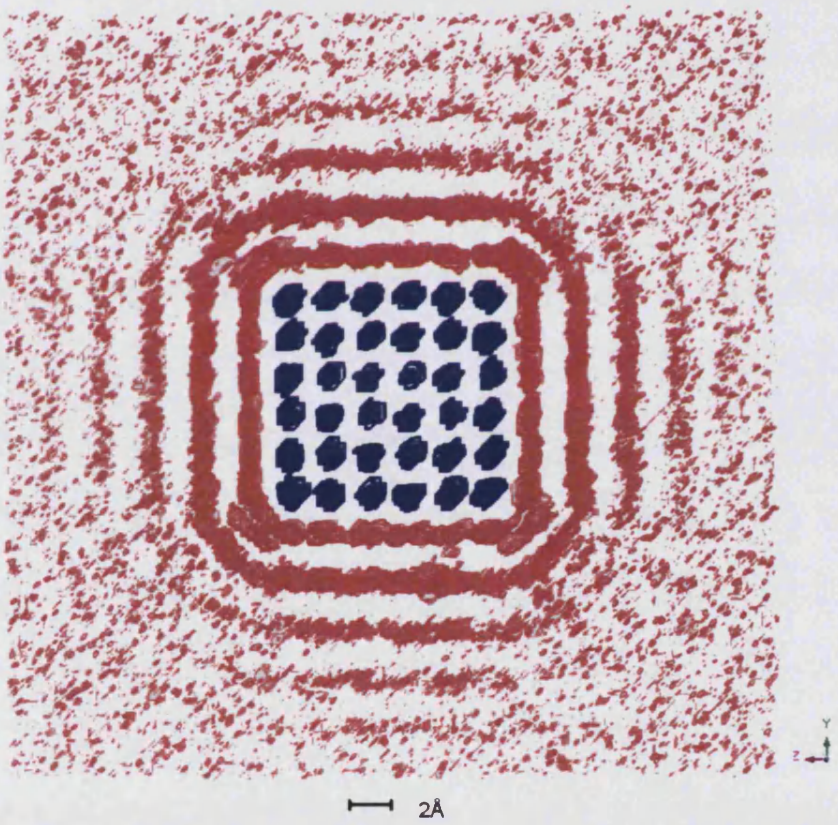

Figure 5.10: 3-dimensional projection of the structure of water around a positively charged MgO nanoparticle in a salt water solution. The colour blue indicates a magnesium ion. Light red indicates a lower number of water molecules, whereas dark red indicates a high number of water molecules.

In comparison with figure 5.7, the structure of water around a nanoparticle is not affected by the presence of salt in solution. There is still a high ordering of water along the sides of the nanoparticle, up to 8Å in height, and less ordering above the edges of the nanoparticle. By comparing the RDF plots of the magnesium ion in the nanoparticle and the oxygen of the water molecule (figure 5.11), the distance of the water molecule from the surface and the shape of the plots are identical.

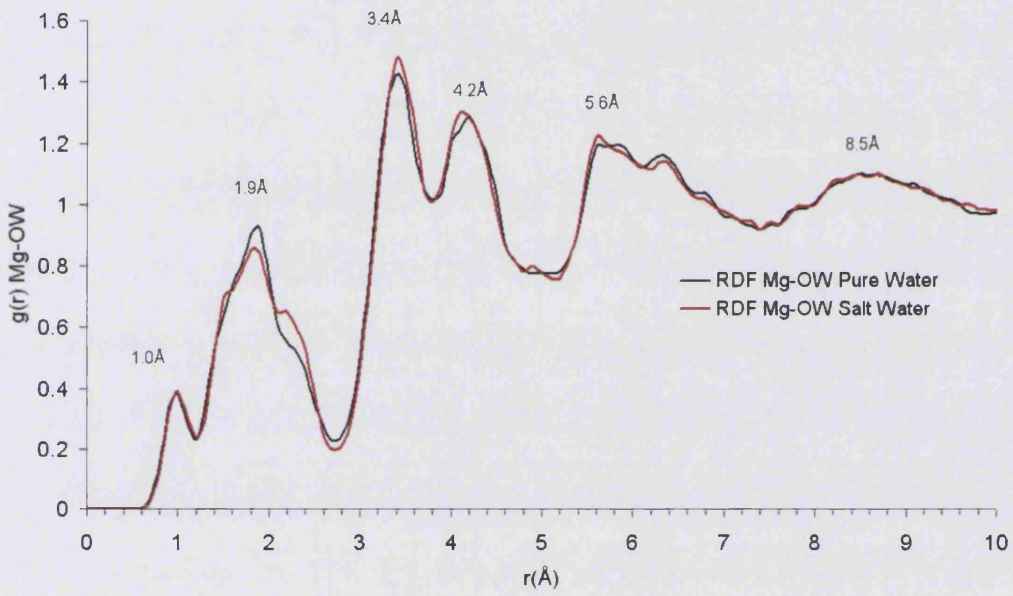

Figure 5.11: RDF of a magnesium ion in a nanoparticle and oxygen from pure and salt water

The first peak is split at a distance of 1 and 1.9Å above the surface of the nanoparticle. The splitting of the first and second peak is due to the magnesium ion not being in the centre of the nanoparticle. The structure of water is highly ordered with peaks at 3.4, 4.2, 5.6 and 8.5Å. There is no difference in the RDF of pure and salt water around a nanoparticle and therefore the introduction of salt does not seem to affect the structure of water around a nanoparticle.

Table 5.10 shows the residence times and average coordination number of magnesium ions with water. The coordination number shows the same trend as in the pure water system. The average residence times are slightly higher around the side and edge of the nanoparticle in pure water (see table 5.5). However, the average residence time is lower around the corner in the salt solution rather than the pure water system. The positive charge on the nanoparticle could cause the oxygen ions of the water molecule to spend more time in the first hydration shell of the magnesium ions.

Table 5.10: Water residence time at the nanoparticle surface and magnesium coordination number with water in a salt water solution

Magnesium position	Average Water Residence Time/ps	Average Coordination Number with MgO Oxygen	Average Coordination Number with Water Oxygen
Side	242.82 ± 61.62	5	1.7
Edge	161.89 ± 45.33	4	2.8
Corner	112.72 ± 52.34	3.1	3.9

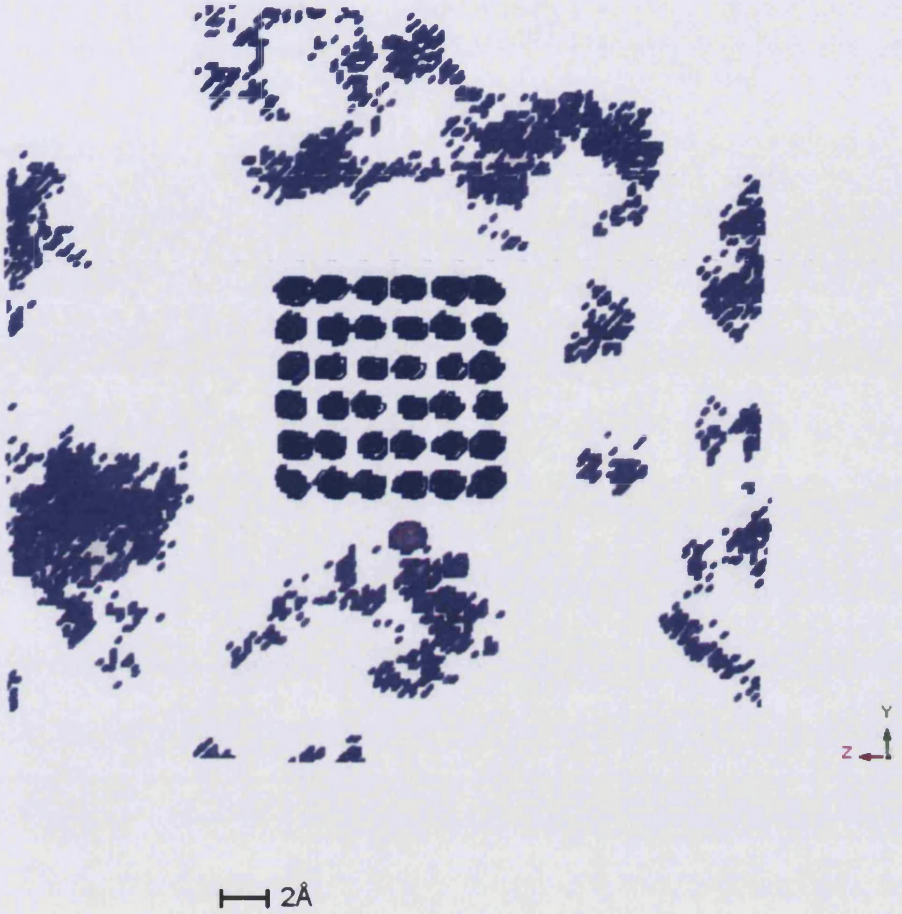

Figure 5.12: 3-dimensional projection of the sodium ion distribution around a positively charged MgO nanoparticle. Dark blue indicates a magnesium ion and a pale blue/purple indicates the sodium ion distribution.

Figure 5.12 shows the distribution of sodium around the positively charged MgO nanoparticle. The adsorbed sodium ion can be seen at the bottom of the nanoparticle. The pale blue/purple colour in figure 5.12 shows the sodium ion distribution around the MgO nanoparticle. Figure 5.13 shows the chlorine ion distribution around the MgO nanoparticle. The green/blue colour indicates the chlorine ion distribution around the blue magnesium ions.

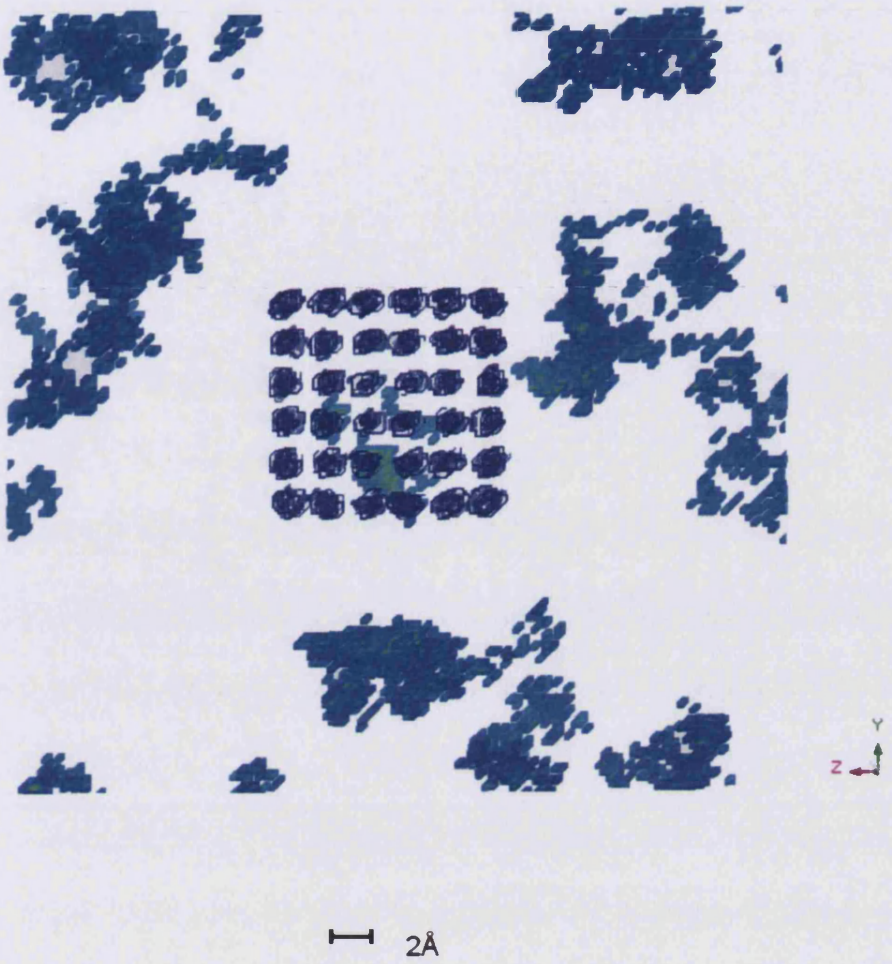

Figure 5.13: 3-dimensional projection of the chlorine ion distribution around a positively charged MgO nanoparticle. Dark blue indicates a magnesium ion and a turquoise indicates the chlorine ion distribution.

Below the nanoparticle, where the sodium ion is adsorbed, there is a high distribution of chlorine ions compared with the rest of the distribution. There is no real evidence of an electric double layer being formed in these simulations. It is clear that in both electrolyte projections the simulations need to be run for much longer as there are areas of no electrolyte ions in the simulation cell.

A second simulation was performed to increase the positive charge on the MgO nanoparticle by creating an oxygen ion vacancy on the surface. The creation of the vacancy was at the corner of the nanoparticle as this is the most reactive point (see section 5.3). The MD simulation was performed using the same conditions as before and the nanoparticle had an effective charge of +3 on the nanoparticle. To compensate this extra positive charge two more chlorine ions were randomly added to the solution to keep the charge of the entire system neutral. Figure 5.14 shows the distribution of sodium ions around an MgO nanoparticle that has an effective charge of +3. Again, there is not a great deal of ordering of sodium ions around the nanoparticle.

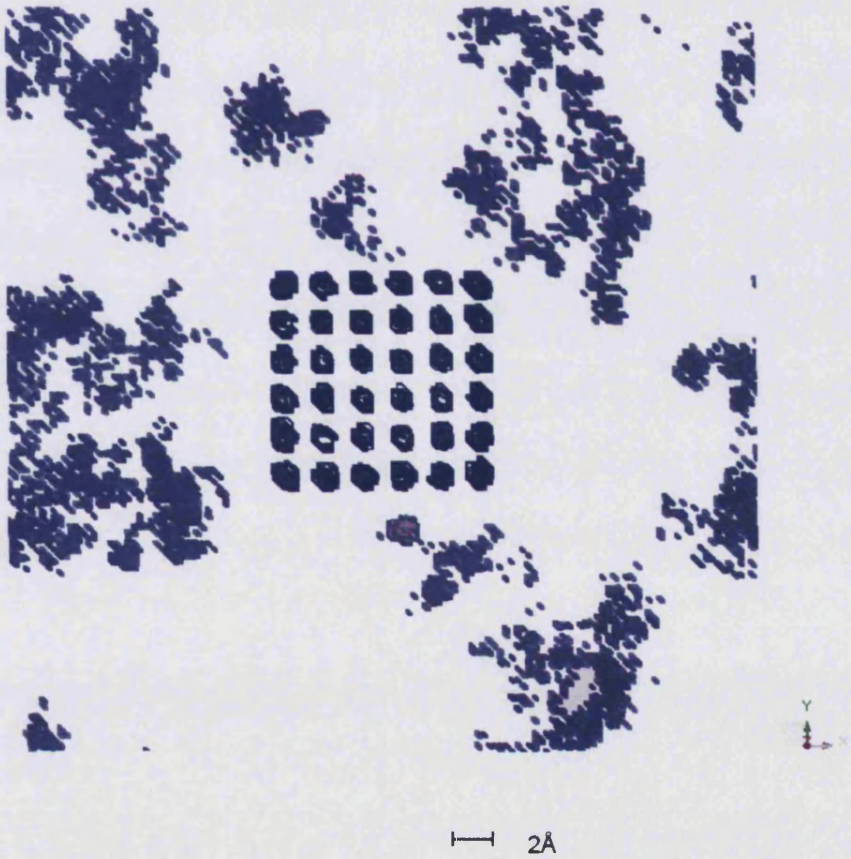

Figure 5.14: 3-dimensional projection of the sodium ion distribution around a +3 charged MgO nanoparticle. Dark blue indicates a magnesium ion and a pale blue/purple indicates the sodium ion distribution.

Figure 5.15 shows the distribution of chlorine ions around a +3 charged MgO nanoparticle. The chlorine ion distribution around a +3 MgO nanoparticle shows increased ordering towards the left and bottom of the nanoparticle.

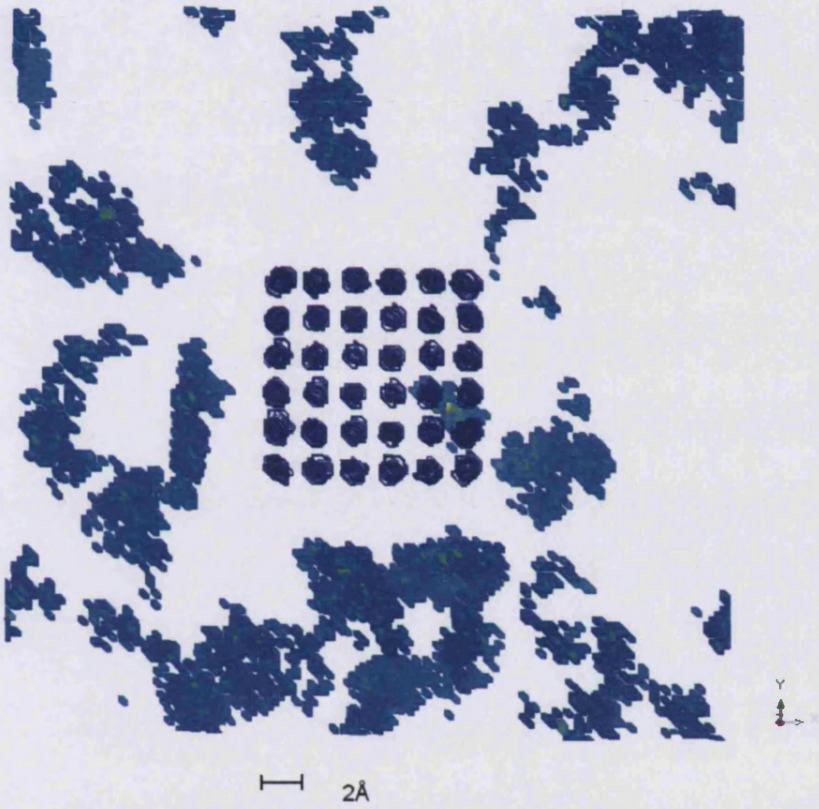

Figure 5.15: 3-dimensional projection of the chlorine ion distribution around a +3 charged MgO nanoparticle. Dark blue indicates a magnesium ion and a turquoise colour indicates the chlorine ion distribution.

To illustrate the effect of the increased positive charge of the nanoparticle on the negative chlorine ion, we can compare the RDF of a magnesium ion with the chlorine ions in solution. Figure 5.16 shows the RDF of a magnesium ion from a +1 charged nanoparticle with chlorine ions and figure 5.17 shows the RDF of a magnesium ion from a +3 charged nanoparticle with chlorine ions.

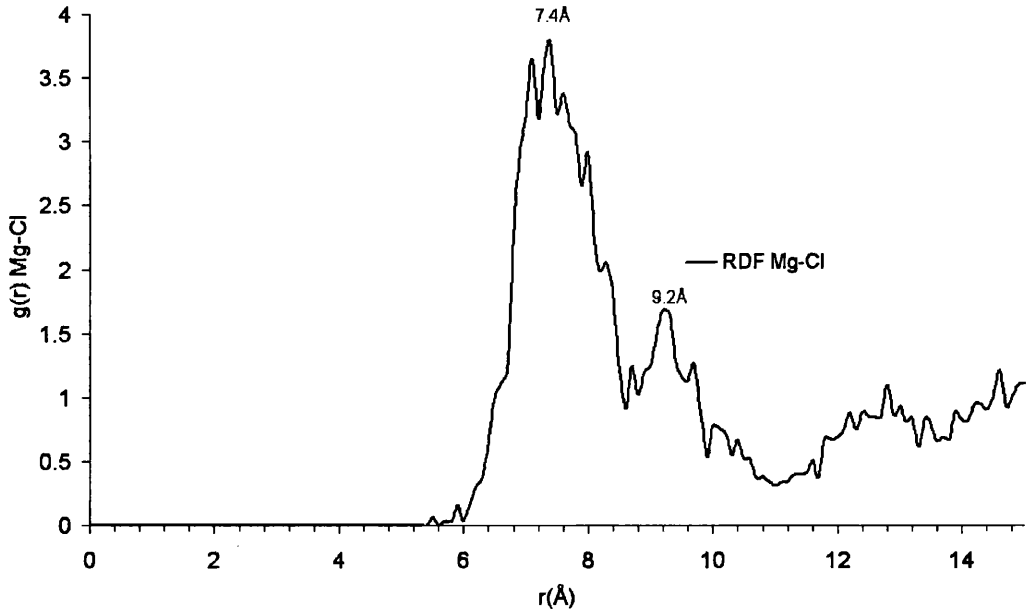

Figure 5.16: RDF of a magnesium ion from a +1 charged nanoparticle with chlorine ions in solution

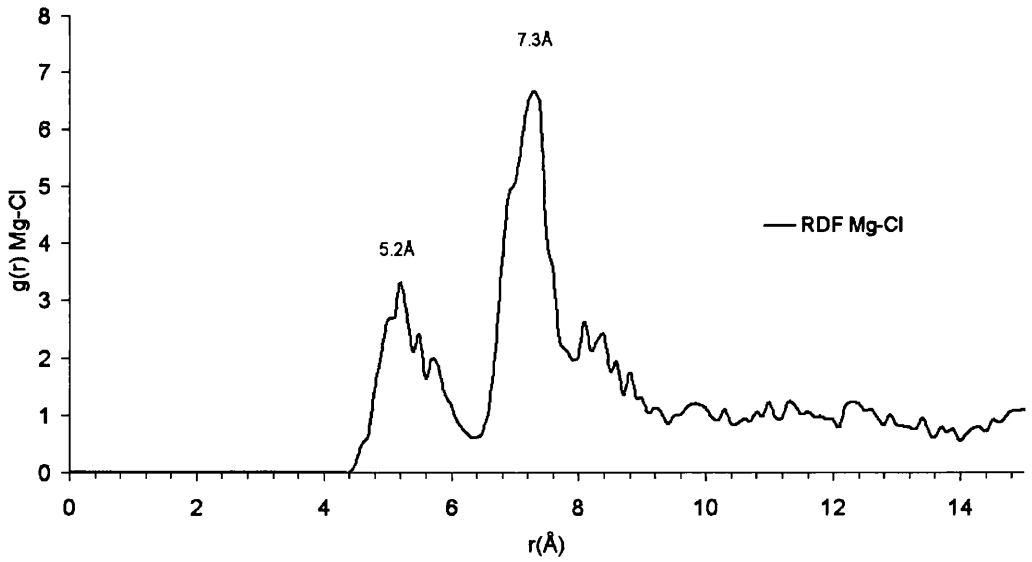

Figure 5.17: RDF of a magnesium ion from a +3 charged nanoparticle with chlorine ions in solution

Figure 5.16 reveals a strong peak of chlorine ions at 7.4Å above the flat surface and a secondary smaller peak at 9.2Å. By increasing the charge to +3 on the nanoparticle causes a peak to be observed closer to the flat surface at 5.2Å and again at 7.3Å (figure 5.17).

A third simulation was also performed but this included a magnesium ion vacancy rather than an oxygen ion vacancy. Also in order to increase the effective negative charge on the nanoparticles the sodium ion previously adsorbed on the surface was placed back into solution. Therefore, the effective charge on the nanoparticle was -2. To compensate, two sodium ions were added to the solution so that the charge of the system was maintained as neutral. The sodium ions are strongly attracted to the negative MgO nanoparticle and one was quickly adsorbed onto the flat surface. The sodium ion adsorption is also clearly shown in the 3-dimensional projections of the distribution around the MgO nanoparticle (figure 5.18).

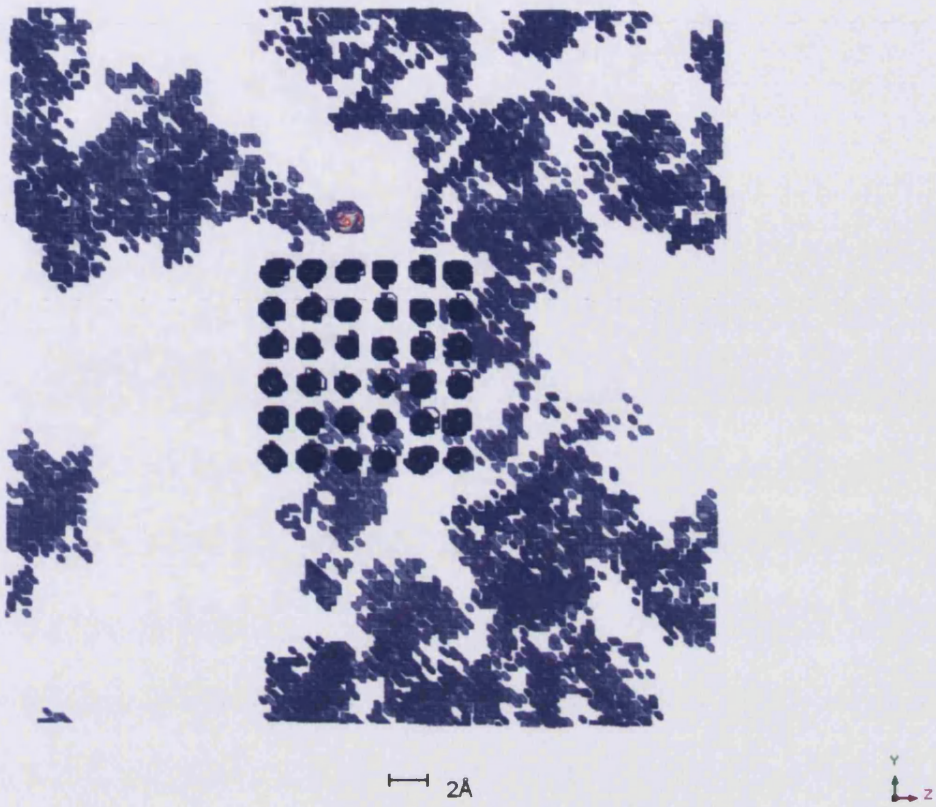

Figure 5.18: 3-dimensional projection of the sodium ion distribution around a -2 charged MgO nanoparticle. Dark blue indicates a magnesium ion and a pale blue/purple indicates the sodium ion distribution.

The adsorption of a sodium ion is clearly shown to be adsorbed on to the top of side of the nanoparticle. Analysis of the RDF of a magnesium ion in the nanoparticle with the sodium ions in solution reveals that the absorbed sodium ion is 2.71Å above the surface (figure 5.19). Despite the intensity of this peak there is no real structure to the remaining part of the RDF plot in figure 5.19.

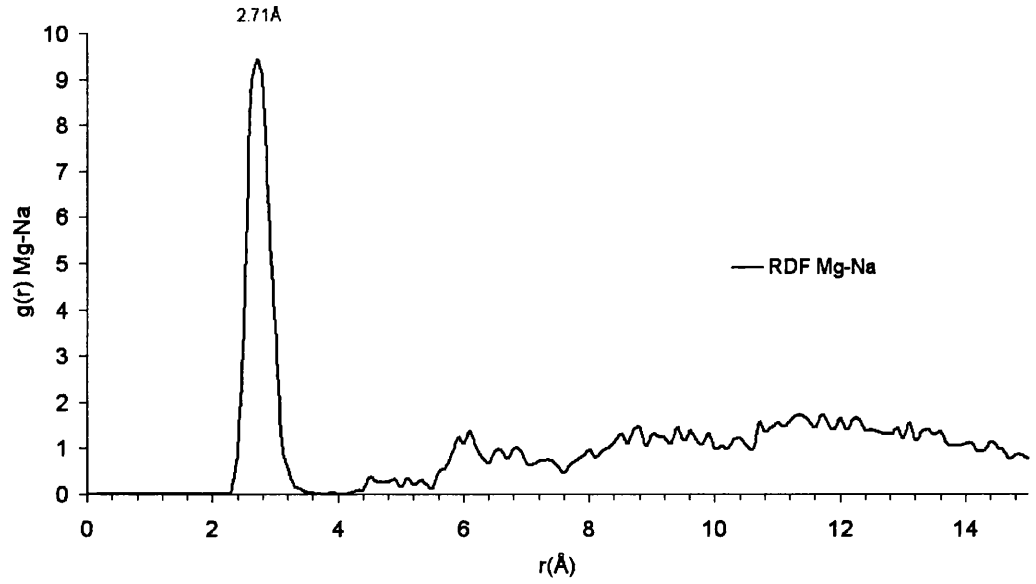

Figure 5.19: RDF of a magnesium ion from a -2 charged nanoparticle with sodium ions in solution

The fact that the sodium ion chose to adsorb onto the side and not where the vacancy was situated initially implies that the effective charge is distributed around the whole of the nanoparticle and not just at the vacancy. However, closer analysis of the vacancy region shows that there may not have been the room for a sodium ion to adsorb at the vacancy position. Figure 5.20 shows a close-up of the final configuration of the vacancy region of the nanoparticle.

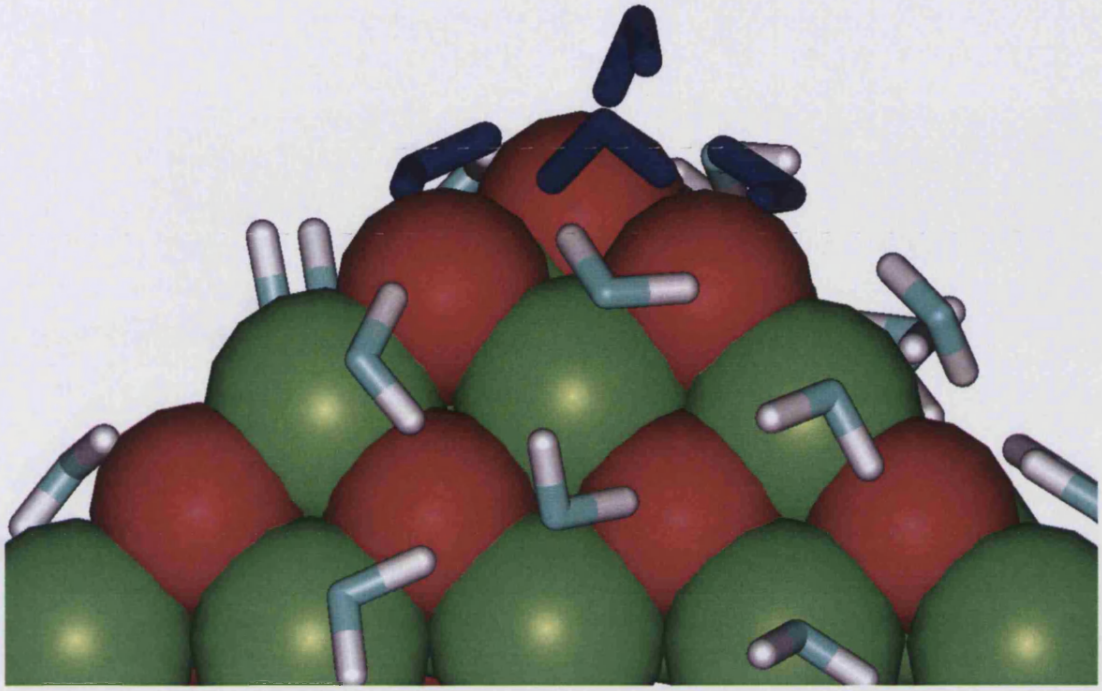

Figure 5.20: A close-up of the final configuration of the vacancy region of the nanoparticle.

Figure 5.20 shows closest water molecules, coloured dark blue for clarity, all pointing their hydrogen atoms into the vacancy. The distances between the oxygen ions of the nanoparticle and the hydrogen atoms of the water molecules are in the region of 1.5-1.8Å. This suggests that there would be a kinetic energy barrier to overcome. Analysis of the residence times of the hydrogen of the water molecule and the oxygen of the MgO nanoparticle around the vacancy is calculated to be 231.85 ± 7.04ps.

In this chapter we have shown how the reactivity of nanoparticles can be analysed in two different ways. Firstly, energy minimisation techniques can be used to calculate the free energy of hydration at different positions on the MgO {100} nanoparticle. From these calculations it provides further indication that the corner of the nanoparticle is the most reactive, due to its low coordination and higher strain

at this region. Secondly, molecular dynamics simulations were used to study the structure of water around an MgO and calcite nanoparticle. The 3-dimensional projections of the water structure around the larger MgO nanoparticle is very structured and layering around the sides of the nanoparticle is clear up to 8-10Å above the surface. The smaller calcite nanoparticle, which is amorphous in vacuum, retains more of its crystal structure in water. However, the structure and layering of water is not as apparent as in the MgO nanoparticle. The residence times of water in the first hydration shell at different positions of the MgO nanoparticle reinforce the energy minimisation calculations. The residence times at the side is far greater than at the more reactive corner and edge sites. The calcite nanoparticle has so few ions in bulk that the residence times are more comparable with the residence time of a water molecule around an isolated calcium ion rather than calcium on a 2-dimensional surface. The chapter finished with a preliminary study into analysing the distribution of electrolytes around different charged MgO nanoparticles. All simulations need to be run longer in order to see phenomena such as the electric double layer, but initial findings are promising. By increasing the effective charge of the MgO nanoparticle from +1 to +3 the simulation showed increased ordering of chlorine ions at around 5.2Å above the surface.

While this chapter investigated the interaction of single nanoparticles with its environment, the next chapter is the study of the interactions of two or more nanoparticles with each other.

Chapter 6

Aggregation of Mineral Nanoparticles

An understanding of aggregating nanoparticles is of technological, geochemical and biological importance [236, 237]. The stability of colloids depends on the forces that drive or inhibit aggregation [101] and the biomineralisation process is a result of aggregating mineral nanoparticles [238]. In this chapter, we use molecular dynamics simulations to describe this process. We have considered the aggregation of different materials, i.e. periclase and calcite, initially in vacuum, to see whether the aggregation is dependent on the composition of the material. Furthermore, as a means of quantifying this process we have evaluated the free energy change as two nanoparticles are brought together.

6.1 Aggregation of Magnesium Oxide Nanoparticles

A study of the structural changes that occur during aggregation was performed using molecular dynamics simulations initially by modelling an eight nanoparticle system. Each of the nanoparticles in the starting configuration was the same distance apart. The simulation was performed in vacuum with no periodic boundary conditions. To ensure that each nanoparticle could interact with each other and that there would be no discontinuity in the interaction energy, a cut-off of 70Å was used in the simulation. The system used a canonical ensemble at 300K and ambient pressure using a time step of 0.1fs. The simulation was run for 1ns with a 2ps equilibration period.

Each {100} MgO nanoparticle had a diameter of 1.01nm and the simulation started with them being 2.3nm apart, i.e. the centre to centre distance was 3.0nm. The starting configuration is shown in figure 6.1. The potential energy of the simulation is plotted as it evolves over time (figure 6.2).

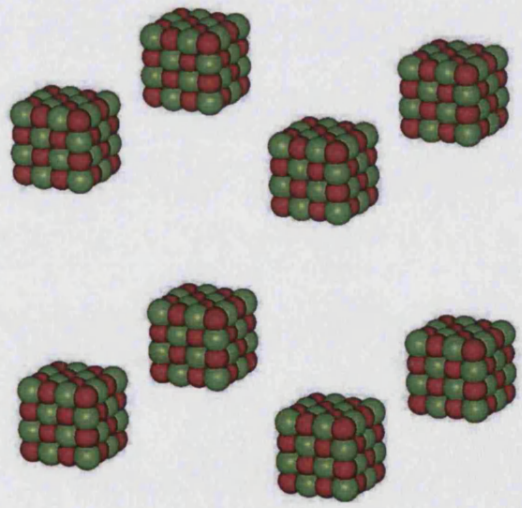

Figure 6.1: Initial configuration of eight MgO nanoparticles before aggregation

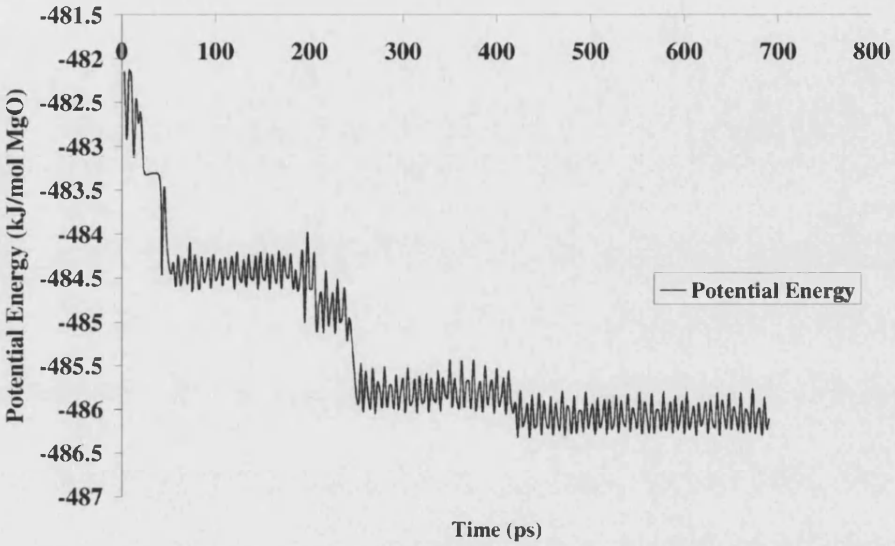

Figure 6.2: Potential energy per magnesium ion against time of an MD simulation of 8 MgO nanoparticles

The starting configuration has a potential energy of -482.1kJ/mol of Mg ions and then drops rapidly in-between 30-55ps to -484.1kJ/mol. This decrease in potential energy corresponds to the initial aggregation of MgO nanoparticles. Figure 6.3a shows a snapshot of the MD simulation at 30ps. The particles retain their bulk-like structure and have well ordered surfaces. At 30ps, single MgO nanoparticles are starting to aggregate together in pairs. The aggregation seems very ordered and is dominated by orientation along the {100} plane. This snapshot is also interesting because it shows that joining nanoparticles will join at the corners first. This is in good agreement with the results presented in chapter 5 which showed that the most reactive position on a MgO nanoparticle is at the corner. The pair of nanoparticles that is circled in figure 6.3a is a pair that drifts further and further away from the rest of the nanoparticles has not aggregated with the other six nanoparticles by the end of the simulation. Since they are so far away it is not practical to show them in

subsequent figures. At 60ps, figure 6.2 shows a stabilisation of potential energy at -484.4kJ/mol. Figure 6.3b shows a snapshot of the MD simulation at 60ps and shows the aggregation of a single MgO nanoparticle to a pair. The snapshot again illustrates the general result that aggregation has initially occurred along the corners of the nanoparticles. The nanoparticles find their preferred face centre cubic site at 220ps (figure 6.3c) when the potential energy decreases to around -484.6kJ/mol. The increased ordering of aggregation along the {100} plane continues when the potential energy decreases to -485.8kJ/mol, when a pair of nanoparticles aggregate to the triplet at 275ps (figure 6.3d). The final configuration occurs at 460ps, shown in figure 6.3e. Here the sixth nanoparticle joins the cluster of five. The two nanoparticles circled in Figure 6.3a were in fact too far away to become attracted to the rest of them. This aggregation process has also shown that when crystal growth occurs in MgO there are the chances of kinks and steps being formed.

Any structural changes that may occur during aggregation may be observed by comparing the RDF of aggregated nanoparticles with bulk MgO. Figure 6.4 shows the RDF of the (a) aggregated MgO nanoparticles and (b) bulk MgO. The RDF's of the aggregated MgO nanoparticles and bulk MgO are very similar with the first three peaks showing Mg-O bond distances at 2.1, 3.5 and 4.5Å in both graphs. These interatomic distances agree with x-ray diffraction experiments [222, 239].

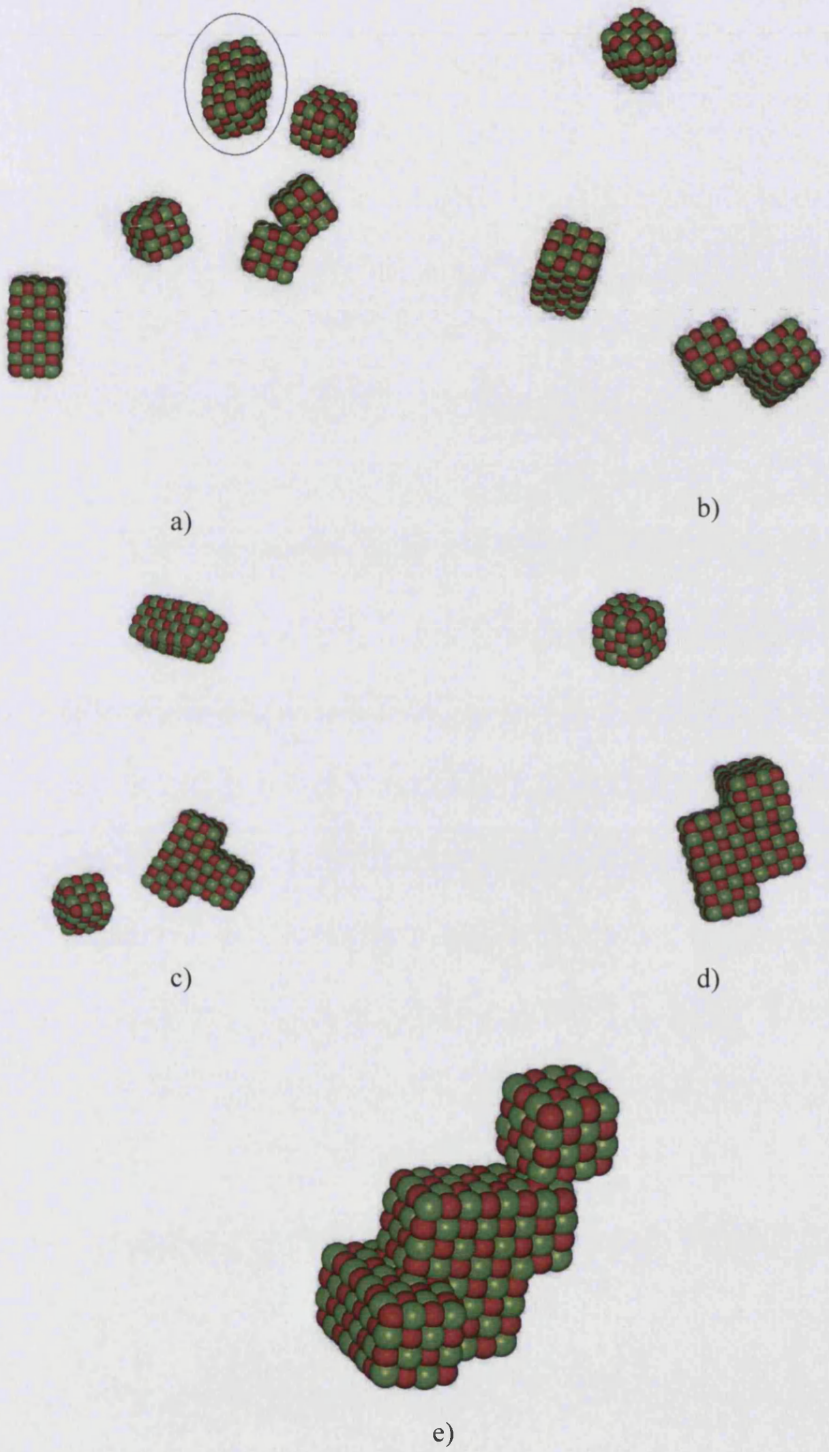

Figure 6.3: Snapshots of the MD simulation at a) 30ps, b) 60ps, c) 220ps, d) 275ps and e) final configuration of the MgO system

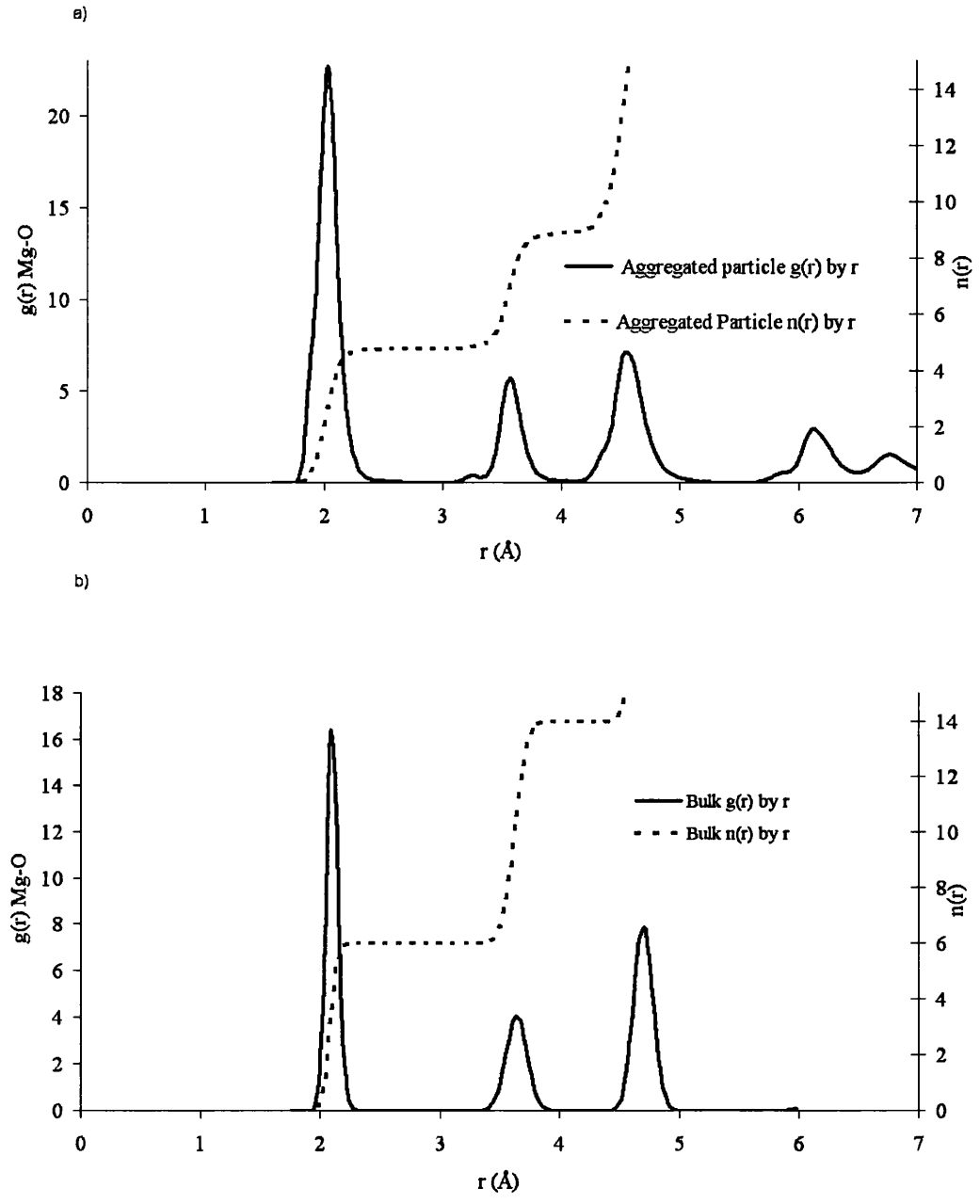

Figure 6.4: RDF of the (a) aggregated MgO nanoparticles and (b) bulk MgO

The RDF of the aggregated nanoparticles shows that during aggregation the MgO nanoparticles maintain their crystalline form. Furthermore, the bonding between

magnesium and oxygen is so highly directed, resulting in a continuous structure. Therefore, although the overall shape is non-symmetric there are no obvious grain boundaries being formed. Next we show the aggregation process of eight calcite nanoparticles.

6.2 Aggregation of Calcite Nanoparticles

Eight $\{10\bar{1}4\}$ calcite nanoparticles that were 1.6nm in diameter were placed 1.7nm apart, i.e. the centre to centre distance was 3.0nm. The starting configuration is shown in figure 6.5. The simulation was run for 1ns. Figure 6.6 shows the potential energy of the system as a function of MD time.

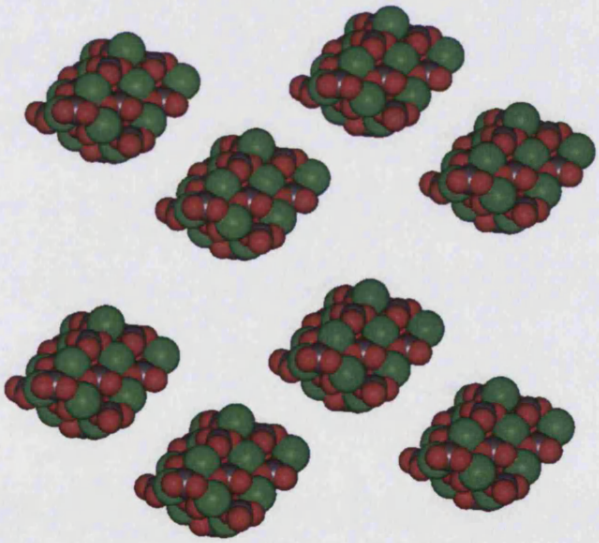

Figure 6.5: Initial configuration of calcite nanoparticles for MD simulation

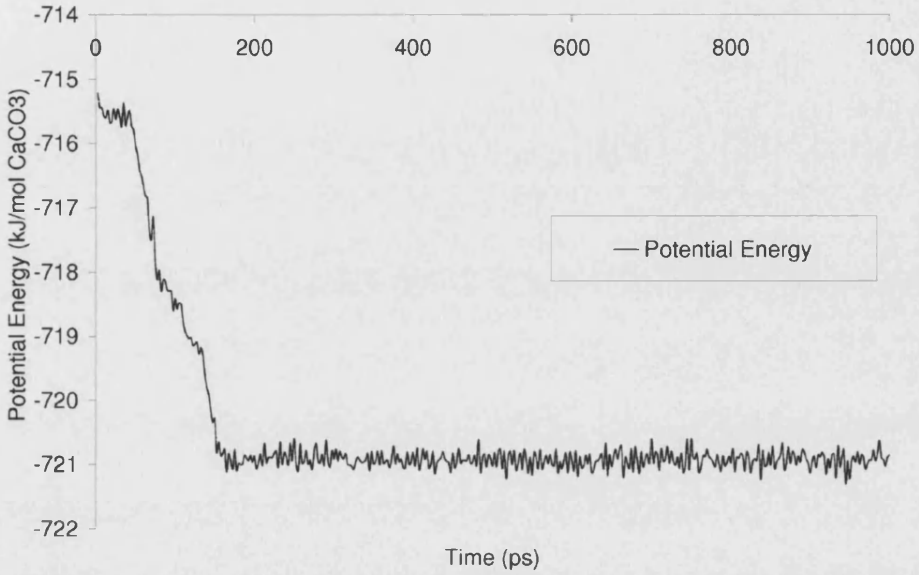

Figure 6.6: Potential energy per calcium ion against time of an MD simulation of 8 calcite nanoparticles

The simulation starts with a potential energy of -715.3kJ/mol of calcium ions. As the simulation evolves, the first drop in potential energy occurs at around 50ps. This corresponds to figure 6.7a which shows that before aggregation occurs the individual nanoparticles will relax independently resulting in a disordered structure. Once the calcite particles are relaxed aggregation then occurs in pairs similar to MgO. At around 67ps the eight nanoparticles had formed four nanoparticles and the energy lowered to –716.9kJ/mol. Figure 6.7b shows a snapshot of aggregation at 87ps. The potential energy of this system continues to lower, -718.2kJ/mol, as the four calcite nanoparticles start to form two larger nanoparticles. The two larger calcite nanoparticles now become attracted to each other and again as they join the potential energy drops to -719.9kJ/mol at around 140ps (figure 6.7c). The final

configuration occurs at 180ps and the potential energy stabilises at -721.0kJ/mol. Figure 6.7d shows the aggregated nanoparticle, which has lost its symmetry.

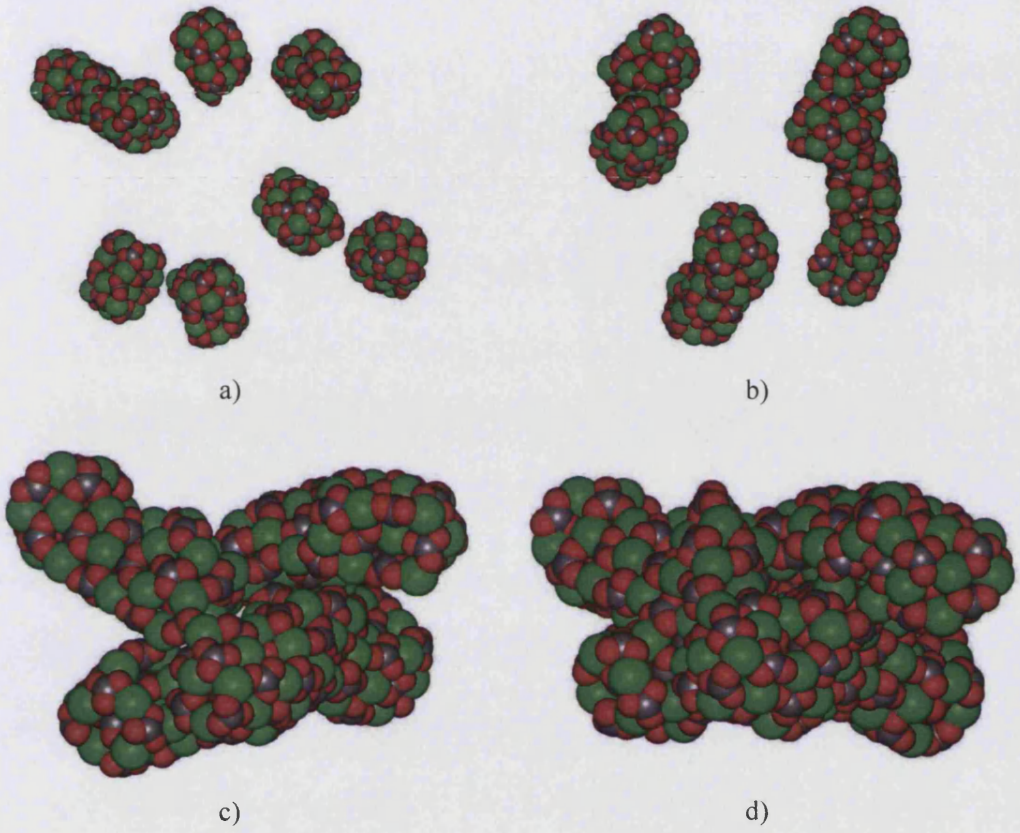

Figure 6.7: Snapshots of the MD simulation at a) 50ps, b) 87ps, c) 140ps, and d) final configuration of the calcite system

Figure 6.8a shows the RDF of the final aggregated calcite nanoparticle. When compared with the RDF of bulk calcite (figure 6.8b) it has much less order than the crystalline bulk. The peaks in the RDF bulk calcite show the same Ca-O bond distances, 2.3, 3.3 and 4.1Å, as found experimentally [240, 241].

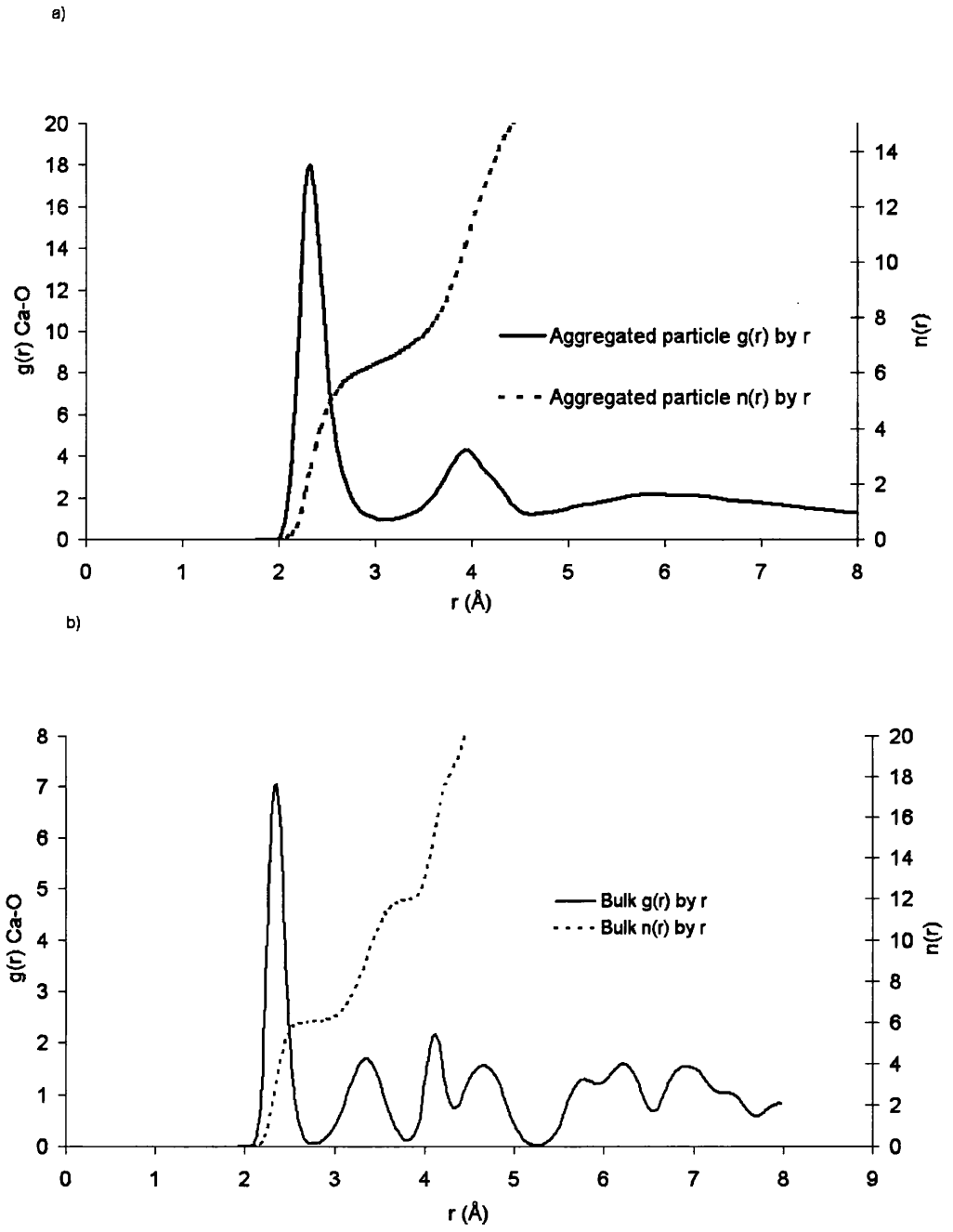

Figure 6.8: RDF of the (a) aggregated calcite nanoparticles and (b) bulk calcite

The average coordination number for a calcium ion in the aggregated nanoparticle is calculated to be 6.5, which is slightly higher then the coordination number for bulk calcite which is 6. This suggests that the amorphous nanoparticle is more

closely related to calcite, rather than aragonite which has a calcium ion coordination number of 8. However, another possible explanation could be that the small nanoparticles have formed (or trying to form) the vaterite morphology, which has a disordered structure and six-fold coordinate [242]. There have been experimental studies of growing calcite particles where vaterite forms first and then as the crystal grows bigger the calcite morphology dominants [243].

There has been a great deal of debate in the literature suggesting that biomineralisation occurs from amorphous calcium carbonate [7, 244-246]. We have shown that very small calcium carbonate nanoparticles are more stable when amorphous and also, when they aggregate together, their morphology changes drastically. Therefore, this aggregation process could promote the exotic morphologies seen in biomineralisation.

We have shown that the aggregation can be modelled explicitly. There have been other studies in the literature documenting the aggregation process of other minerals [237], only in a qualitative manner. The remainder of this chapter will focus on our attempt to model the aggregation process can be quantified in a quantitative manner, particular by modelling the free-energy of aggregation.

6.3 Free Energy of Aggregation

The free energy of aggregation is obtained by performing a series of MD simulations where two identical nanoparticles are held at fixed distances apart and then integrating the force required to keep them at end distance. The approach is based on a Potential of Mean Force (PMF) and as described in chapter 3 it is a generalisation of bond constraints that can be made to constrain a system along a reaction coordinate. If a number of simulations are conducted with the system constrained at different points along the reaction coordinate, then the mean

constraint force may be plotted as a function of reaction coordinate and the function integrated to give the free energy change of the overall process [247]:

$$G_{PMF} = \frac{-W_{PMF}}{d_{PMF}} \tag{6.1}$$

Where G_{PMF} is the free energy of the system, W_{PMF} is the PMF constraint virial, d_{PMF} is the constraint distance between the two groups used to define the reaction coordinate. We fix two of the central cations in both nanoparticles with this PMF constraint. The constraint distance d_{PMF}, then becomes the centre to centre distance of the two nanoparticles. This technique has been used in the past to measure the intermolecular forces between two gold passivated nanoparticles [248].

Two {100} 1.01nm magnesium oxide nanoparticles were placed in a range of 0.7 to 23.7Å apart. Twenty-four independent MD simulations were performed with no periodic boundary conditions. A cut-off of 60Å and the NVE ensemble was used with a 0.2fs time step. Each simulation was run for 1ns with the first 200ps used for equilibration. Figure 6.9 shows the free energy profile versus distance of two MgO nanoparticles.

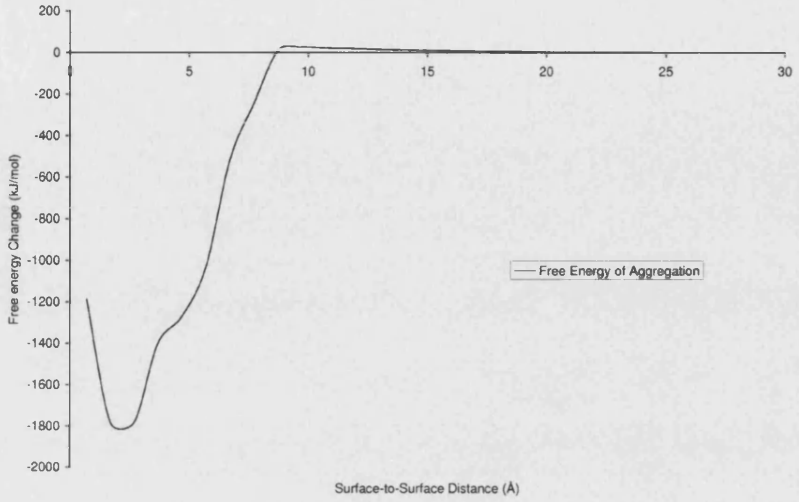

Figure 6.9: Free energy of aggregation of two 1.01nm MgO nanoparticles as a function of distance

The first feature of figure 6.9 is that there is a huge decrease in free energy from 9.7Å to 2.7Å apart. At 9.7Å apart the two MgO nanoparticles are able to form a bond at corner to corner sites. Figure 6.10 shows the final configuration of two MgO nanoparticles at 9.7Å apart and the nanoparticles have joined together.

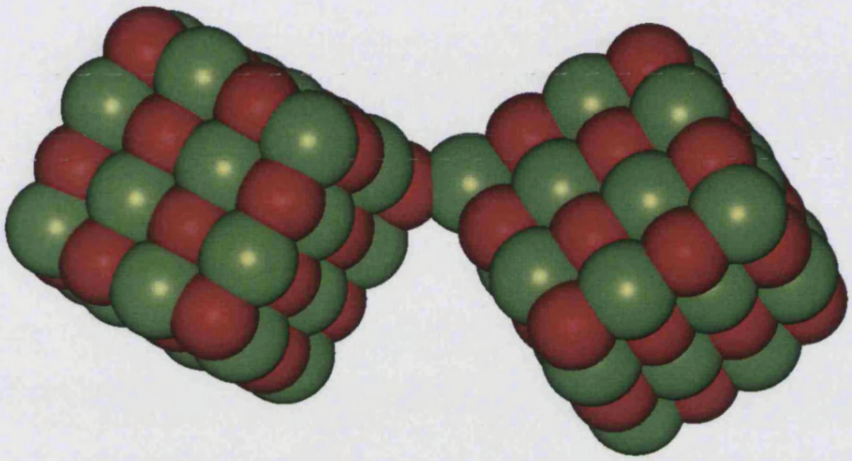

Figure 6.10: Final configuration of two MgO 1.01nm diameter nanoparticles 9.7Å apart

The bond distance between a magnesium ion and an oxygen ion in MgO is 2.1Å. Therefore, it is not surprising that when the surface-to-surface distance goes below that there is overlapping of ions and an increase in free energy. However, another feature of figure 6.9 is that the free energy leading up to 9.7Å is positive and gradually increasing. Figure 6.11 shows a scaled up free energy profile to see this increase in positive free energy as a function of distance.

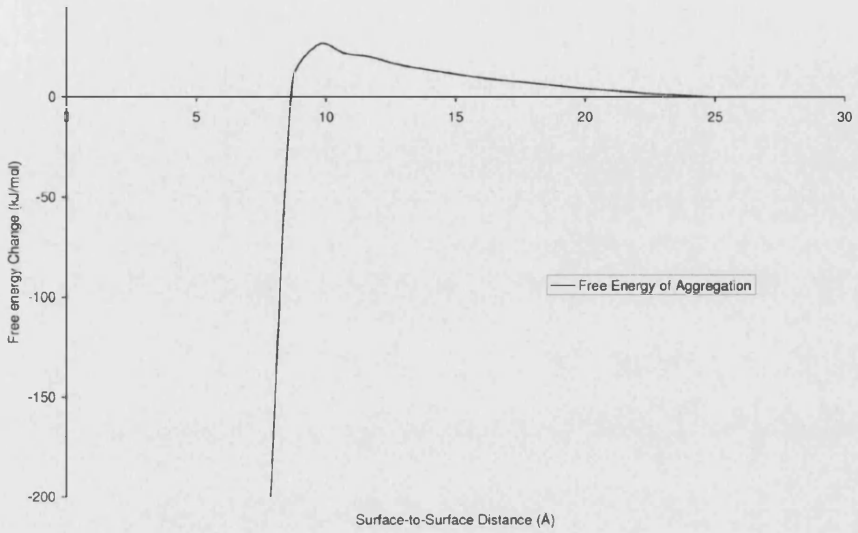

Figure 6.11: Scaled up free energy profile of two 1.01nm MgO nanoparticles

This increase in free energy just before the nanoparticles touch introduces a problem because as shown earlier in the chapter, nanoparticles of this size aggregate together quite easily. The free energy barrier suggests that there is a kinetic barrier to aggregation in vacuum.

The same procedure was applied to two $\{10\bar{1}4\}$ 1.6nm calcite nanoparticles and two 1.7nm {100} MgO nanoparticles in-order to see if this free energy barrier occurs in other simulations. Figure 6.12 shows the free energy change as a function of distance for two 1.6nm calcite nanoparticles and two 1.7nm MgO nanoparticles.

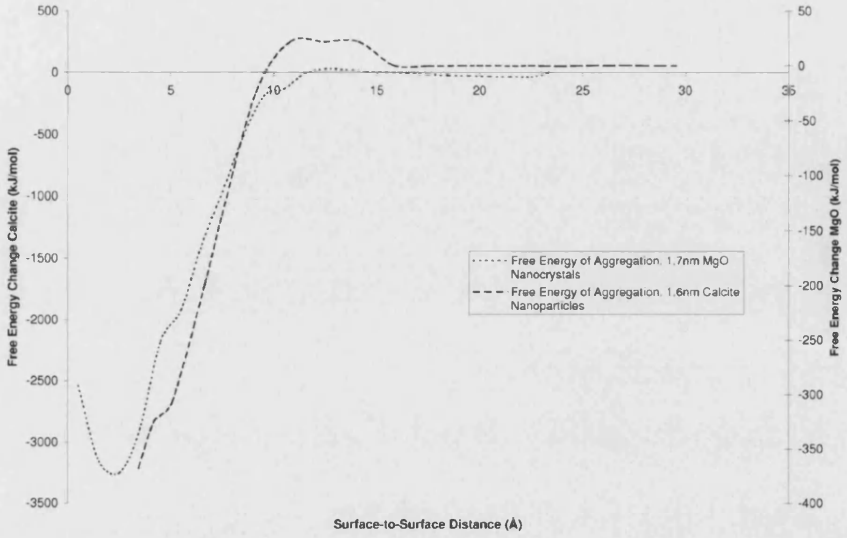

Figure 6.12: Free energy profile as a function of distance of two 1.6nm calcite nanoparticles and two 1.7nm MgO nanoparticles

The same trend is also observed in the larger MgO nanoparticles and in the calcite nanoparticles. The increase in free energy occurs just before the particles are about to touch. The free energy barrier is observed for all simulations, therefore, the way in which the free energy is calculated should be investigated.

A study into the definition of the PMF bond constraint was performed first. Instead of placing the PMF bond constraint between the two central cations of each nanoparticle, it was placed between all the cations of the 1.01nm MgO nanoparticle. Therefore, the average PMF bond constraint is calculated between the centre of mass of each nanoparticle. Figure 6.13 shows the free energy change as a function of distance of the two different ways of defining the PMF bond constraint.

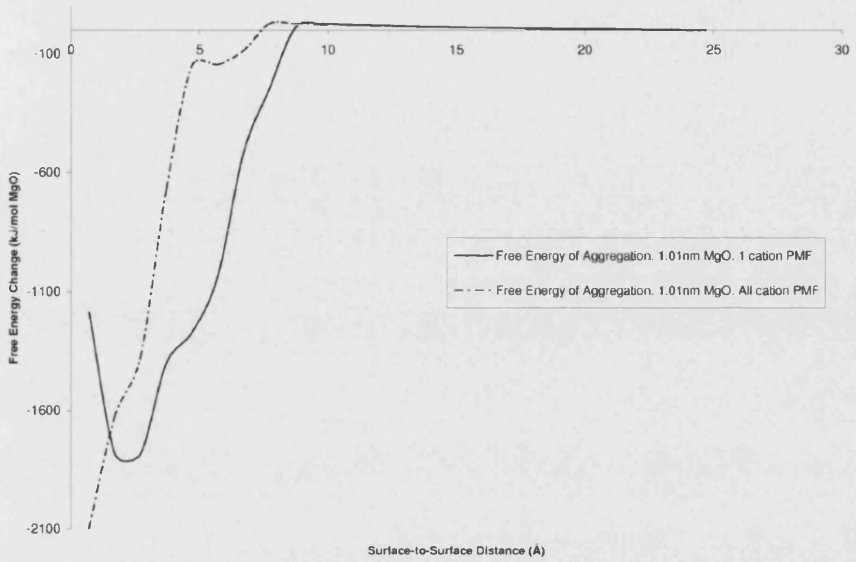

Figure 6.13: Free energy profile of two different ways of defining the PMF bond constraint as a function of distance.

This method has still not prevented the free energy barrier occurring. In addition, the PMF bond constraint is so strong that instead of showing an increase in free energy at the very close distances there is a continued decrease in free energy. This is due to the temperature increasing so much that the nanoparticles begin to melt so as to try and keep all the cation distances the same. Figure 6.14 shows the end configuration of two MgO nanoparticles at 0.7Å apart, where the MgO nanoparticles have melted into one.

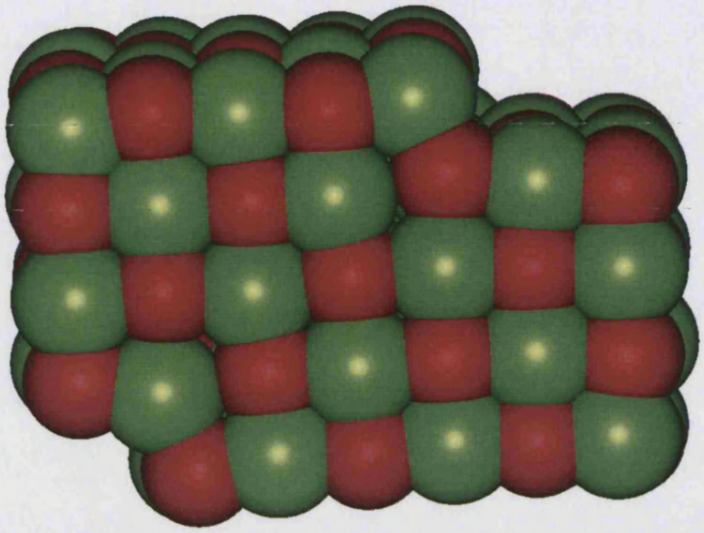

Figure 6.14: Two MgO nanoparticles at 0.7Å apart with PMF bond constraints between all cations.

In all cases the two particles are being held at a set distance apart by putting a PMF constraint between the cations in the particles. In each case the particles are free to spin, rotate or indeed move anywhere in the simulation cell but at any given time in the simulation the distance between them is always the constant. As the particles are brought closer together the particles stop spinning because of the increasing interaction between the two particles. Therefore, the particles are sampling less configurational space then if they were a single particle. This has the effect of increasing the entropy of the system because of increased order as the particles are brought together.

The rotational entropy of two isolated nanoparticles can be calculated and therefore, the rotational contribution to the Helmholtz free energy can be determined by using the partition function shown by equation 6.2:

$$q_{rot} = \frac{\sqrt{\pi}}{\sigma}\left[\left(\frac{T}{\theta_{r,x}}\right)\left(\frac{T}{\theta_{r,y}}\right)\left(\frac{T}{\theta_{r,z}}\right)\right]^{\frac{1}{2}} \tag{6.2}$$

Where σ is the symmetry number, which is the number of indistinguishable orientations that can be produced by rotations less than or equal to 360° about any axis through its centre of mass. The rotational partition function has to take into account the three independent moments of inertia, which is one moment for each mutually perpendicular axis of rotation. One way of achieving this is by recognising the existence of three independent characteristic rotational temperatures $\theta_{r,x}$, $\theta_{r,y}$, and $\theta_{r,z}$, which corresponds to the three principal moments of inertia I_x, I_y, and I_z, The characteristic rotational temperature is defined by:

$$\theta_r = \frac{h^2}{8\pi^2 Ik} = \frac{hcB}{k} \tag{6.3}$$

Where h is Planck's constant and B is the rotational constant. Table 6.1 compares the free energy barrier of two isolated nanoparticles from the rotational entropic effect and the calculated free energy barrier from the molecular dynamics simulation.

Table 6.1: Comparison of the free energy barrier associated with rotational entropy and the calculated free energy barrier from MD simulations

Molecular Dynamics Simulation	Free Energy Barrier Associated with Rotational Entropy (kJ/mol)	Calculated Free Energy Barrier (kJ/mol)
1.01nm MgO	88.04	26.14
1.70nm MgO	103.48	29.84
1.60nm Calcite	108.42	21.86

From Table 6.1 shows that the calculated free energy barrier is lower then the free energy barrier associated with rotational energy, which indicates the interaction between nanoparticles are lowering the free energy change. Therefore, the next simulations fixed the nanoparticles as they approach one another so that there was no rotation allowed. This would give an indication if there is still an entropic effect on the aggregating nanoparticles.

The three different nanoparticle systems were set up in the same way, however, in addition to the PMF constraint, four cations on the opposite surfaces of each nanoparticle were held fixed. Therefore, the nanoparticles are unable to spin or rotate. Figure 6.15 shows the free energy profiles of the three different nanoparticles as a function of distance with the nanoparticles unable to spin or rotate.

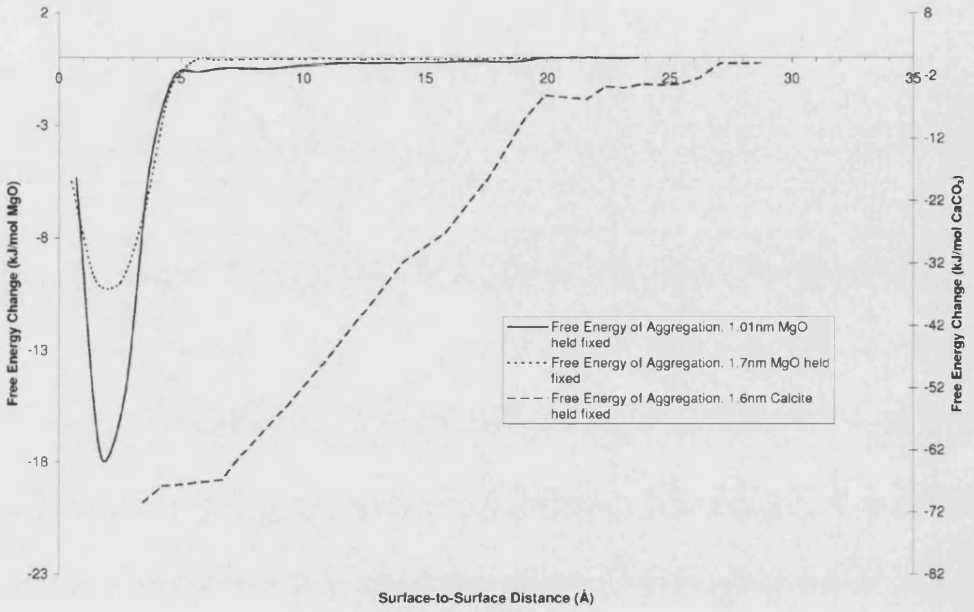

Figure 6.15: Free energy profile as a function of distance with the nanoparticles held fixed

Figure 6.15 shows that in all three cases the free energy profile is now negative and decreases as distance is reduced until the distance between nanoparticles is so small that they repel. This method may not be appropriate for calcite because of the amorphous nature of calcite nanoparticles in vacuum. The consequent disruption on the free energy profile for calcite has caused the shape of the curve to change significantly. The free energy profiles of the two MgO nanoparticles show that the larger nanoparticle has a deeper free energy well than the smaller one. In order to see the effect of size of the free energy process different sized MgO nanoparticles need to be simulated.

In chapter 1 there is a description of colloidal stability and one method of trying to quantify this process is by the use of the Hamaker constant [100, 101]. By calculating the interaction energy of the two 1.01nm MgO nanoparticles at different distances and using the Hamaker constant, as calculated by Bergstrom in 1997 [101] for MgO, we are able to calculate a free energy curve using this method. The equation used to calculate the interaction energy at different distances apart is given in equation 1.2. Figure 6.16 shows a comparison of free energy profiles of the two different methods. The free energy profile using MD simulations has much more structure and at very small distances apart there is an increase in free energy which indicates repulsion. The van der Waals free energy, calculated using the Hamaker constant, will always be attractive when calculating the interaction between the same solid. However, it can not be used at very close distances. Clearly MD simulations could be used to describe the interparticle potentials as particles are brought together in a more quantitative way.

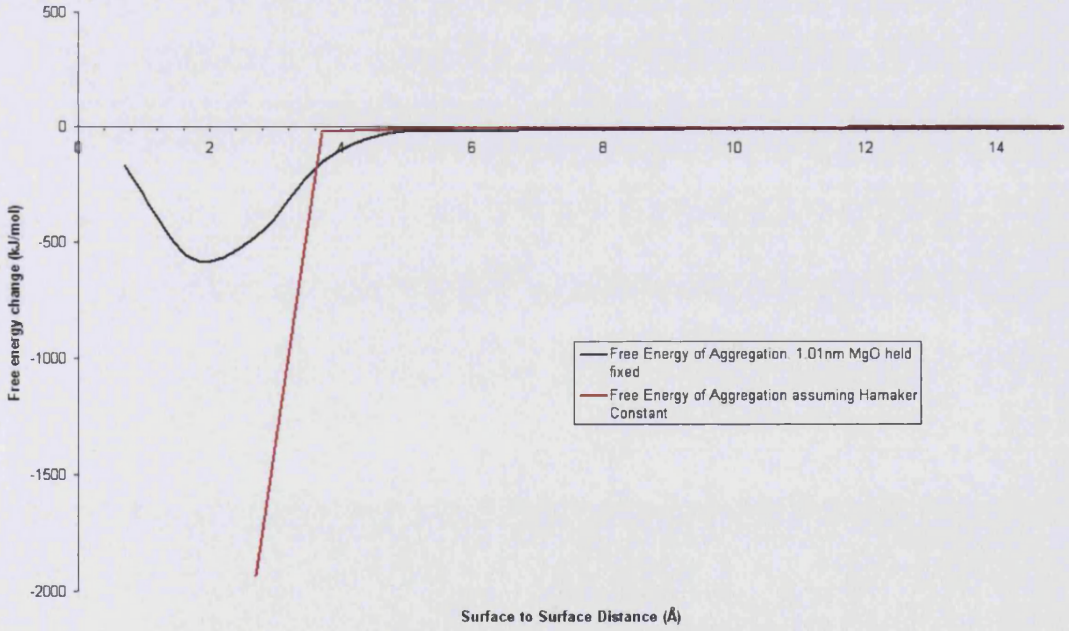

Figure 6.16: Comparison of the free energy of aggregation of two 1.01nm MgO nanoparticles using MD simulations, where the particles are held fixed and calculating the free energy was calculated using of the Hamaker constant

This chapter has shown that the aggregation process of two different minerals can evolve differently over time. The aggregation of MgO is strongly influenced by the stability of the {100} surface. The {100} surface dominates the orientation as each nanoparticle aggregates toward each other. The aggregation of $\{10\bar{1}4\}$ calcite nanoparticles does not show the same highly ordered aggregation process but rather the amorphous nature of very small calcite nanoparticles causes a disordered final structure. This process can be quantified by calculating the free energy change as the nanoparticles are brought closer together. By using a number of PMF calculations, the free energy of aggregation can be evaluated and provides a new alternative approach for quantifying particle interactions used in the investigation of the stability of colloids, which in the past has used a Hamaker constant and Lifshitz theory. The Hamaker constant has the problem of additivity in its calculation and Lifshitz theory is difficult to apply. Future work in this study should include aqueous media between the aggregating nanoparticles to see the effect it has on the free energy of aggregation.

Chapter 7

Conclusions

The aim of the work described in this thesis has been to increase current understanding at processes that occur at the mineral-water interface. Two minerals were studied in detail, the polymorph of calcium carbonate, calcite and magnesium oxide, periclase. The results in this thesis cover a range of different calcite surfaces as well as mineral nanoparticles.

Chapter 4 illustrated the structure and stability of seven different calcite surfaces. The surfaces described include the most stable, flat $\{10\bar{1}4\}$ surface. Two vicinal surfaces were also considered; the $\{31\bar{4}8\}$ and $\{3\bar{1}\bar{2}16\}$, where each consists of flat $\{10\bar{1}4\}$ terraces, acute and obtuse steps. Four kinked surfaces were also considered. On a step edge, a kink is an offset where the edge jumps one or more

atomic units. The four different kinked surfaces can be identified by first considering the orientation of the step and then the orientation of the partial step at the kink. Therefore, the four different surfaces are acute-acute (AA), acute-obtuse (AO), obtuse-acute (OA) and obtuse-obtuse (OO). Using energy minimisation methods and molecular dynamics simulations the most stable of the dry surfaces is the flat $\{10\bar{1}4\}$ surface with the obtuse step being the next most stable. In vacuum, the ions at the acute kinks are so mobile that they reconstruct to form obtuse angled kinks. In aqueous conditions the acute kinks are stabilised by the water around it. The structure of water changes above the different surfaces. On a flat surface there is increased ordering with three distinct layers found at 2.5, 3.5 and 5.0Å above the surface. The introduction of a step in the surface does not disrupt the layering of water in the direction normal to the surface, however, there is some disruption in the direction normal to the step. On kinked surfaces the distance between the nearest neighbour water molecule to the surface is the same as on flat surfaces but there is less ordering of water above the surface.

The dissolution of ions from calcite surfaces were modelled by evaluating the free energy change of dissolution of calcium and carbonate ions from the flat and stepped surfaces. The dissolution process from a flat surface is more unfavourable than dissolution from a stepped site. The ratios of the free energies for the different processes were reasonably constant.

To increase the complexity of the system, two salts of polyacrylic acid (PAA), calcium and sodium, were considered and interacted with a flat calcite surface. Firstly, the potential had to be derived and then tested in vacuum and aqueous conditions. The sodium salt of PAA behaves differently in aqueous conditions than the calcium salt as the sodium ions are easily solvated by the water molecules. The initial study showed that fully coordinated PAA chains with their cations are very stable and, therefore, there is no driving force to adsorb onto the surface. However, adsorption can occur by moving one of the cations from the chain to the surface,

thus creating a charged surface for the oppositely charged PAA molecule to be attracted to.

Chapter 5 involved a study of the structure and stability of mineral nanoparticles. Energy minimisation was used to estimate the free energy of dissociatively adsorbing water at different positions on the MgO {100} nanoparticle. These calculations show that the corner of the nanoparticle is the most reactive due to the low coordination of the ions and the higher strain at this region. Molecular dynamics simulations were then used to study the structure of water around both MgO and calcite nanoparticles. The 3-dimensional projections of the water structure around the larger MgO nanoparticle shows the water to be very structured and layered along the sides of the nanoparticle up to 8-10Å above the surface. This is in contrast to the structure at the corners and edges where there is little structure.

A smaller $\{10\bar{1}4\}$ calcite nanoparticle was immersed in water. In contrast to MgO there was not as much ordering and the water residence times indicate that the calcite nanoparticle is in fact behaving more like an isolated calcium ion in water rather than a 2-dimensional calcite surface. As is consistent with other studies of nanoparticles in water the crystal structure is maintained in aqueous conditions compared in vacuum. Charged MgO nanoparticles were then considered in electrolyte solutions. The introduction of salt in solution does not significantly change the structure of water around the nanoparticle. The charge of the MgO nanoparticle was first set at +1. The majority of chlorine ions are 7.4 and 9.4Å from the surface. As the charge on the nanoparticle increased to +3 the ordering of the oppositely charged ion are closer to the surface at 5.4 and 7.3Å. However, in order to simulate phenomena such as the electric double layer these simulations need to be run longer.

Chapter 6 describes the aggregation of calcite and MgO nanoparticles. During the MD simulations the aggregation of MgO nanoparticles forms a very ordered structure, which is orientated along the <100> direction. It is interesting to note that

the aggregation of MgO nanoparticles occurs by the formation of bonds at the reactive corners first. By comparing the RDF of the magnesium and oxygen ions in the final aggregated structure and bulk MgO there is no significant difference in the crystal structure. In contrast the aggregation of calcite nanoparticles form a very amorphous structure. Comparison of the RDF between the calcium and oxygen ions of the final aggregated structure and bulk calcite shows that the final structure loses some of its crystal structure and could be forming the vaterite morphology of calcium carbonate.

One major deficiency in the literature is a quantitative method to describe the aggregation of mineral nanoparticles. By performing a number of PMF calculations the free energy change of aggregation is evaluated for two different sized MgO nanoparticles and calcite nanoparticles. Early studies indicate that as the two nanoparticles aggregate together there is a free energy barrier which must be overcome just before the nanoparticle join. The free energy barrier is associated with the increased ordering as the nanoparticles are sampling less configuration space at very short separations. This increases the rotational entropy and hence increases the free energy, creating a barrier. By holding the nanoparticles fixed at the corners, as the nanoparticles aggregate, they are unable to rotate. The free energy change of aggregation then shows no free energy barrier. This method could be applied to aggregation in different media to determine the effect of different solvents and different charge states on aggregating mineral nanoparticles.

This work has hopefully addressed some of the issues raised in the introduction particularly, trying to identify the structure of water in contact with more complex mineral interfaces and the effect on key properties. However, this work can be taken further still. The dissolution of ions from kinked surfaces is essential in order to fully understand the relative stabilities of these sites and their role in the rates of growth. The interfacial energies of polymeric additives on kinked calcite surfaces could reveal the adsorption process and their effects on the stability and ultimately growth of the kinked sites. We have shown that the aggregation process can be

quantified however all the calculations were performed in vacuum. Therefore, a full free energy profile of aggregating nanoparticles in aqueous solution is required and the structured nature of water around nanoparticles could have an effect on the aggregation process. From our initial calculations there is evidence that the electric double layer will form around charged nanoparticles and we now have all elements in place to see what contribution the electric double layer has on the free energy of aggregation, which is at the heart of colloidal chemistry. This atomistic simulation technique is poised to address this important area.

References

1. Brown, G.E., V.E. Henrich, W.H. Casey, D.L. Clark, C. Eggleston, A. Felmy, D.W. Goodman, M. Gratzel, G. Maciel, M.I. McCarthy, K.H. Nealson, D.A. Sverjensky, M.F. Toney, and J.M. Zachara, *Metal oxide surfaces and their interactions with aqueous solutions and microbial organisms*, Chem. Rev., **99,** 77-174 (1999)
2. Brown, G.E., *Surface science - How minerals react with water*, Science, **294,** 67-+ (2001)
3. Nachtegaal, M. and D.L. Sparks, *Effect of iron oxide coatings on zinc sorption mechanisms at the clay-mineral/water interface*, J. Colloid Interface Sci., **276,** 13-23 (2004)
4. Catalano, J.G., Z. Zhang, P. Fenter, and M.J. Bedzyk, *Inner-sphere adsorption geometry of Se(IV) at the hematite (100)-water interface*, J. Colloid Interface Sci., **297,** 665-671 (2006)
5. Geissbuhler, P., P. Fenter, E. DiMasi, G. Srajer, L.B. Sorensen, and N.C. Sturchio, *Three-dimensional structure of the calcite-water interface by surface X-ray scattering*, Surf. Sci., **573,** 191-203 (2004)
6. Oonkhanond, B. and M.E. Mullins, *Electrical double-layer effects on the deposition of zeolite A on surfaces*, J. Colloid Interface Sci., **284,** 210-215 (2005)
7. Xu, X.R., J.T. Han, and K. Cho, *Formation of amorphous calcium carbonate thin films and their role in biomineralization*, Chem. Mat., **16,** 1740-1746 (2004)
8. Boskey, A.L., *Biomineralization: An overview*, Connect Tissue Res, **44,** 5-9 (2003)
9. Morse, J.W. and R.S. Arvidson, *The dissolution kinetics of major sedimentary carbonate minerals*, Earth-Sci. Rev., **58,** 51-84 (2002)
10. Zhang, X.Y., G.S. Zhuang, J.M. Chen, Y. Wang, X. Wang, Z.S. An, and P. Zhang, *Heterogeneous reactions of sulfur dioxide on typical mineral particles*, J. Phys. Chem. B, **110,** 12588-12596 (2006)
11. Hochella, M.F., *Atomic Structure, Microtopography, Composition, and Reactivity of Mineral Surfaces*, in *Mineral-Water Interface Geochemistry*, M.F. Hochella and A.F. White, Editors. 1990, Mineralogical Society of America: Chelsea. p. 87-128.
12. Chada, V.G.R., D.B. Hausner, D.R. Strongin, A.A. Rouff, and R.J. Reeder, *Divalent Cd and Pb uptake on calcite 10(1)over-bar4} cleavage faces: An XPS and AFM study*, J. Colloid Interface Sci., **288,** 350-360 (2005)
13. Lazarov, V.K., R. Plass, H.C. Poon, D.K. Saldin, M. Weinert, S.A. Chambers, and M. Gajdardziska-Josifovska, *Structure of the hydrogen-stabilized MgO(111)-(1x1) polar surface: Integrated experimental and theoretical studies*, Phys. Rev. B, **71,** 115434 (2005)

14. Mukkamala, S.B., C.E. Anson, and A.K. Powell, *Modelling calcium carbonate biomineralisation processes*, Journal of Inorganic Biochemistry, **100,** 1128-1138 (2006)
15. Provencio, P.P. and V.J. Polyak, *Iron oxide-rich filaments: Possible fossil bacteria in Lechuguilla Cave, New Mexico*, Geomicrobiology Journal, **18,** 297-309 (2001)
16. Cutting, R.S., C.A. Muryn, G. Thornton, and D.J. Vaughan, *Molecular scale investigations of the reactivity of magnetite with formic acid, pyridine, and carbon tetrachloride*, Geochim. Cosmochim. Acta, **70,** 3593-3612 (2006)
17. Komiyama, M. and M.M. Gu, *Atomic force microscopy images of MgO(100) and TiO2(110) under water and aqueous aromatic molecule solutions*, Applied Surface Science, **120,** 125-128 (1997)
18. Park, C., P.A. Fenter, N.C. Sturchio, and J.R. Regalbuto, *Probing outer-sphere adsorption of aqueous metal complexes at the oxide-water interface with resonant anomalous X-ray reflectivity*, Phys. Rev. Lett., **94,** (2005)
19. Fenter, P., P. Geissbuhler, E. DiMasi, G. Srajer, L.B. Sorensen, and N.C. Sturchio, *Surface speciation of calcite observed in situ by high-resolution X-ray reflectivity*, Geochim. Cosmochim. Acta, **64,** 1221-1228 (2000)
20. Fenter, P., M.T. McBride, G. Srajer, N.C. Sturchio, and D. Bosbach, *Structure of barite (001)- and (210)-water interfaces*, J. Phys. Chem. B, **105,** 8112-8119 (2001)
21. Fenter, P., H. Teng, P. Geissbuhler, J.M. Hanchar, K.L. Nagy, and N.C. Sturchio, *Atomic-scale structure of the orthoclase (001)-water interface measured with high-resolution X-ray reflectivity*, Geochim. Cosmochim. Acta, **64,** 3663-3673 (2000)
22. Didymus, J.M., P. Oliver, S. Mann, A.L. Devries, P.V. Hauschka, and P. Westbroek, *Influence of Low-Molecular-Weight and Macromolecular Organic Additives on the Morphology of Calcium-Carbonate*, J. Chem. Soc.-Faraday Trans., **89,** 2891-2900 (1993)
23. Henriksen, K., S.L.S. Stipp, J.R. Young, and P.R. Bown, *Tailoring calcite: Nanoscale AFM of coccolith biocrystals*, Am. Miner., **88,** 2040-2044 (2003)
24. Henriksen, K., J.R. Young, P.R. Bown, and S.L.S. Stipp, *Coccolith biomineralisation studied with atomic force microscopy*, Palaeontology, **47,** 725-743 (2004)
25. Eggleston, C.M., A.G. Stack, K.M. Rosso, and A.M. Bice, *Adatom Fe(III) on the hematite surface: Observation of a key reactive surface species*, Geochemical Transactions, **5,** 33-40 (2004)
26. Dobson, P.S., L.A. Bindley, J.V. Macpherson, and P.R. Unwin, *Atomic force microscopy investigation of the mechanism of calcite microcrystal growth under Kitano conditions*, Langmuir, **21,** 1255-1260 (2005)
27. Hillner, P.E., A.J. Gratz, S. Manne, and P.K. Hansma, *Atomic-Scale Imaging of Calcite Growth and Dissolution in Real-Time*, Geology, **20,** 359-362 (1992)
28. Hillner, P.E., S. Manne, A.J. Gratz, and P.K. Hansma, *Afm Images of Dissolution and Growth on a Calcite Crystal*, Ultramicroscopy, **42,** 1387-1393 (1992)

29. Park, N.S., M.W. Kim, S.C. Langford, and J.T. Dickinson, *Atomic layer wear of single-crystal calcite in aqueous solution scanning force microscopy*, J. Appl. Phys., **80,** 2680-2686 (1996)
30. Higgins, S.R., G. Jordan, and C.M. Eggleston, *Dissolution kinetics of magnesite in acidic aqueous solution: A hydrothermal atomic force microscopy study assessing step kinetics and dissolution flux*, Geochim. Cosmochim. Acta, **66,** 3201-3210 (2002)
31. Ju, S.H., M.T. Tang, S.H. Yang, and Y.N. Li, *Dissolution kinetics of smithsonite ore in ammonium chloride solution*, Hydrometallurgy, **80,** 67-74 (2005)
32. Duckworth, O.W. and S.T. Martin, *Connections between surface complexation and geometric models of mineral dissolution investigated for rhodochrosite*, Geochim. Cosmochim. Acta, **67,** 1787-1801 (2003)
33. Gutjahr, A., H. Dabringhaus, and R. Lacmann, *Studies of the growth and dissolution kinetics of the CaCO3 polymorphs calcite and aragonite .1. Growth and dissolution rates in water*, J. Cryst. Growth, **158,** 296-309 (1996)
34. Meyer, H.J., *Growth-Rate of Calcite from Aqueous-Solutions*, J. Cryst. Growth, **47,** 21-28 (1979)
35. Cubillas, P., S. Kohler, M. Prieto, C. Chairat, and E.H. Oelkers, *Experimental determination of the dissolution rates of calcite, aragonite, and bivalves*, Chemical Geology, **216,** 59-77 (2005)
36. Walter, L.M. and J.W. Morse, *The Dissolution Kinetics of Shallow Marine Carbonates in Seawater - a Laboratory Study*, Geochim. Cosmochim. Acta, **49,** 1503-1513 (1985)
37. Tracy, S.L., C.J.P. Francois, and H.M. Jennings, *The growth of calcite spherulites from solution I. Experimental design techniques*, J. Cryst. Growth, **193,** 374-381 (1998)
38. Tracy, S.L., D.A. Williams, and H.M. Jennings, *The growth of calcite spherulites from solution II. Kinetics of formation*, J. Cryst. Growth, **193,** 382-388 (1998)
39. Chibowski, E., A. Szczes, and L. Holysz, *Influence of sodium dodecyl sulfate and static magnetic field on the properties of freshly precipitated calcium carbonate*, Langmuir, **21,** 8114-8122 (2005)
40. Wada, N., K. Yamashita, and T. Umegaki, *Effects of carboxylic acids on calcite formation in the presence of Mg2+ ions*, J. Colloid Interface Sci., **212,** 357-364 (1999)
41. Donnet, M., P. Bowen, N. Jongen, J. Lemaitre, and H. Hofmann, *Use of seeds to control precipitation of calcium carbonate and determination of seed nature*, Langmuir, **21,** 100-108 (2005)
42. Qi, L.M., J. Li, and J.M. Ma, *Biomimetic morphogenesis of calcium carbonate in mixed solutions of surfactants and double-hydrophilic block copolymers*, Adv. Mater., **14,** 300-+ (2002)
43. Yu, Y.G., M. Lei, B. Cheng, and X.J. Zhao, *Effects of PAA additive and temperature on morphology of calcium carbonate particles*, J. Solid State Chem., **177,** 681-689 (2004)

44. Tong, H., W.T. Ma, L.L. Wang, P. Wan, J.M. Hu, and L.X. Cao, *Control over the crystal phase, shape, size and aggregation of calcium carbonate via a L-aspartic acid inducing process*, Biomaterials, **25,** 3923-3929 (2004)
45. Downs, R.T. and R.M. Hazen, *Chiral indices of crystalline surfaces as a measure enantioselective potential*, Journal of Molecular Catalysis a-Chemical, **216,** 273-285 (2004)
46. Hazen, R.M., *Genesis: Rocks, minerals, and the geochemical origin of life*, Elements, **1,** 135-137 (2005)
47. Hazen, R.M., T.R. Filley, and G.A. Goodfriend, *Selective adsorption of L- and D-amino acids on calcite: Implications for biochemical homochirality*, Proceedings of the National Academy of Sciences of the United States of America, **98,** 5487-5490 (2001)
48. Chadwick, A.V., *Small, but perfectly formed: The microstructure of nanocrystalline oxides*, Radiat. Eff. Defects Solids, **158,** 21-30 (2003)
49. Waychunas, G.A., C.S. Kim, and J.F. Banfield, *Nanoparticulate iron oxide minerals in soils and sediments: unique properties and contaminant scavenging mechanisms*, J. Nanopart. Res., **7,** 409-433 (2005)
50. Vogel, W., P.H. Borse, N. Deshmukh, and S.K. Kulkarni, *Structure and stability of monodisperse 1.4-nm ZnS particles stabilized by mercaptoethanol*, Langmuir, **16,** 2032-2037 (2000)
51. Gilbert, B., F. Huang, H.Z. Zhang, G.A. Waychunas, and J.F. Banfield, *Nanoparticles: Strained and stiff*, Science, **305,** 651-654 (2004)
52. Kistler, S., *Coherent Expanded-Aerogels*, J. Phys. Chem, **36,** 52-64 (1932)
53. Utamapanya, S., K.J. Klabunde, and J.R. Schlup, *Nanoscale Metal-Oxide Particles Clusters as Chemical Reagents - Synthesis and Properties of Ultrahigh Surface-Area Magnesium- Hydroxide and Magnesium-Oxide*, Chem. Mat., **3,** 175-181 (1991)
54. Stark, J.V. and K.J. Klabunde, *Nanoscale metal oxide particles/clusters as chemical reagents. Adsorption of hydrogen halides, nitric oxide, and sulfur trioxide on magnesium oxide nanocrystals and compared with microcrystals*, Chem. Mat., **8,** 1913-1918 (1996)
55. Lin, R.Y., J.Y. Zhang, and P.X. Zhang, *Nucleation and growth kinetics in synthesizing nanometer calcite*, J. Cryst. Growth, **245,** 309-320 (2002)
56. Ojo, S.A., L. Whitmore, B. Slater, and C.R.A. Catlow, *Understanding nucleation and growth using computer simulation*, Solid State Sci, **3,** 821-826 (2001)
57. Zhang, C. and P.J.D. Lindan, *Towards a first-principles picture of the oxide-water interface*, J. Chem. Phys., **119,** 9183-9190 (2003)
58. Todorov, I.T., N.L. Allan, M.Y. Lavrentiev, C.L. Freeman, C.E. Mohn, and J.A. Purton, *Simulation of mineral solid solutions at zero and high pressure using lattice statics, lattice dynamics and Monte Carlo methods*, J. Phys.-Condes. Matter, **16,** S2751-S2770 (2004)
59. Pandey, R., J.D. Gale, S.K. Sampath, and J.M. Recio, *Atomistic simulation study of spinel oxides: Zinc aluminate and zinc gallate*, J. Am. Ceram. Soc., **82,** 3337-3341 (1999)

60. Olson, C.L., J. Nelson, and M.S. Islam, *Defect chemistry, surface structures, and lithium insertion in anatase TiO2*, J. Phys. Chem. B, **110,** 9995-10001 (2006)
61. Redfern, S.E. and S.C. Parker, *Atomistic simulation of the effects of calcium and strontium defects on the surface structure and stability of BaSO4*, J. Chem. Soc.-Faraday Trans., **94,** 1947-1952 (1998)
62. Harris, D.J., G.W. Watson, and S.C. Parker, *Computer simulation of pressure-induced structural transitions in MgO 001 tilt grain boundaries*, Am. Miner., **84,** 138-143 (1999)
63. Trachenko, K., M.T. Dove, E. Artacho, I.T. Todorov, and W. Smith, *Atomistic simulations of resistance to amorphization by radiation damage*, Phys. Rev. B, **73,** (2006)
64. Rose, D.A. and I. Benjamin, *Molecular-Dynamics of Adiabatic and Nonadiabatic Electron-Transfer at the Metal-Water Interface*, J. Chem. Phys., **100,** 3545-3555 (1994)
65. de Leeuw, N.H. and S.C. Parker, *Molecular-dynamics simulation of MgO surfaces in liquid water using a shell-model potential for water*, Phys. Rev. B, **58,** 13901-13908 (1998)
66. Kerisit, S., S.C. Parker, and J.H. Harding, *Atomistic simulation of the dissociative adsorption of water on calcite surfaces*, J. Phys. Chem. B, **107,** 7676-7682 (2003)
67. Kerisit, S. and S.C. Parker, *Free energy of adsorption of water and calcium on the {10(1)over-bar-4} calcite surface*, Chem. Commun., 52-53 (2004)
68. Kerisit, S. and S.C. Parker, *Free Energy of Adsorption of Water and Metal Ions on the {104} Calcite Surface*, J. Am. Chem. Soc., **126,** 10152 - 10161 (2004)
69. Kristensen, R., S.L.S. Stipp, and K. Refson, *Modeling steps and kinks on the surface of calcite*, J. Chem. Phys., **121,** 8511-8523 (2004)
70. Tasker, P.W. and D.M. Duffy, *The Structure and Properties of the Stepped Surfaces of MgO and NiO*, Surf. Sci., **137,** 91-102 (1984)
71. McCoy, J.M. and J.P. LaFemina, *Kinetic Monte Carlo investigation of pit formation at the CaCO3(10(1)over-bar4) surface-water interface*, Surf. Sci., **373,** 288-299 (1997)
72. Liang, Y. and D.R. Baer, *Anisotropic dissolution at the CaCO3(10(1)over-bar4)-water interface*, Surf. Sci., **373,** 275-287 (1997)
73. Weeks, J.D. and G.H. Gilmer, in *Advances in Chemical Physics*, I. Prigogine and S.A. Rice, Editors. 1979, Wiley: New York. p. 157.
74. Cooper, T.G. and N.H. de Leeuw, *A computer modeling study of the competitive adsorption of water and organic surfactants at surfaces of the mineral scheelite*, Langmuir, **20,** 3984-3994 (2004)
75. de Leeuw, N.H. and T.G. Cooper, *A computer modeling study of the inhibiting effect of organic adsorbates on calcite crystal growth*, Cryst. Growth Des., **4,** 123-133 (2004)
76. Duffy, D.M. and J.H. Harding, *Modelling the interfaces between calcite crystals and Langmuir monolayers*, J. Mater. Chem., **12,** 3419-3425 (2002)

77. Duffy, D.M., A.M. Travaille, H. van Kempen, and J.H. Harding, *Effect of bicarbonate ions on the crystallization of calcite on self-assembled monolayers*, J. Phys. Chem. B, **109,** 5713-5718 (2005)
78. Hamad, S., S. Cristol, and C.R.A. Callow, *Surface structures and crystal morphology of ZnS: Computational study*, J. Phys. Chem. B, **106,** 11002-11008 (2002)
79. Spano, E., S. Hamad, and C.R.A. Catlow, *Computational evidence of bubble ZnS clusters*, J. Phys. Chem. B, **107,** 10337-10340 (2003)
80. Spano, E., S. Hamad, and C.R.A. Catlow, *ZnS bubble clusters with onion-like structures*, Chem. Commun., 864-865 (2004)
81. Golberg, D., Y. Bando, O. Stephan, and K. Kurashima, *Octahedral boron nitride fullerenes formed by electron beam irradiation*, Applied Physics Letters, **73,** 2441-2443 (1998)
82. Stephan, O., Y. Bando, A. Loiseau, F. Willaime, N. Shramchenko, T. Tamiya, and T. Sato, *Formation of small single-layer and nested BN cages under electron irradiation of nanotubes and bulk material*, Appl. Phys. A-Mater. Sci. Process., **67,** 107-111 (1998)
83. Hamad, S., C.R.A. Catlow, E. Spano, J.M. Matxain, and J.M. Ugalde, *Structure and properties of ZnS nanoclusters*, J. Phys. Chem. B, **109,** 2703-2709 (2005)
84. Hamad, S., C.R.A. Catlow, S.M. Woodley, S. Lago, and J.A. Mejias, *Structure and stability of small TiO2 nanoparticles*, J. Phys. Chem. B, **109,** 15741-15748 (2005)
85. Wales, D.J. and H.A. Scheraga, *Review: Chemistry - Global optimization of clusters, crystals, and biomolecules*, Science, **285,** 1368-1372 (1999)
86. Holland, J.H., *Adaptation in Natural and Artificial Systems*. 1975, Cambridge: University of Michigan Press.
87. Schmitt, L.M., *Theory of genetic algorithms*, Theoretical Computer Science, **259,** 1-61 (2001)
88. Guimaraes, F.F., J.C. Belchior, R.L. Johnston, and C. Roberts, *Global optimization analysis of water clusters (H2O)(n) (11 <= n <= 13) through a genetic evolutionary approach*, J. Chem. Phys., **116,** 8327-8333 (2002)
89. Lloyd, L.D., R.L. Johnston, C. Roberts, and T.V. Mortimer-Jones, *Geometry optimisation of aluminium clusters using a genetic algorithm*, ChemPhysChem, **3,** 408-+ (2002)
90. Massen, C., T.V. Mortimer-Jones, and R.L. Johnston, *Geometries and segregation properties of platinum-palladium nanoalloy clusters*, Journal of the Chemical Society-Dalton Transactions, 4375-4388 (2002)
91. Sayle, D.C. and R.L. Johnston, *Evolutionary techniques in atomistic simulation: thin films and nanoparticles*, Curr. Opin. Solid State Mat. Sci., **7,** 3-12 (2003)
92. Sayle, D.C. and G.W. Watson, *Structural exploration of thin-film oxide interfaces via 'simulated amorphisation and recrystallisation'*, Surf. Sci., **473,** 97-107 (2001)

93. Sayle, D.C., J.A. Doig, S.A. Maicaneanu, and G.W. Watson, *Atomistic structure of oxide nanoparticles supported on an oxide substrate*, Phys. Rev. B, **65,** art. no.-245414 (2002)
94. Sayle, D.C. and G.W. Watson, *Atomistic structures of 25000-atom oxide nanoparticles supported on an oxide substrate*, J. Phys. Chem. B, **106,** 10793-10807 (2002)
95. Sayle, D.C., J.A. Doig, S.C. Parker, and G.W. Watson, *Metal oxide encapsulated nanoparticles*, J. Mater. Chem., **13,** 2078-2089 (2003)
96. Sayle, T.X.T., C.R.A. Catlow, R.R. Maphanga, P.E. Ngoepe, and D.C. Sayle, *Evolving microstructure in MnO2 using amorphisation and recrystallisation*, J. Cryst. Growth, **294,** 118-129 (2006)
97. Zhang, H.Z., B. Gilbert, F. Huang, and J.F. Banfield, *Water-driven structure transformation in nanoparticles at room temperature*, Nature, **424,** 1025-1029 (2003)
98. Zhang, H.Z., F. Huang, B. Gilbert, and J.F. Banfield, *Molecular dynamics simulations, thermodynamic analysis, and experimental study of phase stability of zinc sulfide nanoparticles*, J. Phys. Chem. B, **107,** 13051-13060 (2003)
99. Israelachvili, J., *Intermolecular and Surface Forces*. 2nd ed. 1997, London: Academic Press.
100. Hamaker, H.C., *The London-van der Waals attraction between spherical particles*, Physica, **4,** (1937)
101. Bergstrom, L., *Hamaker constants of inorganic materials*, Adv. Colloid Interface Sci., **70,** 125-169 (1997)
102. Lifshitz, E.M., *The theory of molecular attractive forces between solids*, Sov. Phys. JETP (Engl. Transl.), **2,** (1956)
103. Derjaguin, B.V. and L. Landau, *Theory of the stability of strongly charged lyophobic sols and the adhesion of strongly charged particles in solutions of electrolytes*, **14,** 633 (1941)
104. Verwey, E.G.W. and T.G. Overbeek, *Theory of stability of lyophobic colloids*. 1st ed. 1948, Amsterdam: Elsevier.
105. Atkins, P.W., *Physical Chemistry*. 6th ed. 1999, Oxford: Oxford University Press.
106. Schulze, H., J Prakt Chem, **25,** 431 (1882)
107. Hardy, W., *A preliminary investigation of the conditions which determine the stability of irreversible hydrosols*, Proceedings of the Royal Society of London, **66,** 110 (1900)
108. Missana, T. and A. Adell, *On the applicability of DLVO theory to the prediction of clay colloids stability*, J. Colloid Interface Sci., **230,** 150-156 (2000)
109. Andersson, K.M. and L. Bergstrom, *DLVO interactions of tungsten oxide and cobalt oxide surfaces measured with the colloidal probe technique*, J. Colloid Interface Sci., **246,** 309-315 (2002)
110. Meurk, A., P.F. Luckham, and L. Bergstrom, *Direct measurement of repulsive and attractive van der Waals forces between inorganic materials*, Langmuir, **13,** 3896-3899 (1997)

111. Kerisit, S. and K.M. Rosso, *Computer simulation of electron transfer at hematite surfaces*, Geochim. Cosmochim. Acta, **70,** 1888-1903 (2006)
112. Nolan, M., S.C. Parker, and G.W. Watson, *The electronic structure of oxygen vacancy defects at the low index surfaces of ceria*, Surf. Sci., **595,** 223-232 (2005)
113. Watson, G.W., R.P.K. Wells, D.J. Willock, and G.J. Hutchings, *Ab initio simulation of the interaction of hydrogen with the {111} surfaces of platinum, palladium and nickel. A possible explanation for their difference in hydrogenation activity*, Chem. Commun., 705-706 (2000)
114. Watson, G.W., R.P.K. Wells, D.J. Willock, and G.J. Hutchings, *pi adsorption of ethene on to the {111} surface of copper - A periodic ab initio study of the effect of k-point sampling on the energy, atomic and electronic structure*, Surf. Sci., **459,** 93-103 (2000)
115. Born, M. and K. Huang, *Dynamical Theory of Crystal Lattices*. 1st ed. 1954, Oxford: Oxford University Press.
116. Ewald, P.P., *Die berechnung optisher und elektostatischer gitterpotentiale*, Annalen der Physik, **64,** 253 (1921)
117. Parry, D.E., *The electrostatic potential in the surface region of an ionic crystal*, Surf. Sci., **49,** 433-440 (1975)
118. Parry, D.E., *Errata*, Surf. Sci., **54,** 195 (1976)
119. Kittel, C., *Introduction to Solid State Physics*. 2nd ed. 1963, New York: John Wiley & Sons.
120. Heyes, D.M., M. Barber, and J.H.R. Clarke, *Molecular dynamics computer simulation of surface properties of crystalline potassium chloride*, Journal of Chemistry Society Faraday Transactions 2: Molecular and Chemical Physics, **73,** 1485-1496 (1977)
121. Lewis, G.V. and C.R.A. Catlow, *Potential model for ionic oxides*, J. Phys. C: Solid St. Phys., **18,** 1149-1161 (1985)
122. de Leeuw, N.H., F.M. Higgins, and S.C. Parker, *Modeling the surface structure and stability of alpha-quartz*, J. Phys. Chem. B, **103,** 1270-1277 (1999)
123. Higgins, F.M., G.W. Watson, and S.C. Parker, *Effect of lattice relaxation on cation exchange in zeolite A using computer simulation*, J. Phys. Chem. B, **101,** 9964-9972 (1997)
124. Catlow, C.R.A., M. Norgett, and T.A. Ross, *Ion transport and interatomic potentials in alkaline-earth-fluoride crystals*, J. Phys. C: Solid St. Phys., **10,** 1627-1640 (1977)
125. Slater, B., J.D. Gale, C.R.A. Catlow, T. Ohsuna, and O. Terasaki, *Surface structure determination of zeolites*, in *Recent Advances in the Science and Technology of Zeolites and Related Materials, Pts a - C*. 2004. p. 1197-1203.
126. Collins, D.R., W. Smith, N.M. Harrison, and T.R. Forester, *Molecular dynamics study of TiO2 microclusters*, J. Mater. Chem., **6,** 1385-1390 (1996)
127. Collins, D.R., W. Smith, N.M. Harrison, and T.R. Forester, *Molecular dynamics study of the high temperature fusion of TiO2 nanoclusters*, J. Mater. Chem., **7,** 2543-2546 (1997)

128. Naicker, P.K., P.T. Cummings, H.Z. Zhang, and J.F. Banfield, *Characterization of titanium dioxide nanoparticles using molecular dynamics simulations*, J. Phys. Chem. B, **109,** 15243-15249 (2005)
129. Oliver, P.M., S.C. Parker, J. Purton, and D.W. Bullett, *Atomistic Simulations and Electronic-Structure of Tio2(100) Surfaces*, Surf. Sci., **309,** 1200-1205 (1994)
130. Watson, G.W., S.C. Parker, and A. Wall, *Molecular-Dynamics Simulation of Fluoride-Perovskites*, J. Phys.-Condes. Matter, **4,** 2097-2108 (1992)
131. Allan, N.L., A.L. Rohl, D.H. Gay, C.R.A. Catlow, R.J. Davey, and W.C. Mackrodt, *Calculated Bulk and Surface-Properties of Sulfates*, Faraday Discuss., 273-280 (1993)
132. Paolini, G.V., P.J.D. Lindan, and J.H. Harding, *The thermal conductivity of defective crystals*, J. Chem. Phys., **106,** 3681-3687 (1997)
133. Takagi, R., F. Hutchinson, P.A. Madden, A.K. Adya, and M. Gaune-Escard, *The structure of molten DyCl3 and DyNa3Cl6 simulated with polarizable- and rigid-ion models*, J. Phys.-Condes. Matter, **11,** 645-658 (1999)
134. Sayle, D.C., S.A. Maicaneanu, and G.W. Watson, *Synthesis of a BaO thin film supported on MgO(001) using a shell-model amorphisation and recrystallisation strategy*, Phys. Chem. Chem. Phys., **4,** 5189-5198 (2002)
135. Dick, A.W. and B.G. Overhauser, *Theory of dielectric constants of alkali halide crystals*, Phys. Rev., **112,** 90-103 (1958)
136. Schroder, U., *A new model for lattice dynamics ("breathing shell model")*, Solid State Communications, **4,** 347-349 (1966)
137. Catlow, C.R.A., M. Dixon, and W.C. Mackrodt, *Inter-Ionic Potentials in Ionic Solids*, Lecture Notes in Physics, **166,** 130-161 (1982)
138. Aguado, A., L. Bernasconi, S. Jahn, and P.A. Madden, *Multipoles and interaction potentials in ionic materials from planewave-DFT calculations*, Faraday Discuss., **124,** 171-184 (2003)
139. Wilson, M., S. Jahn, and P.A. Madden, *The construction and application of a fully flexible computer simulation model for lithium oxide*, J. Phys.-Condes. Matter, **16,** S2795-S2810 (2004)
140. Kresse, G. and J. Furthmuller, *Efficient iterative schemes for ab initio total-energy calculations using a plane-wave basis set*, Phys. Rev. B, **54,** 11169-11186 (1996)
141. Segall, M.D., P.J.D. Lindan, M.J. Probert, C.J. Pickard, P.J. Hasnip, S.J. Clark, and M.C. Payne, *First-principles simulation: ideas, illustrations and the CASTEP code*, J. Phys.-Condes. Matter, **14,** 2717-2744 (2002)
142. Soler, J.M., E. Artacho, J.D. Gale, A. Garcia, J. Junquera, P. Ordejon, and D. Sanchez-Portal, *The SIESTA method for ab initio order-N materials simulation*, J. Phys.-Condes. Matter, **14,** 2745-2779 (2002)
143. Gale, J.D. and A.L. Rohl, *The General Utility Lattice Program (GULP)*, Mol. Simul., **29,** 291-341 (2003)
144. Gale, J.D., C.R.A. Catlow, and W.C. Mackrodt, *Periodic Ab-Initio Determination of Interatomic Potentials for Alumina*, Model. Simul. Mater. Sci. Eng., **1,** 73-81 (1992)

145. Parker, S.C., J.O. Titiloye, and G.W. Watson, *Molecular Modeling of Carbonate Minerals - Studies of Growth and Morphology*, Philos. Trans. R. Soc. Lond. Ser. A-Math. Phys. Eng. Sci., **344,** 37-48 (1993)
146. Sayle, T.X.T., S.C. Parker, and C.R.A. Catlow, *The Role of Oxygen Vacancies on Ceria Surfaces in the Oxidation of Carbon-Monoxide*, Surf. Sci., **316,** 329-336 (1994)
147. Pavese, A., M. Catti, S.C. Parker, and A. Wall, *Modelling of the thermal dependence of structural and elastic properties of calcite, CaCO3*, Phys. Chem. Miner., **23,** 89-93 (1996)
148. Harris, D.J., J.H. Harding, and S.C. Parker, *Simulations of surfaces and interfaces in MgO*, Radiat. Eff. Defects Solids, **151,** 299-304 (1999)
149. Sayle, T.X.T., C.R.A. Catlow, D.C. Sayle, S.C. Parker, and J.H. Harding, *Computer-Simulation of Thin-Film Heteroepitaxial Ceramic Interfaces Using a near-Coincidence-Site Lattice Theory*, Philosophical Magazine a-Physics of Condensed Matter Structure Defects and Mechanical Properties, **68,** 565-573 (1993)
150. Harris, D.J., G.W. Watson, and S.C. Parker, *Vacancy migration at the {410}/ 001 symmetric tilt grain boundary of MgO: An atomistic simulation study*, Phys. Rev. B, **56,** 11477-11484 (1997)
151. Dove, M.T., B. Winkler, M. Leslie, M.J. Harris, and E.K.H. Salje, *A New Interatomic Potential Model for Calcite - Applications to Lattice-Dynamics Studies, Phase-Transition, and Isotope Fractionation*, Am. Miner., **77,** 244-250 (1992)
152. Pavese, A., M. Catti, G.D. Price, and R.A. Jackson, *Interatomic Potentials for Caco3 Polymorphs (Calcite and Aragonite), Fitted to Elastic and Vibrational Data*, Phys. Chem. Miner., **19,** 80-87 (1992)
153. de Leeuw, N.H., J.H. Harding, and S.C. Parker, *Molecular dynamics simulations of the incorporation of Mg2+, Cd2+ and Sr2+ at calcite growth steps: Introduction of a SrCO3 potential model*, Mol. Simul., **28,** 573-589 (2002)
154. de Leeuw, N.H., S.C. Parker, and J.H. Harding, *Molecular dynamics simulation of crystal dissolution from calcite steps*, Phys. Rev. B, **60,** 13792-13799 (1999)
155. Duffy, D.M. and J.H. Harding, *Simulation of organic monolayers as templates for the nucleation of calcite crystals*, Langmuir, **20,** 7630-7636 (2004)
156. Duffy, D.M. and J.H. Harding, *The crystallisation of calcite clusters on self-assembled monolayers*, Surf. Sci., **595,** 151-156 (2005)
157. de Leeuw, N.H. and S.C. Parker, *Atomistic simulation of the effect of molecular adsorption of water on the surface structure and energies of calcite surfaces*, J. Chem. Soc.-Faraday Trans., **93,** 467-475 (1997)
158. Kerisit, S., D.J. Cooke, A. Marmier, and S.C. Parker, *Atomistic simulation of charged iron oxyhydroxide surfaces in contact with aqueous solution*, Chem. Commun., 3027-3029 (2005)

159. Post, J.E. and C.W. Burnham, *Ionic Modeling of Mineral Structures and Energies in the Electron-Gas Approximation - Tio2 Polymorphs, Quartz, Forsterite, Diopside*, Am. Miner., **71,** 142-150 (1986)
160. Harrison, N.M. and V.R. Saunders, *The Structural-Properties of Beta-Mgcl2 - an Abinitio Study*, J. Phys.-Condes. Matter, **4,** 3873-3882 (1992)
161. Lin, J.S. and C.R.A. Catlow, *Computer-Modeling Studies on Mgcl2-Supported Ziegler-Natta Catalysts*, J. Mater. Chem., **3,** 1217-1225 (1993)
162. Gale, J.D., C.R.A. Catlow, and M.J. Gillan, *A density functional study of Ti/MgCl2-supported Ziegler-Natta catalysts*, Topics in Catalysis, **9,** 235-250 (1999)
163. Smith, W. and T.R. Forester, *DL_POLY_2.0: A general-purpose parallel molecular dynamics simulation package*, J. Mol. Graph., **14,** 136-141 (1996)
164. Frisch, M.J., G.W. Trucks, H.B. Schlegel, G.E. Scuseria, M.A. Robb, J.R. Cheeseman, J. Montgomery, J. A.; , T. Vreven, K.N. Kudin, J.C. Burant, J.M. Millam, S.S. Iyengar, J. Tomasi, V. Barone, B. Mennucci, M. Cossi, G. Scalmani, N. Rega, G.A. Petersson, H. Nakatsuji, M. Hada, M. Ehara, K. Toyota, R. Fukuda, J. Hasegawa, M. Ishida, T. Nakajima, Y. Honda, O. Kitao, H. Nakai, M. Klene, X. Li, J.E. Knox, H.P. Hratchian, J.B. Cross, V. Bakken, C. Adamo, J. Jaramillo, R. Gomperts, R.E. Stratmann, O. Yazyev, A.J. Austin, R. Cammi, C. Pomelli, J.W. Ochterski, P.Y. Ayala, K. Morokuma, G.A. Voth, P. Salvador, J.J. Dannenberg, V.G. Zakrzewski, S. Dapprich, A.D. Daniels, M.C. Strain, O. Farkas, D.K. Malick, A.D. Rabuck, K. Raghavachari, J.B. Foresman, J.V. Ortiz, Q. Cui, A.G. Baboul, S. Clifford, J. Cioslowski, B.B. Stefanov, G. Liu, A. Liashenko, P. Piskorz, I. Komaromi, R.L. Martin, D.J. Fox, T. Keith, Al-Laham, C.Y. M. A.; Peng, A. Nanayakkara, M. Challacombe, P.M.W. Gill, B. Johnson, W. Chen, M.W. Wong, C. Gonzalez, and J.A. Pople, *Gaussian 03, Revision C.02*. 2004, Gaussian Inc: Wallingford CT.
165. MacKerell, A.D., D. Bashford, M. Bellott, R.L. Dunbrack, J.D. Evanseck, M.J. Field, S. Fischer, J. Gao, H. Guo, S. Ha, D. Joseph-McCarthy, L. Kuchnir, K. Kuczera, F.T.K. Lau, C. Mattos, S. Michnick, T. Ngo, D.T. Nguyen, B. Prodhom, W.E. Reiher, B. Roux, M. Schlenkrich, J.C. Smith, R. Stote, J. Straub, M. Watanabe, J. Wiorkiewicz-Kuczera, D. Yin, and M. Karplus, *All-atom empirical potential for molecular modeling and dynamics studies of proteins*, J. Phys. Chem. B, **102,** 3586-3616 (1998)
166. Brooks, B.R., R.E. Bruccoleri, B.D. Olafson, D.J. States, S. Swaminathan, and M. Karplus, *Charmm - a Program for Macromolecular Energy, Minimization, and Dynamics Calculations*, Journal of Computational Chemistry, **4,** 187-217 (1983)
167. Wall, A., S.C. Parker, and G.W. Watson, *The Extrapolation of Elastic-Moduli to High-Pressure and Temperature*, Phys. Chem. Miner., **20,** 69-75 (1993)
168. Swamy, V., J.D. Gale, and L.S. Dubrovinsky, *Atomistic simulation of the crystal structures and bulk moduli of TiO2 polymorphs*, Journal of Physics and Chemistry of Solids, **62,** 887-895 (2001)

169. de Leeuw, N.H. and S.C. Parker, *Surface structure and morphology of calcium carbonate polymorphs calcite, aragonite, and vaterite: An atomistic approach*, J. Phys. Chem. B, **102,** 2914-2922 (1998)
170. Kirkpatrick, R.J., A.G. Kalinichev, and J. Wang, *Molecular dynamics modelling of hydrated mineral interlayers and surfaces: structure and dynamics*, Mineral Mag, **69,** 289-308 (2005)
171. Fletcher, R. and C.M. Reeves, *Function minimization by conjugate gradients*, The Computer Journal, **7,** 149-154 (1964)
172. Norgett, M. and R. Fletcher, *Fast matrix methods for calculating the relaxation about defects in the crystals*, Journal of Physics C-Solid State Physics, **3,** L190-L192 (1970)
173. Watson, G.W., E.T. Kelsey, N.H. deLeeuw, D.J. Harris, and S.C. Parker, *Atomistic simulation of dislocations, surfaces and interfaces in MgO*, J. Chem. Soc.-Faraday Trans., **92,** 433-438 (1996)
174. Tasker, P.W., *Technical Report.* 1978.
175. Duffy, D.M. and P.W. Tasker, *Harwell Technical Report.* 1983.
176. Parker, S.C., *Chemistry.* 1st ed. 1982, London: University of London.
177. Parker, S.C. and G.D. Price, Adv. Solid. State. Chem, **1,** 295 (1989)
178. Todorov, I.T. and W. Smith, *DL_POLY_3: the CCP5 national UK code for molecular-dynamics simulations*, Philos. Trans. R. Soc. Lond. Ser. A-Math. Phys. Eng. Sci., **362,** 1835-1852 (2004)
179. Todorov, I.T., W. Smith, K. Trachenko, and M.T. Dove, *DL_POLY_3: new dimensions in molecular dynamics simulations via massive parallelism*, J. Mater. Chem., **16,** 1911-1918 (2006)
180. Verlet, L., *Computer "Experiments" on Classical Fluids. I. Thermodynamical Properties of Lennard-Jones Molecules*, Phys. Rev. J1 - PR, **159,** 98 LP - 103 (1967)
181. Hockney, R.W., *The potential calculation and some applications.* Methods in Computational Physics, ed. B. Alder, S. Fernbach, and M. Rotenberg. Vol. 9. 1970, New York/London: Academic Press.
182. Allen, M.P. and J.D. Tildesley, *Molecular Dynamics*, in *Computer Simulations of Liquids.* 1993, Oxford University Press: Oxford.
183. Swope, W.C., H.C. Andersen, P.H. Berens, and K.R. Wilson, *A Computer-Simulation Method for the Calculation of Equilibrium-Constants for the Formation of Physical Clusters of Molecules - Application to Small Water Clusters*, J. Chem. Phys., **76,** 637-649 (1982)
184. Hoover, W.G., *Canonical Dynamics - Equilibrium Phase-Space Distributions*, Phys Rev A, **31,** 1695-1697 (1985)
185. Melchionna, S., G. Ciccotti, and B.L. Holian, *Hoover Npt Dynamics for Systems Varying in Shape and Size*, Mol. Phys., **78,** 533-544 (1993)
186. Frenkel, D. and B. Smit, *Understandng Molecular Simulations.* 1996, San Diego, USA: Academic Press.
187. Catlow, C.R.A., *Computer Modelling in Inorganic Crystallography.* 1997, San Diego: Academic Press.

188. Kato, T., *Molecular dynamics simulation of liquid N2O4 reversible arrow 2NO(2) by orientation-sensitive pairwise potential. III. Reaction dynamics*, J. Chem. Phys., **120,** 829-838 (2004)
189. Marrink, S.J. and H.J.C. Berendsen, *Permeation process of small molecules across lipid membranes studied by molecular dynamics simulations*, J. Phys. Chem, **100,** 16729-16738 (1996)
190. Forester, T.R. and W. Smith, *Bluemoon simulations of benzene in silicalite-1 - Prediction of free energies and diffusion coefficients*, J. Chem. Soc.-Faraday Trans., **93,** 3249-3257 (1997)
191. Tasker, P.W., *The stability of ionic crystal surfaces*, J. Phys. C: Solid St. Phys., **12,** 4977-4984 (1979)
192. Bertaut, F., Compt. Rendu., **246,** 3447 (1958)
193. Oliver, P.M., S.C. Parker, and W.C. Mackrodt, *Computer-Simulation of the Crystal Morphology of Nio*, Model. Simul. Mater. Sci. Eng., **1,** 755-760 (1993)
194. http://www.uwm.edu/Dept/Grad_Sch/Publications/ResearchProfile/Vol21No1/marija.html
195. Tasker, P.W., Philos Mag. A, **39,** 119 (1979)
196. Wulff, G., Kristallogr. Kristallgeom., **39,** 449 (1901)
197. Lee, B. and F.M. Richards, *The interpretation of protein structures: Estimation of static accessibility*, J. Mol. Biol., **55,** 379-400 (1971)
198. Meldrum, F.C., *Calcium carbonate in biomineralisation and biomimetic chemistry*, International Materials Reviews, **48,** 187-224 (2003)
199. Ettler, V., O. Zelena, M. Mihaljevic, O. Sebek, L. Strnad, P. Coufal, and P. Bezdicka, *Removal of trace elements from landfill leachate by calcite precipitation*, Journal of Geochemical Exploration, **88,** 28-31 (2006)
200. Delgado, J., M.P. Aznar, and J. Corella, *Calcined dolomite, magnesite, and calcite for cleaning hot gas from a fluidized bed biomass gasifier with steam: Life and usefulness*, Industrial & Engineering Chemistry Research, **35,** 3637-3643 (1996)
201. Wada, S. and H. Suzuki, *Calcite and fluorite as catalyst for the Knovenagel condensation of malononitrile and methyl cyanoacetate under solvent-free conditions*, Tetrahedron Letters, **44,** 399-401 (2003)
202. Effenberger, H.M., K.;Zemann, J., *Crystal structure refinements of Magnesite, Calcite, Rhodochrosite, Siderite, Smithonite, and Dolomite, with the discussion of some aspects of the stereochemistry of Calcite type carbonates*, Zeitschrift fuer Kristallographie, **156,** 233-243 (1981)
203. Dandekar, D.P., *Variation in the Elastic Constants of Calcite with Temperature*, J. Appl. Phys., **39,** 3694-3699 (1968)
204. Kerisit, S., *Atomistic Simulation of Calcite Surfaces*, in *Department of Chemistry*. 2004, University of Bath: Bath. p. 244.
205. de Leeuw, N.H., S.C. Parker, and K.H. Rao, *Modeling the competitive adsorption of water and methanoic acid on calcite and fluorite surfaces*, Langmuir, **14,** 5900-5906 (1998)

206. Teng, H.H., P.M. Dove, C.A. Orme, and J.J. De Yoreo, *Thermodynamics of calcite growth: Baseline for understanding biomineral formation*, Science, **282,** 724-727 (1998)
207. Britt, D.W. and V. Hlady, *In-situ atomic force microscope imaging of calcite etch pit morphology changes in undersaturated and 1-hydroxyethylidene-1,1-diphosphonic acid poisoned solutions*, Langmuir, **13,** 1873-1876 (1997)
208. Lea, A.S., J.E. Amonette, D.R. Baer, Y. Liang, and N.G. Colton, *Microscopic effects of carbonate, manganese, and strontium ions on calcite dissolution*, Geochim. Cosmochim. Acta, **65,** 369-379 (2001)
209. Cheng, L.W., P. Fenter, N.C. Sturchio, Z. Zhong, and M.J. Bedzyk, *X-ray standing wave study of arsenite incorporation at the calcite surface*, Geochim. Cosmochim. Acta, **63,** 3153-3157 (1999)
210. McCarthy, M.I., G.K. Schenter, C.A. Scamehorn, and J.B. Nicholas, *Structure and dynamics of the water/MgO interface*, J. Phys. Chem, **100,** 16989-16995 (1996)
211. Impey, R.W., P.A. Madden, and I.R. McDonald, *Hydration and Mobility of Ions in Solution*, J. Phys. Chem, **87,** 5071-5083 (1983)
212. Essmann, U., L. Perera, M.L. Berkowitz, T. Darden, H. Lee, and L.G. Pedersen, *A Smooth Particle Mesh Ewald Method*, J. Chem. Phys., **103,** 8577-8593 (1995)
213. Mitchell, P.J. and D. Fincham, *Shell-Model Simulations by Adiabatic Dynamics*, J. Phys.-Condes. Matter, **5,** 1031-1038 (1993)
214. Molnar, F. and J. Rieger, *"Like-charge attraction" between anionic polyelectrolytes: Molecular dynamics simulations*, Langmuir, **21,** 786-789 (2005)
215. Rieger, J., *A new approach towards an understanding of scaling in the presence of polycarboxylates*, Tenside Surfactants Deterg., **39,** 221-225 (2002)
216. Schweins, R., J. Hollmann, and K. Huber, *Dilute solution behaviour of sodium polyacrylate chains in aqueous NaCl solutions*, Polymer, **44,** 7131-7141 (2003)
217. Boisvert, J.P., A. Malgat, I. Pochard, and C. Daneault, *Influence of the counter-ion on the effective charge of polyacrylic acid in dilute condition*, Polymer, **43,** 141-148 (2002)
218. Diez, V.K., C.R. Apesteguia, and J.I. Di Cosimo, *Aldol condensation of citral with acetone on MgO and alkali-promoted MgO catalysts*, Journal of Catalysis, **240,** 235-244 (2006)
219. Hazen, R.M. and D.S. Sholl, *Chiral selection on inorganic crystalline surfaces*, Nature Materials, **2,** 367-374 (2003)
220. Poitrasson, F. and R. Freydier, *Heavy iron isotope composition of granites determined by high resolution MC-ICP-MS*, Chemical Geology, **222,** 132-147 (2005)
221. Reeder, R.J., G.M. Lamble, J.F. Lee, and W.J. Staudt, *Mechanism of Seo42- Substitution in Calcite - an Xafs Study*, Geochim. Cosmochim. Acta, **58,** 5639-5646 (1994)

222. Bragg, W.L., *Crystal structure*, Nature, **105,** 646-648 (1920)
223. Broyden, C.G., *The convergence of a class of double rank minimization algorithms*, Journal of the Institute of Mathematics and its Applications, **6,** 222 (1970)
224. Goldfarb, D., *A Family of Variable-Metric Methods Derived by Variational Means*, Mathematics of Computation, **24,** 23-& (1970)
225. Shanno, D.F. and K.H. Phua, *Matrix Conditioning and Non-Linear Optimization*, Mathematical Programming, **14,** 149-160 (1978)
226. Wogelius, R.A., K. Refson, D.G. Fraser, G.W. Grime, and J.P. Goff, *Periclase Surface Hydroxylation During Dissolution*, Geochim. Cosmochim. Acta, **59,** 1875-1881 (1995)
227. Johnson, D.A., *Some thermodynamic aspects of inorganic chemistry*. 2nd ed. 1982, Cambridge: Cambridge University Press.
228. Friedman, H.L., *Hydration Complexes - Some Firm Results and Some Pressing Questions*, Chemica Scripta, **25,** 42-48 (1985)
229. Spagnoli, D., D.J. Cooke, S. Kerisit, and S.C. Parker, *Molecular dynamics simulations of the interaction between the surfaces of polar solids and aqueous solutions*, J. Mater. Chem., **16,** 1997-2006 (2006)
230. Dove, P.M. and C.M. Craven, *Surface charge density on silica in alkali and alkaline earth chloride electrolyte solutions*, Geochim. Cosmochim. Acta, **69,** 4963-4970 (2005)
231. Busing, W.R., *An Interpretation of the Structures of Alkaline Earth Chlorides in Terms of Interionic Forces*, Transactions of the American Crystallographic Association, **6,** 57-72 (1970)
232. Bassi, I.W.P., F.;Calcaterra, M.;Bart, J.C.J., *A new layer structure of Mg Cl2 with hexagonal close packing of the chlorine atoms*, Zeitschrift fuer Kristallographie, **159,** 297-302 (1982)
233. Kosmulski, M., *pH-dependent surface charging and points of zero charge - II. Update*, J. Colloid Interface Sci., **275,** 214-224 (2004)
234. Garcia, H., J.M.L. Nieto, E. Palomares, and B. Solsona, *Photoluminescence of supported vanadia catalysts: linear correlation between the vanadyl emission wavelength and the isoelectric point of the oxide support*, Catalysis Letters, **69,** 217-221 (2000)
235. Russo, S. and C. Noguera, *Acido-Basic Properties of Simple Oxide Surfaces .2. A Simple-Model*, Surf. Sci., **262,** 259-270 (1992)
236. Banfield, J.F., S.A. Welch, H.Z. Zhang, T.T. Ebert, and R.L. Penn, *Aggregation-based crystal growth and microstructure development in natural iron oxyhydroxide biomineralization products*, Science, **289,** 751-754 (2000)
237. Zhang, H.Z. and J.F. Banfield, *Aggregation, coarsening, and phase transformation in ZnS nanoparticles studied by molecular dynamics simulations*, Nano Lett., **4,** 713-718 (2004)
238. He, G., S. Gajjeraman, D. Schultz, D. Cookson, C.L. Qin, W.T. Butler, J.J. Hao, and A. George, *Spatially and temporally controlled biomineralization is facilitated by interaction between self-assembled dentin matrix protein 1*

and calcium phosphate nuclei in solution, Biochemistry, **44,** 16140-16148 (2005)
239. Tsirelson, V.G., A.S. Avilov, Y.A. Abramov, E.L. Belokoneva, R. Kitaneh, and D. Feil, *X-ray and electron diffraction study of MgO*, Acta Crystallographica Section B-Structural Science, **54,** 8-17 (1998)
240. Maslen, E.N.S.t., V.A.;Strel'tsova, N.R., *X-ray study of the electron density in calcite, CaCO3*, Acta Crystallographica B, **49,** 636-641 (1993)
241. Wyckoff, R.W.G., *The crystal structures of some carbonates of the calcite group*, American Journal of Science, Serie **50,** 317-360 (1920)
242. Benzerara, K., T.H. Yoon, T. Tyliszczak, B. Constantz, A.M. Spormann, and G.E. Brown, *Scanning transmission X-ray microscopy study of microbial calcification*, Geobiology, **2,** 249-259 (2004)
243. Suzuki, M., H. Nagasawa, and T. Kogure, *Synthesis and structure of hollow calcite particles*, Cryst. Growth Des., **6,** 2004-2006 (2006)
244. Addadi, L., S. Raz, and S. Weiner, *Taking advantage of disorder: Amorphous calcium carbonate and its roles in biomineralization*, Adv. Mater., **15,** 959-970 (2003)
245. Faatz, M., F. Grohn, and G. Wegner, *Amorphous calcium carbonate: Synthesis and potential intermediate in biomineralization*, Adv. Mater., **16,** 996-+ (2004)
246. Weiner, S., Y. Levi-Kalisman, S. Raz, and L. Addadi, *Biologically formed amorphous calcium carbonate*, Connect Tissue Res, **44,** 214-218 (2003)
247. http://www.cse.clrc.ac.uk/msi/software/DL_POLY/MANUALS/USRMAN2.16.pdf
248. Tay, K. and F. Bresme, *Computer simulations of two dimensional gold nanoparticle arrays: the influence of core geometry*, Mol. Simul., **31,** 515-526 (2005)